

**Carnegie Mellon University**  
**MELLON COLLEGE OF SCIENCE**

**THESIS**

SUBMITTED IN PARTIAL FULFILLMENT OF THE REQUIREMENTS  
FOR THE DEGREE OF

**DOCTOR OF PHILOSOPHY IN THE FIELD OF PHYSICS**

TITLE: "Investigation of Elastic Properties of Lipids and Proteins using Computer Simulations"

PRESENTED BY: Patrick Diggins

ACCEPTED BY THE DEPARTMENT OF PHYSICS

Markus Deserno	3/31/16
MARKUS DESERNO, CHAIR PROFESSOR	DATE

Stephen Garoff	3/31/16
STEPHEN GAROFF, DEPT HEAD	DATE

APPROVED BY THE COLLEGE COUNCIL

Fred Gilman	3/31/16
FRED GILMAN, DEAN	DATE

# Investigation of Elastic Properties of Lipids and Proteins using Computer Simulations

by

Patrick Diggins

Submitted in partial fulfillment of the  
requirements for the degree of  
Doctor of Philosophy  
at  
Carnegie Mellon University  
Department of Physics  
Pittsburgh, Pennsylvania

Advised by Professor Markus Deserno

March 28, 2016



*To Katie*



## Abstract

The elastic properties of biological materials play an important role in many biomechanical functions. As a result, a large effort has gone into understanding these properties through the creation of theoretical frameworks and the measurement of the parameters entering such theories. With the improvement of computer hardware and software, computational studies now work alongside experimental techniques to probe the mechanics of biomaterials. In this thesis, we will look at three different ways that computational work to improve our understanding of the elastic properties of biomaterials: (1) developing methods to measure important material parameters, (2) test theories and provide data to refine theories, and (3) develop new computational models to investigate the properties of biomaterials.

In Chapter 2, we discuss a method of measuring the bending modulus of lipid bilayers in the fluid-phase by simulating buckled membranes. This method is computationally efficient and can be applied to lipid models of a wide range of resolution, using both implicit or explicit solvent. After showing how Helfrich theory [1], a standard theory of membrane elasticity, predicts the shape of the buckles as well as the stress-strain relation, we apply the method to three different coarse-grained models: a low resolution implicit solvent model, a medium resolution implicit solvent model, and a medium resolution explicit solvent model.

In Chapter 3, we try to apply the method from Chapter 2 to membranes in the gel-phase. We find that Helfrich theory fails to accurately describe both the shape and stress-strain relation of the buckles. Drawing inspiration from the shapes of the simulated buckles, we present a modification of Helfrich theory that incorporates curvature softening and show that this theory does describe both the shape and stress of the gel-phase buckles. Unexpectedly, the buckles exhibit negative compressibility.

In Chapter 4, we apply the new theory to the fluid-phase buckles studied in Chapter 2. The large fluctuations of the membranes makes the error in our measurement of the shapes too large to draw proper conclusions from the shape, but we are able to fit the theory directly to the stress-strain relation from the simulations. The results show that there is a small amount of curvature softening at large curvatures, and this has a small effect on the bending modulus of the lipids.

In Chapter 5, we switch our focus to the study of elastic networks, a way of investigating the fluctuations of biomolecules such as globular proteins and folded RNA structures. Specifically, we study a technique to create coarse-grained elastic networks from a high resolution model without the need to run a reference simulation. We show that the choice of which particles to remove upon coarse-graining determines the ability of the elastic network to reproduce the fluctuations of the high resolution model, with a good choice of particles leading to a network that performs exceptionally well at replicating the fluctuations.



## Acknowledgments

Though this may be “my” thesis, it would have never come into existence without the help of a number of people. First and foremost, I thank Markus for all he has done as my advisor. He has shown me how a scientist is supposed to act, and his enthusiasm and support have motivated me throughout my time at Carnegie Mellon. In addition, he has given me a strong foundation in computational physics, biophysics, and statistics. I would not be where I am now as a researcher without him.

Next, I thank the members of my thesis committee: Adam Linstedt, John Nagle, and Mathias Lösche. Their advice during my annual reviews has been valuable to my research efforts over the last four years. Their comments have made this thesis much better than it otherwise would have been.

I was fortunate to visit the Max Planck Institute for Polymer Research in Mainz Germany, for a summer, both in terms of academic and personal experience. I thank Kurt Kremer for inviting me, and Raffaello Potestio for working directly with me when I was there. The work shown in Chapter 5 has been done in collaboration with Raffaello, and the project would never have reached the point it has without his insight during our conversations. Finally, I would like to thank all my friends in Mainz, especially Karsten and Denis, for improving my experience outside of the Institute.

I want to thank Christian Holm’s group at the University of Stuttgart for inviting me to present tutorials at their ESPRESSO summer schools for four years. I now have seen more of the “sites” in Stuttgart than any other city. I also want to thank the Kavli Institute for Theoretical Physics in Santa Barbara for a wonderful summer of learning and fun.

I thank Tristan, Cem, Mingyang, and Zunjing for making me feel welcome when I entered the Deserno group. They all went out of their way to help me transition into a graduate student. I especially want to thank Mingyang for all his work on the buckling project. Mentoring Changjiang over one summer was one of my favorite experiences at CMU. I always have had stimulating conversations with Venky about elastic networks and science in general. Zach has been vital to the work of Chapter 3, and it has been a pleasure to work with him. I want to thank Mert, Xin, Nick, Pablo, and Martina for keeping the Deserno group “awesome.”

I thank the participants in the weekly Biophysics Plots and Scotch for wonderful discussions every week.

Finally, I want to thank my family for all their support. I especially want to thank Katie for inspiring me to keep working when I needed to work and stop working when I needed a break.

# List of Publications

## Chapter 2

M. Hu, P. Diggins, and M. Deserno “Determining the bending modulus of a lipid membrane by simulating buckles,” *J. Chem. Phys.*, vol. 138, p. 214110, 2013.

## Chapter 3

P. Diggins IV, Z. A. McDargh, and M. Deserno, “Curvature softening and negative compressibility of gel-phase lipid membranes,” *J. Am. Chem. Soc.*, vol. 137, pp. 12752–12755, 2015.

## Chapter 5

P. Diggins IV, Changjiang Liu, R. Potestio, M. Deserno, “Investigation of efficient coarse-grained elastic network method,” in preparation.

# Contents

<b>1</b>	<b>Introduction</b>	<b>1</b>
1.1	Overview of Thesis Projects . . . . .	1
1.2	Motivation . . . . .	2
1.3	Relevant Biological Materials . . . . .	3
1.3.1	Lipids . . . . .	3
1.3.2	Proteins . . . . .	4
1.3.3	Ribonucleic Acid (RNA) . . . . .	5
1.4	Biophysics Simulations . . . . .	6
1.5	Coarse-Graining . . . . .	6
1.5.1	Benefits of Coarse-Grained Models . . . . .	7
1.5.2	Creating Coarse-Grained Models . . . . .	7
1.5.3	Limitations of Coarse-Grained Models . . . . .	9
1.6	Lipid Models Used in This Thesis . . . . .	9
1.6.1	Cooke . . . . .	9
1.6.2	MARTINI . . . . .	11
1.6.3	Plum . . . . .	12
1.7	Elastic Networks . . . . .	12
<b>2</b>	<b>Buckling of Fluid Membranes</b>	<b>15</b>
2.0.1	Modeling Lipid Bilayers: Helfrich Theory . . . . .	15
2.0.2	Measuring $\kappa$ . . . . .	16
2.1	Buckling Theory . . . . .	18
2.1.1	Hamiltonian and Shape Equation . . . . .	19
2.1.2	Applying the constraint of imposed strain . . . . .	21
2.1.3	Stress-Strain Relationship . . . . .	22
2.1.4	Isotropic stress . . . . .	24
2.1.5	Undulation correction for $f_x$ . . . . .	25
2.2	Summary of Buckling Theory . . . . .	26
2.3	Simulation Setup . . . . .	27
2.3.1	Theoretical Considerations . . . . .	27
2.3.2	Creating the Buckles . . . . .	27
2.3.3	Simulation Parameters . . . . .	29

2.4	Simulation Results . . . . .	29
2.4.1	Stress-Strain Relation . . . . .	30
2.4.2	Getting the Shape of Buckled Membranes . . . . .	33
2.4.3	Shape of Buckles . . . . .	37
2.5	Energetics of Fluid Membranes . . . . .	38
2.6	Discussion . . . . .	45
<b>3</b>	<b>Buckling Gel Membranes</b>	<b>46</b>
3.0.1	Gel phase Membranes . . . . .	46
3.0.2	Motivation for using buckling method for gel-phase membranes	47
3.1	Simulation setup . . . . .	47
3.1.1	Lipid models: Cooke . . . . .	48
3.1.2	Lipid models: MARTINI . . . . .	48
3.1.3	Simulation parameters . . . . .	48
3.1.4	Creating the gel membranes . . . . .	49
3.1.5	Creating buckles . . . . .	50
3.1.6	Comment on Simulation Difficulties . . . . .	50
3.2	Applying Helfrich Theory to Gel Membranes . . . . .	52
3.3	Theory . . . . .	54
3.3.1	Modifying Helfrich Theory . . . . .	54
3.3.2	Predicting the shape and stress in the new theory . . . . .	58
3.4	Results . . . . .	61
3.4.1	Fitting the Simulations to the New Theory . . . . .	62
3.4.2	Shape . . . . .	62
3.4.3	Stress-strain Relation . . . . .	63
3.4.4	Values . . . . .	64
3.4.5	Energetics . . . . .	69
3.5	Materials with Negative Compressibility . . . . .	72
3.6	Discussion . . . . .	73
<b>4</b>	<b>Revisiting the Buckling of Fluid Membranes</b>	<b>75</b>
4.1	Analyzing the Shape of Fluid Membranes . . . . .	76
4.1.1	Shape . . . . .	76
4.1.2	Stress-strain Relationship from the Shape . . . . .	82
4.2	Fit to Stress-strain Relationship . . . . .	85
4.2.1	Stress-strain Relationship . . . . .	85
4.2.2	Shape . . . . .	87
4.3	Summary of Material Parameters . . . . .	87
4.4	Discussion . . . . .	89

<b>5</b>	<b>Coarse-graining Elastic Networks</b>	<b>90</b>
5.1	Theory . . . . .	91
5.1.1	Creating the Hessian . . . . .	92
5.1.2	Creating the Coarse-Grained Hessian . . . . .	92
5.1.3	Creating the Coarse-Grained Elastic Network . . . . .	93
5.2	Metrics to determine quality of CG Elastic Networks . . . . .	95
5.3	Effects of System Size and Number of Removed Particles on Metrics .	96
5.4	Elastic Networks for Protein Molecule . . . . .	97
5.4.1	Random Configuration Distributions . . . . .	97
5.4.2	Defining the Spring Constant . . . . .	98
5.4.3	RMSF of Random Reductions . . . . .	101
5.4.4	Single Particle per Amino Acid . . . . .	101
5.4.5	Optimized Reductions . . . . .	102
5.4.6	Efficient MC Steps . . . . .	104
5.5	Elastic Networks for RNA . . . . .	106
5.5.1	Random Configuration Distribution . . . . .	107
5.5.2	Single Particle per Nucleic Acid . . . . .	109
5.6	Discussion . . . . .	113

# List of Tables

2.1	Series coefficients . . . . .	22
2.2	Summary of important simulation properties . . . . .	30
2.3	Bending rigidity values . . . . .	33
3.1	Gel membrane material values . . . . .	68
4.1	Summary of material parameters for fluid membranes . . . . .	89
5.1	Metrics for Protein single atom type reductions . . . . .	102
5.2	Metrics for RNA randomly chosen reductions . . . . .	108
5.3	Metrics for RNA single atom type reductions . . . . .	111

# List of Figures

1.1	DMPC lipid . . . . .	4
1.2	Amino acids . . . . .	5
1.3	RNA nucleotide . . . . .	5
1.4	Cooke lipid image . . . . .	10
1.5	MARTINI lipid image . . . . .	11
1.6	Plum lipid image . . . . .	12
2.1	Buckle illustration . . . . .	19
2.2	Graph of important series functions . . . . .	23
2.3	Stress-strain relationship for the Cooke model . . . . .	31
2.4	Stress-strain relationship for the MARTINI model . . . . .	31
2.5	Stress-strain relationship for the Plum model . . . . .	32
2.6	Shifting Cooke monolayers to midplane . . . . .	34
2.7	Normalizing position of buckle . . . . .	35
2.8	Length of Fourier series fit as function of number of coefficients . . . . .	36
2.9	Fluctuation range for Cooke buckles . . . . .	36
2.10	Fluctuation range for MARTINI buckles . . . . .	37
2.11	Fluctuation range for Plum buckles . . . . .	37
2.12	Buckle reflections . . . . .	38
2.13	Shape of Cooke fluid buckles . . . . .	39
2.14	Shape of MARTINI fluid buckles . . . . .	39
2.15	Shape of Plum fluid buckles . . . . .	40
2.16	RMSD for Cooke fluid buckles . . . . .	40
2.17	RMSD for MARTINI fluid buckles . . . . .	41
2.18	RMSD for Plum fluid buckles . . . . .	41
2.19	Energetics of the Cooke buckles . . . . .	42
2.20	Energetics of the MARTINI buckles . . . . .	43
2.21	Energetics of the Plum buckles . . . . .	44
2.22	Temperature dependence of $\kappa$ for the Cooke model . . . . .	45
3.1	Cooke phase transition jumps . . . . .	49
3.2	Jump in energy and force for gel simulations . . . . .	51
3.3	Image showing Cooke gel membrane buckle at large strain . . . . .	51

3.4	Helfrich stress prediction for Cooke gel membranes . . . . .	52
3.5	Energy of Cooke gel membranes . . . . .	53
3.6	Predicted temperature dependence for Cooke gel membranes . . . . .	54
3.7	Cooke gel membrane shape fluctuations . . . . .	55
3.8	MARTINI gel membrane shape fluctuations . . . . .	55
3.9	Shape of Cooke gel buckle . . . . .	56
3.10	RMSD for Cooke gel buckles . . . . .	57
3.11	Shape of MARTINI gel buckle . . . . .	58
3.12	RMSD for MARTINI gel buckles . . . . .	59
3.13	Curvature energy functions . . . . .	59
3.14	Effect of $\delta$ on $\tilde{f}_x$ . . . . .	61
3.15	Cooke gel buckle shape . . . . .	63
3.16	MARTINI gel buckle shape . . . . .	64
3.17	RMSD for Cooke gel buckles . . . . .	65
3.18	$\ell$ versus strain for Cooke gel buckles . . . . .	65
3.19	Theoretical RMSD for Cooke gel buckles . . . . .	66
3.20	RMSD for MARTINI gel membranes . . . . .	66
3.21	$\ell$ versus strain for MARTINI gel buckles . . . . .	67
3.22	Theoretical RMSD for MARTINI gel buckles . . . . .	67
3.23	Stress-strain for Cooke gel buckles . . . . .	68
3.24	Stress-strain for MARTINI gel buckles . . . . .	69
3.25	Energetics of Cooke gel buckles . . . . .	70
3.26	Temperature dependence of $\kappa$ for Cooke gel membranes . . . . .	71
3.27	Temperature dependence of $\mathcal{R}$ for Cooke gel membranes . . . . .	72
3.28	Energetics of MARTINI gel buckles . . . . .	73
3.29	Temperature dependence of $\kappa$ for MARTINI gel buckles . . . . .	74
4.1	Tether Results for Cooke fluid membranes . . . . .	77
4.2	Shape comparison for Cooke fluid buckles . . . . .	78
4.3	RMSD for Cooke fluid buckles . . . . .	78
4.4	Shape of MARTINI fluid buckles . . . . .	79
4.5	RMSD for MARTINI fluid buckles . . . . .	79
4.6	Shape of Plum fluid buckles . . . . .	80
4.7	RMSD for Plum fluid buckles . . . . .	80
4.8	$\ell$ versus strain for Cooke fluid buckles . . . . .	81
4.9	$\ell$ versus strain for MARTINI fluid buckles . . . . .	81
4.10	$\ell$ versus strain for Plum fluid buckles . . . . .	82
4.11	Buckling stress for the Cooke fluid membrane . . . . .	83
4.12	Buckling stress for the MARTINI fluid membrane . . . . .	84
4.13	Buckling stress for the Plum fluid membrane . . . . .	85
4.14	Buckling stress for Cooke fluid membrane . . . . .	86
4.15	Buckling stress for MARTINI fluid membrane . . . . .	87

4.16	RMSD for Cooke fluid buckles . . . . .	88
4.17	RMSD for MARTINI fluid buckles . . . . .	88
5.1	Flow of coarse graining elastic network method . . . . .	91
5.2	Flow of coarse graining elastic network method updated . . . . .	94
5.3	Effect of system size on good bond fraction . . . . .	96
5.4	Image of Adenylate Kinase protein . . . . .	97
5.5	Protein good bond fraction distribution . . . . .	98
5.6	Protein average ratio distribution . . . . .	99
5.7	Good bond fraction versus average ratio . . . . .	100
5.8	RMSF for protein network using largest eigenvalue and trace . . . . .	100
5.9	RMSF for a band protein network . . . . .	101
5.10	RMSF for $C_\alpha$ network . . . . .	103
5.11	RMSF for $C_\beta$ network . . . . .	103
5.12	RMSF for simulated annealing network . . . . .	104
5.13	Image of the Adenine riboswitch . . . . .	106
5.14	Distribution of RNA good bond fraction . . . . .	107
5.15	Distribution of the RNA average ratio . . . . .	108
5.16	RMSF for good RNA network . . . . .	109
5.17	RMSF for another good RNA network . . . . .	110
5.18	RMSF for bad RNA network . . . . .	110
5.19	RMSF for phosphorous RNA network . . . . .	112
5.20	RMSF for C1' RNA network . . . . .	112
5.21	RMSF for C2 RNA network . . . . .	113

# Chapter 1

## Introduction

In the first paragraph of the textbook *Physical Biology of the Cell* [2], Phillips *et al.* declare, “The art of model building lies in striking the proper balance between too little detail and too much.” The complexity of biological processes makes it impossible for humans to understand every part of a system,<sup>1</sup> and instead frameworks must be constructed that focus on the important aspects of a problem. In this thesis, we are interested in the elastic properties of certain biological materials (lipids, proteins, and nucleic acids). Thus we start our work by using simple theoretical models for the elasticity of the materials and see what we can learn. Only when a simple model is insufficient to explain an observed phenomenon, we expand it.

Specifically, for each project in this thesis, we are working towards one or more of the following three goals: combine simulations with theory to measure material parameters in a way that has not been done before; use the results of simulations to probe the deficiencies of a theory and provide inspiration for how to improve the theory; and finally create methods that make creating simulation models easier, so that the models can later be used to address the first two goals. In the next section, we will briefly describe the different projects in this thesis and provide motivation for why they advance our goals.

### 1.1 Overview of Thesis Projects

In Chapter 2, we discuss a method for measuring the bending modulus of fluid phase lipid membranes within the framework of Helfrich theory [1]. As we will discuss in detail in the next chapter, multiple techniques have been developed to measure the bending modulus. All these techniques have different strengths and weaknesses, and measurements of the bending modulus often disagree [3]. The method that we will use relies on the active bending of membranes into buckles and extracting the bending

---

<sup>1</sup>I still remember as an undergrad walking by the door of a professor. On the door was a large poster mapping out different cellular metabolic pathways that needed 12 point font so that everything would fit.

modulus from the stress-strain relation. This technique gives precise results that help us gain a better understanding of the bending modulus underlying the elasticity of a membrane.

We present a derivation for both the shape of the buckle as well as the stress-strain relation. Next, we test the method with three different coarse-grained lipid models. Finally, we use the energetics of the buckles to find the temperature dependence of the bending modulus.

In Chapter 3, we apply the buckling method to gel-phase membranes. At first this seems like a straight forward proposition, but we show that Helfrich theory can no longer describe the simulated gel-phase buckles. By analyzing their shapes, we develop a modification to Helfrich theory that properly describes the gel-phase buckles. Combining the new theory with the simulations, we measure the bending modulus as well as a new characteristic length parameter of the modified theory. We end the chapter by exploring the energetics of the simulations to discuss the temperature dependence of the bending modulus in the gel-phase. The simulations reveal that gel-phase membranes have unexpected elastic properties. This work suggests that gel membranes may be ideal candidates to study exotic elasticity as well as enticing elements of novel nanoscale systems.

In Chapter 4, we take the buckling of membranes full circle and apply the modified theory presented in Chapter 3 to the fluid simulations of Chapter 2. We find that the new theory can describe the stress-strain relation for the fluid buckles better than Helfrich theory, but that the effect is not as large as for the gel membranes. Thus, an idea that started as a way to efficiently measure the bending modulus of fluid membranes eventually reveals new insights into the fluid phase via an instructive detour over the gel phase.

In Chapter 5, we switch from membranes to proteins and RNA and present a technique for creating improved coarse grained elastic networks without the need to run an atomistic simulation. Once the method is fully understood, it may make the creation of elastic networks for large systems easier and the networks themselves more accurate. Working toward that end, we discuss the error associated with the method and demonstrate how it is affected by the choice of coarse-grained mapping. We compare the most common mapping for protein elastic networks with better mappings following from our approach. To improve the efficiency of the method, we have developed a method to improve the performance of our Monte Carlo searches to find better networks.

## 1.2 Motivation

We will go into more detail concerning lipid membranes and proteins in the next section, but first, we want to give some reasons why we want to model these systems and calculate their elastic parameters. In order to perform different biological functions, such as forming vesicles as part of endocytosis [4, 5], lipid membranes need to

deform. This deformation is often driven by proteins, such as dynamin [6], which plays a role in the separation of newly formed vesicles from the original membrane. Proteins need energy to bend a membrane, which is supplied by GTP hydrolysis in the case of proteins like dynamin, and ATP hydrolysis for many other proteins. The amount of energy needed to reshape a membrane depends on its bending modulus, and thus we must know it before we can explain how much energy the proteins will need.

Obtaining the bending modulus of gel-phase membranes has a similar motivation to the fluid-phase membranes. We need to know the rigidity in order to understand the energy required to deform a membrane. In addition, we show in Chapter 3 that lipid membranes in the gel-phase can undergo negative compressibility under the right conditions. This might help explain the observed faceted nature of gel vesicles [7, 8]. More importantly, this insight into the elastic properties for gel membranes has large implications on the usefulness of lipid bilayers in switchable elastic nano-devices. Effort has gone into developing metamaterials that exhibit negative compressibility because of their potential in mechanical sensors and microactuators [9]. With the ability to tune the properties of lipids, they might be ideal candidates for the same functions.

For the study of proteins, a simple computational model that is easy to work with can greatly improve our understanding of the functions of certain proteins. The size of proteins and the long times needed make high resolution simulations impractical for some protein events. By efficiently creating accurate elastic networks, it may be possible to investigate events where a protein undergoes a large conformational change that primarily depends on a small part of the protein. For example, the Adenylate Kinase has an open and closed state [10]. The protein can be divided into two fairly stiff blocks connected by a hinge [11]. By modeling these blocks with a computationally inexpensive elastic network, it might be possible to observe in a computer simulation how the hinge portion changes as the protein moves between the open and closed states, without completely neglecting the fluctuations of the two blocks.

## 1.3 Relevant Biological Materials

Though there are many important molecules involved in biological processes, in this thesis, we will focus on three types of molecules: lipids, proteins, and nucleic acids.

### 1.3.1 Lipids

Lipids are small, amphiphilic molecules with a propensity to form membranes, which makes them the ideal building blocks for the two-dimensional partitions cells use to compartmentalize their interior, as well as separate themselves from the outside world. Though there are many different kinds of lipids [12], we will focus on phospholipids,

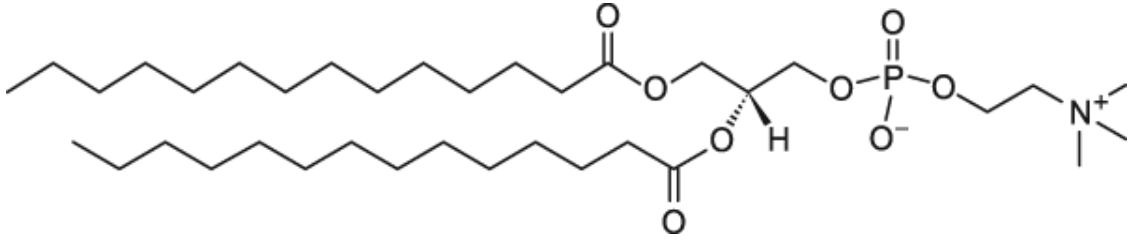


**Figure 1.1:** Chemical structure of DMPC lipid [13].

which generally consist of two hydrophobic fatty acid tails and a hydrophilic head group. The tails consist of hydrocarbon chains that normally have between 12 and 24 carbons, linked together in single bonds, with potentially a few cis-double bonds interspersed that introduce some local disorder. The chains are linked to a glycerol molecule by ester bonds. The glycerol is also linked to the phosphate group which connects to the head group of the lipid [4, 5].

The amphiphilic nature of lipids causes them to self-assemble into various structures such as bilayers, micelles, and inverse hexagonal phases [14, 15]. The structures formed depend on the type of lipid, specifically on the relative sizes of head and tail portions of the lipids [14, 15]. We will focus on lipids for which the cross sectional area of the head and tail are similar, and thus the lipids normally form bilayers [14].

On a macroscopic scale, lipid bilayers can be treated as a thin fluid-elastic sheet. The canonical starting description for the elastic energy  $\mathcal{E}$ , of these membranes is the Helfrich Hamiltonian [1]:

$$\mathcal{E}[S] = \int_S dA \left\{ \frac{1}{2} \kappa (K - K_0)^2 + \bar{\kappa} K_G \right\}, \quad (1.1)$$

where  $K = c_1 + c_2$  is the total curvature,  $c_1$  and  $c_2$  are the principal curvatures,  $K_0$  is the spontaneous curvature, and  $K_G = c_1 c_2$  is the Gaussian curvature. Furthermore,  $\kappa$  is the mean curvature modulus (or bending modulus) and  $\bar{\kappa}$  is the Gaussian curvature modulus [16, 17]. This theory breaks down at smaller length scales (on the order a couple of lipid lengths) where microscopic properties of the lipids, such as tilt, become important [18–20].

Lipid membranes in nature are normally found in a fluid phase ( $L_\alpha$ ), but as they are cooled, they can enter a variety of different phases, including the ripple ( $P_{\beta'}$ ) and gel  $L_{\beta'}$  phases. This gel-phase is characterized by an increased ordering of the tails, increase in membrane thickness, and a reduction in the area per lipid [21–24].

### 1.3.2 Proteins

The second group of molecules that will be discussed in this thesis are proteins, which are polymeric molecules formed by a chain of amino acids. They perform a variety of

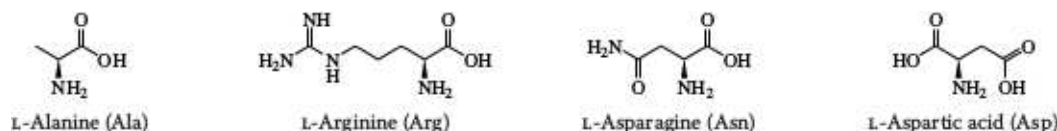


**Figure 1.2:** Chemical structure of four amino acids [28].

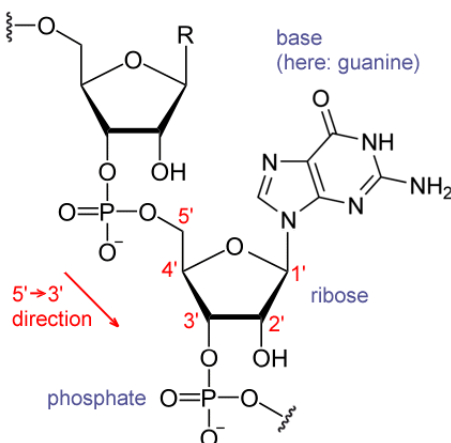


**Figure 1.3:** Image of RNA nucleotide [31].

biological roles, including cell signaling, catalyzing metabolic reactions, motors, and structural building blocks [4, 5, 25–27].

Though proteins are polymers, they have been evolutionarily optimized to have material properties beyond what is predicted by standard polymer physics. Proteins rely on the interactions of the different amino acids to form intricate secondary and tertiary structures. Most proteins are weakly stable [29, 30], and thus often rely on cooperative effects to maintain their structure. This tenuous stability of the structure results in many proteins being able to fold into multiple states, which is essential for many of their biological functions.

All amino acids have a backbone plus a side chain (except Glycine which does not have a side chain). The backbone consists of a central carbon (called the  $\alpha$ -carbon or  $C_\alpha$ ) that is connected to an amino group on one end and a carboxyl group on the other. The  $C_\alpha$  is also connected to the side chain of the protein, which is the only part that is different between amino acids. The chemical properties of the different side chains are vital to the characteristics of the proteins.

### 1.3.3 Ribonucleic Acid (RNA)

Ribonucleic acid (RNA), like Deoxyribonucleic acid (DNA), is also a polymeric compound, which in this case is formed by a chain of nucleotides. The nucleotides contain

a backbone that is formed by a sugar and a phosphate group. A nitrogenous base that is attached to the sugar group completes the nucleotide. RNA has a ribose sugar and normally has either an adenine, guanine, cytosine or uracil nitrogenous base. In contrast, DNA has a deoxyribose sugar group and has a thymine base in place of uracil. The primary function of both DNA and RNA is to store and transfer genetic information; in addition, RNA plays many roles in protein synthesis [4, 5].

Because of its hydroxyl group at the 2' position of its sugar ribose, RNA is more prone to hydrolysis than DNA (which has the hydroxyl removed<sup>2</sup>), and thus it is less stable. In addition, RNA is often found in a single-stranded form that can fold to form a large number of secondary structures, including helices and loops, and tertiary structures [32]. We will primarily be concerned with seeing how techniques commonly used to model the fluctuations of proteins work for RNA structures.

## 1.4 Biophysics Simulations

Computer simulations complement both experimental measurements and theoretical calculations [33, 34], especially in providing insight into the relationship between microscopic interactions and macroscopic phenomena. They act like virtual experiments, where the researcher knows all the microscopic positions and interactions between particles in the system. Thus, we can probe resolutions that we would otherwise be unable to investigate. Also, by comparing the results of simulations to experiments, we test the validity of the theoretical models on which the simulations are based.

Once we have a model for a system, we sample a time average by either Molecular Dynamics or Monte Carlo Simulations. Molecular dynamics (MD) simulations integrate the classical equations of motion of the system, with “thermostats” and “barostats” helping to create the proper ensemble [35, 36]. On the other hand, Monte Carlo simulations create a Markov chain where each step is determined stochastically based on a distribution function, with the choice of function determining the ensemble. In both cases, the time average of the simulated trajectory will provide a good proxy for an ensemble average as long as there is enough sampling and ergodicity holds [37]. In this thesis, we will primarily be using molecular dynamics simulations.

## 1.5 Coarse-Graining

For any computational study, an appropriate model must be chosen. Models can be classified in a number of ways, but one of the biggest classifications is between atomistic and coarse-grained simulations. As the name suggests, atomistic simulations

---

<sup>2</sup>Hence the name

represent every atom of the system explicitly<sup>3</sup>. The computational cost makes simulating large systems challenging and often impractical. Coarse-grained (CG) models aim to improve the efficiency of simulations by combining multiple atoms into a single particle while preserving the important physics of the system.<sup>4</sup>

### 1.5.1 Benefits of Coarse-Grained Models

The most obvious benefit of coarse graining is the reduced computational effort for each time step because the CG model has less particles, but there are other factors that also speed up coarse-grained (CG) simulations. With lower resolution, CG models average out the fast degrees of freedom of an atomistic model (such as bond vibrations), and are thus able to use larger time steps during MD simulations [39, 40]. This also leads to lower molecular friction and a smoother energy landscape that is easier to sample. Putting everything together, CG models can have more than three orders of magnitude computational speedup compared to atomistic models [41].

Obviously any reduction in simulation time is nice, but for many biological systems it is a necessity. As an example, we can look at the simulation of a membrane in a square simulation box of length  $L$ . The number of particles in the membrane is proportional to  $L^2$ , so if the box size is doubled, we will have four times the number of particles in the membrane. This increase in the number of particles can be dealt with through parallel computing via standard domain decomposition schemes. However, this is not the end of the story because the relaxation time for the undulation modes of the membrane scales as  $L^4$  in the absence of hydrodynamic interactions. Therefore, the time needed for the simulation scales as  $L^6$  [42], and doubling the simulation size requires 64 times as much computational effort.

Besides improvements in efficiency, coarse-graining has a more subtle benefit. The goal of coarse-graining is to preserve the important physics of the system that produces the phenomenon that we want to study. Both successful models and failures provide insight into the system [43]. If a model works, we know that we have removed the parts of the system that probably do not matter for the question at hand, while if the model fails, we have apparently eliminated an important part of the system.

### 1.5.2 Creating Coarse-Grained Models

The creation of any CG model requires two steps: (1) creating a mapping from the high-resolution system to the CG system, and (2) defining the interactions between the CG particles in a way that preserves the essential physics.

---

<sup>3</sup>The exception is a class of models called united-atom models, in which the non-polar hydrogens are implicitly included in their “parent” heavy atoms. This is a form of coarse-graining, but these models are often considered atomistic. The Berger lipid model is a popular united-atom model [38].

<sup>4</sup>One should remember that even atomistic models already have a form of coarse graining as they rely on classical and not quantum mechanics; the electrons are coarse-grained away, leading to effective classical interactions of bonded and non-bonded types

There are many ways to create the mapping for the CG system, and the mapping function affects the accuracy and transferability of the CG model [43]. Though there are some conditions that have been proposed for optimizing mappings [44], and systematic methods are under development [43], by and large the mapping still depends on the intuition of the modeler.

Once the mapping has been chosen, we need to develop the appropriate interactions for the CG particles. There are two main classifications for methods for creating interactions: “bottom-up” and “top-down”. In bottom-up modeling, the interactions are chosen so that the CG model can reproduce some property of a higher resolution model. On the other hand, top-down modeling tries to reproduce observables on larger scales obtained either from experiments or from general theoretical conditions.

There are many different systematic ways to parameterize a bottom-up model. With structure-based methods, the goal is to reproduce the structure factor of the high resolution model. The simplest technique is Boltzmann inversion, where we assume the radial distribution function between particles obeys the Boltzmann distribution [43, 45]:

$$g(q) = \mathcal{Z}^{-1} \exp[-\beta U(q)] \quad (1.2)$$

where  $q$  is the degree of freedom,  $\mathcal{Z}$  is the partition function,  $\beta = k_B T$ , and  $U(q)$  is the potential of the degree of freedom.  $q$  is normally the distance between particles or a bond angle, or a torsion angle. If we invert the Boltzmann distribution, we derive the potential as a function of the probability distribution:

$$U(q) = -k_B T \ln g(q) \quad (1.3)$$

This method would be exact if the many-body potential of mean force (PMF) replaces the potential energy.

In order to create reproduce the distribution function, we turn to iterative methods. In these methods, the CG potentials are guessed and a CG simulation is performed. The CG potentials are then modified based on the difference in the atomistic and CG distribution functions. The process is repeated until the distribution functions agree to an acceptable accuracy. The most common method is iterative Boltzmann Inversion (IBI) [43, 46]. Inverse Monte Carlo (IMC) [43, 47] is also effective. The difference between the two methods is in the way the CG potentials are iteratively refined.

An alternative to structure-based approaches is to try to match (or at least approximate) the multibody potential of mean force using a set of interactions (such as all possible continuous two body interactions). The first success in this regard was achieved by a method called Force Matching (FM) [43, 48, 49]. If we allow arbitrarily complex multibody potentials, FM would produce an exact result, but normally we want to come up with the best approximation using standard force fields.

Top-down models are divided into generic models and chemically specific models. Chemically specific models still aim to represent specific chemical systems, and thus

are more ambitious than generic models. They are designed to match certain thermodynamic properties of the system, such as the partitioning from an aqueous to a hydrophobic region.

In contrast, generic models are designed to qualitatively reproduce the most general properties of the material. For example, a generic lipid model might be designed to self-assemble and have a fluid and a gel phase. The interactions in generic models are normally simple and computationally efficient to calculate. The parameters of the interactions can be tuned in order to match desired macroscopic properties of a material, but one should not push this too far and ask material specific questions.

### 1.5.3 Limitations of Coarse-Grained Models

There is no such thing as a free lunch, and coarse-graining comes at a cost. Unless we use very complex multi-body potentials, we cannot reproduce all the physics in a system with a coarse-grained model [44]. There are two main problems, and they are called “representability” and “transferability” issues. The representability of a model deals with how well a model can represent different properties of the system. Most good CG models can represent a certain part of the system extremely well, while failing with other properties [50, 51]. For example, when structure-based coarse-graining is used to create a model of water, the two-body radial distribution function is matched to a high precision [52]. Certain properties that are related to the radial distribution function are then reproduced to high accuracy as well, such as the compressibility. Unfortunately, the pressure of the system may be off by a lot. For instance, some very well-known single-site CG models of water do well matching the structure, but have the pressure (at standard temperature and density) off by four orders of magnitude [52]. The pressure can be corrected, but at the cost of reduced accuracy for the compressibility. It depends on what the model is going to be used for as to whether it should be parameterized to exactly match certain properties at the expense of others or if it should reproduce many properties in a reasonable way.

Transferability is concerned with the questions of how well the model works when the state point is changed in a simulation. Every coarse-grained model is designed for a specific temperature, solvent, concentration, etc. There is no guarantee that the model will work at a different state point. Much like with representability, the transferability can often be improved at the expense of accuracy at the state point [43, 53].

## 1.6 Lipid Models Used in This Thesis

### 1.6.1 Cooke

The Cooke model is a low resolution, top-down implicit solvent lipid model [54, 55]. Each lipid is represented by three beads: one head bead and two tail beads. The beads

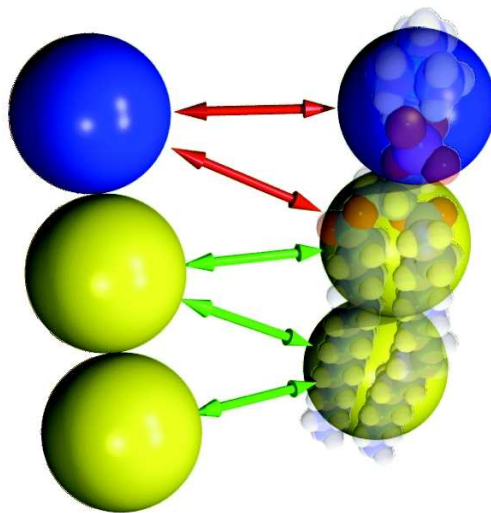


**Figure 1.4:** Image of the Cooke lipid model. The head bead is in blue and the tail beads are in yellow. The head beads only interact repulsively with other beads, while the tail beads have an attractive potential with other tail beads.

in each lipid are connected by FENE (finitely extensible nonlinear elastic) bonds to their immediate neighbors. The head and last tail bead are connected by a harmonic bond with the purpose of controlling the stiffness of the lipid. The model is designed with only two-body potentials in order to make the analysis of observables easier.

Every bead has a repulsive interaction with every other particle, which describes the excluded volume of the particle. This interaction is defined as a Weeks-Chandler-Andersen (WCA) potential, which is just a truncated and shifted Lennard-Jones potential [56]. In addition, there are attractive interactions between the tail beads of the different lipids. The attractive interactions have the form of a squared cosine function [55] which are similar to Lennard-Jones interactions, except the interaction range is easily tunable and the interaction goes exactly and smoothly to zero at some point. This extension is necessary for the model to have a fluid phase [55]. The width of the potential is controlled by a parameter  $w_c$ , which can be tuned in order to adjust the properties of the membrane. The standard value is  $w_c = 1.6\sigma$ , where  $\sigma$  is the Lennard-Jones length unit. When comparing the size of a Cooke model lipid with typical real lipid sizes, one finds that  $\sigma \approx 1$  nm [55]. The model also has an intrinsic energy unit  $\epsilon$  which we will relate to  $k_B T$ .

Since the Cooke model is highly coarse-grained, it has numerous limitations. First, the lack of solvent means that there are no hydrodynamics in the simulation, and thus any phenomenon that depends on hydrodynamics cannot be investigated. Also, the Cooke model only has one tail, whereas phospholipids have two tails. Since the model only has two tail beads, the tails have much less conformational flexibility compared to higher resolution models or realistic lipids. It will therefore be unable to represent

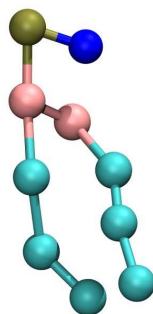


**Figure 1.5:** Image of the Martini lipid model.

phenomena which rely on these aspects of a lipid.

The power of the Cooke model comes in its efficiency. With only three beads per molecule, it does not take as much computer time to achieve long simulations. In addition, the flip-flop rate of lipids in the bilayer is faster than for higher resolution models. Thus, we can reach trans-bilayer equilibrium much faster than for many other models.

### 1.6.2 MARTINI

The MARTINI lipid models are top-down coarse-grained models with an explicit solvent [57, 58]. MARTINI beads on average represent a group of four heavy atoms. The beads are classified by the charge and hydrophobicity of their collection of atoms. There are 18 different types of CG particles that vary in their polarity and charge. The nonbonded interactions between beads are parameterized to reproduce experimental thermodynamic data, such as the free energy of hydration and vaporization, as well as the partition coefficients between water and a hydrophobic liquid, such as decane. The nonbonded interactions are the same for different systems that use the same beads, making it very easy to “click together” models using MARTINI. Of course we have to be careful how we do that. Just because MARTINI is easy to work with does not mean it is easy to get the science right.

The water beads for MARTINI correspond to four water molecules. Unfortunately, standard water in MARTINI has a tendency to freeze at 290 K, a temperature much higher than the freezing temperature of water [58]. Freezing is especially common when there are flat elements in the simulation, which makes lipid simulations a particular problem. This is solved by adding a small amount of anti-freeze (10 percent of the solvent) to the simulation. The anti-freeze is just a solvent particle that interacts with all non-solvent particles just like the ordinal solvent particle, but appears larger to solvent particles. The distance parameter of the interaction is scaled from 0.47 nm to 0.57 nm [57]. This prevents the mixed solvent from crystallizing. When there is only 10 percent anti-freeze, the effect on most observables of the membrane

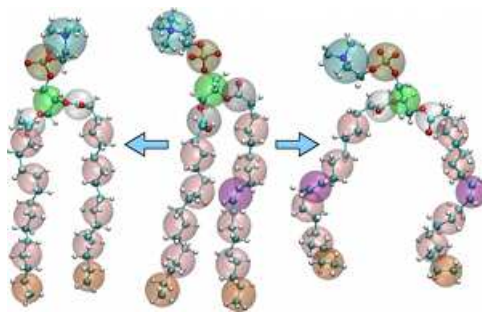


**Figure 1.6:** Image of the Plum lipid model. From left to right, DPPC, POPC, and DOPC are represented.

is less than one percent [58, 59].

There are between 10 and 12 beads per MARTINI lipid for most lipids. This gives enough resolution for MARTINI to differentiate between some types of lipids, but the resolution is not fine enough to avoid ambiguity. For example, DMPC and DLPC are represented using the same number of beads. Thus, we have to be careful to not over-interpret the quantitative measurements obtained using the MARTINI models.

### 1.6.3 Plum

A third CG model that we will use is the Plum lipid model [60, 61], a medium resolution implicit-solvent model that can, for instance, represent DPPC, DOPC, and POPC. The DPPC, POPC, and DOPC models contain 15, 16, and 17 beads, respectively. There are eight different bead types, with each bead systematically parameterized using IBI. The different lipids are created by combinations of the parameterized saturated and unsaturated tails. Because the model was parameterized using IBI from simulations of flat membranes, it performs well at reproducing the observables of flat membranes, though it may have greater transferability problems than the MARTINI model.

## 1.7 Elastic Networks

With proteins, we are often interested in how they fluctuate around an equilibrium configuration. Elastic network models provide efficient and surprisingly effective ways to model these fluctuations [62–75]. In all cases, particles are connected by a quadratic interactions (though what the interaction is quadratic in can be different). The models can be separated into two types, networks based on the distance between particles (called elastic network models or anisotropic network models, ANM) and networks based on the displacement of particles from their equilibrium positions (the most common example is the Gaussian network model) [43].

Before we discuss specific networks, let us assume that we have a system of  $N$  particles that can be described using the force field  $E(\vec{r})$  where  $\vec{r}$  is the vector of all the degrees of freedom of the system

$$\vec{r} = (\vec{r}_1, \vec{r}_2, \dots, \vec{r}_N)^T = (r_{1,x}, r_{1,y}, r_{1,z}, \dots, r_{N,x}, r_{N,y}, r_{N,z})^T. \quad (1.4)$$

We now expand the energy around the equilibrium configuration  $\vec{r}_0$  of the particles to quadratic order:

$$E(\vec{r}) \approx E_0 + \frac{1}{2} \frac{\partial^2 E}{\partial r_i^\mu \partial r_j^\nu} \delta r_i^\mu \delta r_j^\nu, \quad (1.5)$$

where  $r_i^\mu$  is the  $\mu$  component of particle  $i$  and  $\delta r_i^\mu = r_i^\mu - r_{i,0}^\mu$ . We now have a quadratic approximation of the original system that is defined by the Hessian  $\frac{\partial^2 E}{\partial r_i^\mu \partial r_j^\nu}$ . In Chapter 5, we will describe models of this form as Hessian networks or Hessian for short.<sup>5</sup>

The Gaussian network model (GNM) is a subclass of the Hessian network with its potential energy defined as [63]

$$U = \frac{k}{2} \delta \vec{r}^T \mathbf{\Gamma} \delta \vec{r}, \quad (1.6)$$

where  $k$  is the force constant,  $\delta \vec{r} = \vec{r} - \vec{r}_0$ , and  $\mathbf{\Gamma}$  is the connectivity (or Kirchhoff) matrix. The elements Kirchhoff matrix are defined by:

$$\Gamma_{ij} = \begin{cases} -1 & \text{if } i \neq j \text{ and } r_{ij} \leq r_c \\ 0 & \text{if } i \neq j \text{ and } r_{ij} > r_c \\ -\sum_{i,j \neq i} \Gamma_{ij} & \text{if } i = j \end{cases}. \quad (1.7)$$

where  $r_{ij}$  is the distance between particles  $i$  and  $j$ , and  $r_c$  is a cutoff distance.

In this network, every interaction has the same strength. The potential can be separated into independent functions of the Cartesian coordinates which make the fluctuations isotropic and thus unphysical. Despite these simplifications, this network has been effective at reproducing experimental B-factors<sup>6</sup> of proteins [63, 65, 75]. The GNM potential is a quadratic function which allows many properties, including the free energy and the fluctuations of each particle, to be determined analytically using Gaussian integrals [43, 63].

---

<sup>5</sup>This network is sometimes referred to as a Gaussian network, but the original Gaussian network had a more specific definition. We hope to avoid confusion by defining this interaction as a Hessian network.

<sup>6</sup>B-factors describe the effect of thermal motion on the attenuation of x-ray or neutron scattering. It indicates the flexibility of different parts of the system.

The energy of elastic network models (ENM)<sup>7</sup> is dependent on the distance between particles:

$$U = \frac{1}{2} \sum_{i,j} k_{i,j} (d_{i,j} - d_{i,j}^0)^2, \quad (1.8)$$

where  $d_{i,j}$  is the distance between particles  $i$  and  $j$ ,  $d_{i,j}^0$  is the equilibrium distance between the particles, and  $k_{i,j}$  is the spring constant between these particles [62, 67]. At first glance, Eq. 1.8 might look quadratic, and it is quadratic in the distance between particles, but it is *not* quadratic in the positional degrees of freedom. This makes it difficult to analyze analytically, but it can easily be incorporated into an MD simulation. The fluctuations of an ENM are anisotropic and provide more realistic normal modes than GNMs [67]. However, it surprisingly performs worse at predicting experimental B-factors [75]. In order to improve the accuracy of the network, the spring constants are often refined by comparing an observable from the CG network to the equivalent observable from atomistic reference simulation, such as the root mean square fluctuations [71]. This of course requires an atomistic simulation to be run as a reference. This is computationally expensive, and often raises the question that if we have enough computational time to run a proper reference simulation, why do we need a coarse-grained model. Indeed, the motivation for Chapter 5 is to create better elastic networks without the need for atomistic simulations.

---

<sup>7</sup>There is some confusion with what is called an elastic network. Some people will call Gaussian networks elastic networks as well. To avoid confusion, we will only use the term elastic network for networks where the energy depends explicitly on the distance between particles.

# Chapter 2

## Buckling of Fluid Membranes

In this chapter, we will introduce the buckling protocol, and show how we can measure the bending modulus of lipid membranes, as well as its temperature dependence. First, we will derive equations for the shape of a buckle and the stress-strain relation for the buckles, starting from the Helfrich Hamiltonian. Next, we show that the protocol works for three different lipid models: Cooke [54, 55], MARTINI DMPC [57], and Plum DOPC [60, 61]. The simulation shapes are compared to the theoretical prediction, and then the bending modulus for each model is calculated. Finally, we argue that by also measuring the energies during the simulations, we can gain additional insights into the thermodynamics of the buckled membranes, which enables us to describe the temperature dependence of the bending modulus in the vicinity of the actual simulation temperature.

### 2.0.1 Modeling Lipid Bilayers: Helfrich Theory

As discussed in Chapter 1, lipids can self-assemble into bilayer membranes with lateral extensions several orders of magnitude larger than the lipid size. These membranes can be modeled effectively as continuum elastic sheets for large length scales. For many problems, the Helfrich theory, a simple continuum theory with only a few parameters, is adequate to describe the membranes [1]. As mentioned in Chapter 1, Helfrich theory treats a membrane as an elastic sheet governed by the energy functional

$$\mathcal{E}[S] = \int_S dA \left\{ \frac{1}{2} \kappa (K - K_0)^2 + \bar{\kappa} K_G \right\}, \quad (2.1)$$

where  $K = c_1 + c_2$  is the total curvature,  $c_1$  and  $c_2$  are the principal curvatures,  $K_0$  is the spontaneous curvature, and  $K_G = c_1 c_2$  is the Gaussian curvature. Furthermore,  $\kappa$  is the mean curvature modulus (or bending modulus) and  $\bar{\kappa}$  is the Gaussian curvature modulus. Other terms can be added to the Hamiltonian to describe other properties of the membrane (such as the edge tension if the membrane has an open edge, or the stretching modulus), but for now we will only focus on the curvature dependence of the energy.

The principal curvatures  $c_1$  and  $c_2$  are the maximum and minimum values of all possible normal curvatures at a point on the membrane. The study of curvature and differential geometry is vast, and more thorough treatments can be found [16, 17], as well as how they apply to lipid membranes [76]. This Hamiltonian is surprisingly simple (only quadratic in curvature), but describes the behavior of lipid membranes well [77].

Though the theory fixes the functional form of the Hamiltonian, it tells us nothing about the values of the moduli, and a lot of effort has gone into trying to measure them. Before discussing techniques to measure the bending modulus, I want to quickly mention the other parameters. The spontaneous curvature,  $K_0$ , can be determined by analyzing the shape of a curved membrane with regions of opposing  $K_0$  [78]. The Gaussian modulus,  $\bar{\kappa}$ , has been measured using simulations of membranes that transition from flat patches to vesicles [79, 80]. We will now discuss how to measure the bending modulus,  $\kappa$ .

## 2.0.2 Measuring $\kappa$

There exist a fair number of techniques to measure  $\kappa$ . The most common method in simulations [54, 55, 60, 81–93] and experiments [94–99] is to measure the power spectrum of membrane undulations. For a membrane under zero lateral tension, the mean curvature modulus is obtained through the equation

$$\kappa = \frac{k_B T}{L^2 q^4 \langle |h_q|^2 \rangle}, \quad (2.2)$$

where  $|h_q|$  is the amplitude of the undulation mode of wave vector  $q$ .

The theory behind the undulation method assumes that the membrane is a thin sheet with no internal structure. This is a perfectly fine assumption for large membranes, but it begins to break down as the membrane patch becomes smaller, as the power spectrum is contaminated more and more by the lipid tilt fluctuation modes [91]. Thus, we want to sample long wavelength undulations, which require larger simulation sizes and consequently longer simulation run times.

The periodic boundary conditions require that the largest wavelength possible is  $\lambda_{\max} = L$ . The time needed for the system to reach equilibrium depends on the relaxation time of these modes. For a membrane in a viscous solvent, the relaxation time can be expressed as

$$\tau_r \approx \frac{4\mu_v}{\kappa q^3}, \quad (2.3)$$

where  $\mu_v$  is the viscosity and  $q$  is the wave vector [100–102]. This scaling prevents us from relying exclusively on computational parallelization via domain decomposition; if we double the size of the simulation, doubling the number of cores that we use to run the simulation will not be enough. We also have to run the simulation eight times longer.

To get a better feel for the problem, let us look at an early important simulation study by Lindahl and Edholm [82] in the year 2000, in which they simulated 1024 DPPC lipids (which form a square bilayer of approximate side length 20 nm) for 10 ns. This took 30,000 CPU hours. At this size, the contamination from lipid tilt modes is large [91], but at the time, simulating a membrane of this size required a herculean effort. For the bending modulus measured by Lindahl and Edholm,  $\kappa = 4 \times 10^{-20}$  J, the relaxation time for the slowest and most important mode was  $\tau_r \approx 3.2$  ns. If we were to double the box size in order to obtain slower modes, the slowest relaxation time becomes  $\tau_r \approx 26$  ns. Thus, simulations that sample the appropriate long wavelength modes for accurate results are computationally expensive.

A more recent method has been developed by Watson *et al.* [19] which embraces the lipid orientation fluctuations instead of trying to minimize their effect. Starting from a higher resolution theory that incorporates the effect of lipid tilt, it can be shown that the bending modulus depends on the square of the orientation fluctuation modes, specifically,

$$\kappa = \frac{k_B T}{q^2 \langle |\hat{n}_q^{\parallel}|^2 \rangle}, \quad (2.4)$$

where  $|\hat{n}_q^{\parallel}|$  are the amplitudes of the longitudinal orientation fluctuation modes. The orientation of a lipid is the angle it makes with respect to the  $xy$ -plane, whereas the lipid tilt is the angle that the tail makes with respect to the normal of the membrane. The orientation fluctuations are much easier to measure than the tilt fluctuations.

Since this theory relies on a microscopic quantity of the lipids, instead of assuming that the membrane is a thin sheet, much smaller simulations can be used. Specifically, Watson *et al.* showed that about 400 lipids are sufficient to achieve the same accuracy as an undulation simulation using 2048 lipids.

Both of the above methods look at fluctuations, and these fluctuations are inversely proportional to the bending modulus  $\kappa$ . Thus for flexible membranes (small values of  $\kappa$ ), the measured signal (the power spectrum) will be relatively large, and of course the opposite is true for stiff membranes. Therefore, these methods work best for flexible membranes. Active bending methods present a nice alternative to the fluctuation methods where the observable is directly proportional to the bending modulus. In these methods, the membrane is actively bent into some configuration and then the force needed to hold the membrane in this configuration is measured. Since the force is proportional to  $\kappa$ , the methods will perform better for stiffer membranes. Most fluid lipid membranes have a rigidity around  $20 k_B T$ , which falls in a range where both types of methods can be used [3], though for extremely stiff membranes, such as lipids in the gel phase, active bending is preferable.

An early example of successful active bending is the simulation of cylindrical tethers [103]. The force  $F_z$  required to hold a tether of radius  $R_t$  is directly proportional

to the bending modulus, specifically

$$\kappa = \frac{F_z R_t}{2\pi}. \quad (2.5)$$

This technique works well for highly coarse-grained implicit solvent models, but cannot be used for high resolution or explicit solvent models because of the equilibration problems. First, the cylinder partitions the simulation box into an inner and an outer region, and the solvent will need to pass through the membrane in order to reach equilibrium. The permeability of water through lipid membranes is normally between  $2 \times 10^{-3}$  to  $15 \times 10^{-3}$  cm/s [104], so we expect a water molecule to take on the order of microseconds to move through the membrane, a long time for many molecular simulations with the time needed for equilibration longer. Second, the two monolayers will have a different number of lipids since each monolayer has a different radius, and the exact number of lipids for each monolayer in equilibrium cannot be calculated at the start of the simulation. Lipid flip-flop will be required in order for the membrane to reach equilibrium. Experiments suggest that the flip-flop rate for phospholipids in a pure bilayer can be less than one flip per hour [105]. Both issues render the required simulation time too long to make simulating cylinders a practical option for anything but a highly coarse-grained implicit solvent model.

Finally, we want to mention an early attempt to extract the bending modulus using active bending that is similar to buckling technique we discuss below. Den Otter and Briels [106] used umbrella sampling methods to sample amplitudes much larger than would usually occur thermally. Unfortunately for this technique, when a membrane fluctuates at fixed projected area, it invariably needs to stretch. For the large amplitudes simulated for the paper, the associated stretching energy overwhelms bending energy. This stretching was not properly taken into account, and so the stretching contribution was misinterpreted as a bending rigidity that increased with curvature. Buckling removes this problem because the isotropic stress on the membrane is small, hence stretching and compression are less of a problem, even at large curvatures.

Our aim is to develop a method that will accurately and efficiently provide the value of  $\kappa$  for a wide range of lipid models. To this end, we want an active bending method that will work well for stiffer membranes and will not need very large simulations. The technique must avoid the limitations of other active bending methods by not partitioning the simulation box into two separate regions (for solvent based models) and lipid flip-flop should not be required to achieve thermal equilibrium. The buckling method we will now discuss satisfies all of these requirements.

## 2.1 Buckling Theory

We now discuss the theory behind the buckling method, which was first proposed by Noguchi [107]. We will be presenting a different derivation that provides an analytical

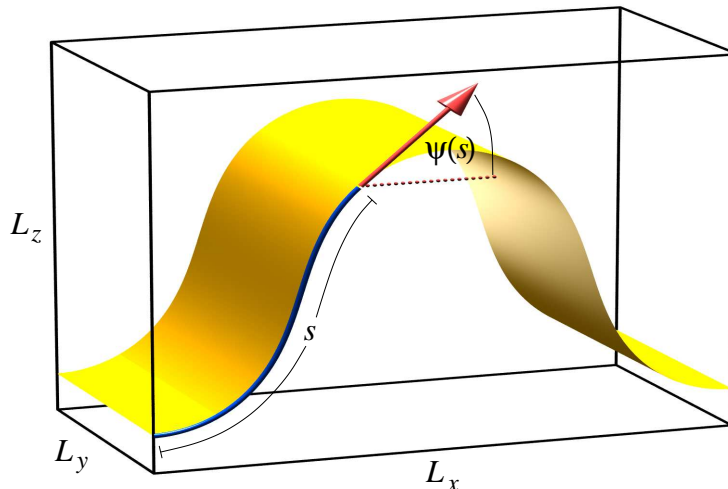


**Figure 2.1:** Illustration of the geometry of a buckled membrane. The membrane is inside a rectangular box of side lengths  $L_x$ ,  $L_y$ , and  $L_z$  and is buckled along the  $x$ -direction. Its shape is specified through the angle  $\psi(s)$  along the arc length  $s$ . The strain for this particular buckle is  $\gamma = (L - L_x)/L = 0.4$ .

solution to the stress-strain solution [108]. By minimizing the energy functional under the constraints of having a buckle of a given buckling strain, we can derive the shape of the buckle as well as the stress-strain relation along the buckle, which is then used to calculate the bending modulus.

### 2.1.1 Hamiltonian and Shape Equation

Let us assume that there is a rectangular membrane with dimensions  $(L, L_y)$ , which we fit inside a rectangular box with side lengths  $L_x < L$ ,  $L_y$ , and  $L_z$  with periodic boundary conditions in all directions. In addition, we assign the buckle to move in the  $x$ -direction so that the membrane is invariant to translations along the  $y$ -axis, as shown in Fig. 2.1. Also, we initially will ignore thermal fluctuations and focus on the ground state of the buckle.

We start by simplifying Eq. (2.1) by removing all unnecessary terms. We will only look at membranes where both monolayers have the same lipid compositions. Thus,  $K_0 = 0$  since the intrinsic curvature of the monolayers will cancel each other out. For a buckle, one of the two principle curvatures is zero, so  $K_G = 0$ . Therefore, the simplified equation becomes

$$\mathcal{E}[S] = \kappa \int_S dA \left\{ \frac{1}{2} K^2 \right\}. \quad (2.6)$$

We now parametrize the membrane shape by the angle  $\psi(s)$ , which the membrane makes against the horizontal axis, and which is measured as a function of the arc length along the contour. Note that  $K = -\dot{\psi}$ . Eq. (2.6) now becomes

$$\mathcal{E}[\psi(s)] = L_y \int_0^L ds \left\{ \frac{1}{2} \kappa \dot{\psi}(s)^2 + f_x \left[ \cos \psi(s) - \frac{L_x}{L} \right] \right\}, \quad (2.7)$$

where  $f_x$  is the Lagrange multiplier needed to constrain the box length in the  $x$ -direction to a predetermined fraction of the length of the membrane. Physically,  $f_x$  corresponds to the lateral compressive stress along the  $x$ -direction. Note that this is not the same as the isotropic surface tension  $\Sigma$  of the membrane, which we will go into more detail in Sec. 2.1.4.

The first goal is to find the shape of the buckle. After a functional variation with respect to  $\psi(s)$ , we find the Euler-Lagrange equation

$$\ddot{\psi} + \lambda^{-2} \sin \psi = 0, \quad (2.8)$$

where  $\lambda^2 = \kappa/f_x$  is a constant with dimension of squared length. Note that Eq. (2.8) is the classical pendulum equation. After multiplying it by  $\dot{\psi}$ , integrating once, and noting that the mean curvature vanishes at the inflection points of the curve, we find that

$$\dot{\psi} = \lambda^{-1} \sqrt{2(\cos \psi - \cos \psi_i)}, \quad (2.9)$$

where  $\psi_i$  is the angle at the inflection point. At this point, we can formally solve for the ground state energy by inserting Eq. (2.9) back into Eq. (2.7). We find that the ground state energy is

$$\mathcal{E} = L_y f_x (L_x - L \cos \psi_i) = f_x A [2m - \gamma], \quad (2.10)$$

where  $A = LL_y$  is the area,  $\gamma = (L - L_x)/L$  is the compressive strain, and where we define  $m$  as

$$m = \sin^2 \frac{\psi_i}{2}. \quad (2.11)$$

If we choose the arc length coordinate such that  $\psi(s=0) = 0$ , the solution to Eq. (2.9) can be expressed as an elliptic integral of the first kind:

$$s/\lambda = F \left[ \arcsin \left( m^{-1/2} \sin \left( \frac{\psi}{2} \right) \right), m \right]. \quad (2.12)$$

We use the notation of Abramowitz and Stegun [109] for all special functions. By inverting Eq. (2.12), we find the equation of the angle as a function of arc length:

$$\psi(s) = 2 \arcsin \left( m^{-1/2} \text{sn}[s/\lambda, m] \right), \quad (2.13)$$

where  $\text{sn}$  is a Jacobi elliptic function. The shape of the buckle is obtained by integrating the cosine and sine of the angle

$$x(s) = 2\lambda \text{E}[\text{am}[s/\lambda, m], m] - s, \quad (2.14a)$$

$$z(s) = 2\lambda \sqrt{m} (1 - \text{cn}[s/\lambda, m]). \quad (2.14b)$$

Though it may not be apparent, the shape of the buckle does not depend on any material properties of the lipids. In the next two sections, we will derive an expression showing that  $f_x$  is equal to  $\kappa$  times a function that depends on the buckling strain. Thus  $\lambda$  is independent of the material properties of the lipids. In addition,  $m$  only depends on the buckling strain. This means that the shape of a membrane buckle is independent of lipid type.

### 2.1.2 Applying the constraint of imposed strain

At this point, there are still two unknowns, the elliptic parameter  $m$  and a characteristic length  $\lambda$ , and we will need to enforce two constraints to find them. First, the periodic boundary conditions require that  $\psi(s)$  has a period  $L$ ; and second, the buckle must fit exactly into the box so that  $x(L) = L_x$ . The periodicity of  $\psi(s)$  requires that  $\psi(L/4) = \psi_i$ , which when combined with Eq. (2.12) means that

$$\frac{L}{4\lambda} = \text{F}\left[\frac{\pi}{2}, m\right] \equiv \text{K}[m]. \quad (2.15)$$

Also, the symmetry of the buckle requires that  $x(L/4) = L_x/4$ , which when combined with Eq. (2.14a) leads to  $L_x = 8\lambda \text{E}[m] - L$ . We now can define the compressional strain  $\gamma$  as a function of  $m$ :

$$\gamma := \frac{L - L_x}{L} = 2 \left( 1 - \frac{\text{E}[m]}{\text{K}[m]} \right). \quad (2.16)$$

We want to invert this equation to find  $m$  as a function of  $\gamma$ . Unfortunately, this cannot be done in a closed form, and we will instead strive to express the function as a series expansion. We start by writing  $m$  as a series in powers of  $\gamma$ :

$$m(\gamma) = \sum_{i=1}^{\infty} a_i \gamma^i. \quad (2.17)$$

The series expansion starts at  $i = 1$  instead of  $i = 0$  because when  $\gamma = 0$ , the membrane is flat and the inflection angle is zero. Thus,  $m = 0$  when  $\gamma = 0$ .

We could use Lagrange's inversion theorem to find the coefficients:

$$a_i = \frac{1}{i!} \lim_{m \rightarrow 0} \frac{\partial^{i-1}}{\partial m^{i-1}} \left[ \frac{2}{m} \left( 1 - \frac{\text{E}[m]}{\text{K}[m]} \right) \right]^{-i}, \quad (2.18)$$

$i$	0	1	2	3	4	5	6	7	8
$a_i$	0	1	$-\frac{1}{8}$	$-\frac{1}{32}$	$-\frac{11}{1024}$	$-\frac{17}{4096}$	$-\frac{55}{32768}$	$-\frac{179}{262144}$	$-\frac{9061}{33554432}$
$b_i$	1	$\frac{1}{2}$	$\frac{9}{32}$	$\frac{21}{128}$	$\frac{795}{8192}$	$\frac{945}{16384}$	$\frac{2247}{65536}$	$\frac{42639}{2097152}$	$\frac{6446547}{536870912}$
$d_i$	1	$\frac{5}{8}$	$\frac{27}{64}$	$\frac{295}{1024}$	$\frac{1605}{8192}$	$\frac{2163}{16384}$	$\frac{92253}{1048576}$	$\frac{1944495}{33554432}$	$\frac{20252835}{536870912}$

**Table 2.1:** Coefficients for several series-expansions occurring in this chapter. The associated functions are displayed in Fig. 2.2. The naming of the coefficients is consistent with Hu *et al* [108]. The coefficients  $c_i$  are not given because they deal with the stress across the bilayer,  $f_y$ , which is discussed in the paper but not in this chapter.

but the faster way is to insert Eq. (2.16) into Eq. (2.17), expand the right hand side in  $\gamma$ , and compare the coefficients on both sides. We find that

$$m(\gamma) = \gamma - \frac{1}{8}\gamma^2 - \frac{1}{32}\gamma^3 - \frac{11}{1024}\gamma^4 \dots \quad (2.19)$$

Table 2.1 provides the coefficients for  $m$  as well as other important series expansions in this chapter up to  $i = 8$ .

### 2.1.3 Stress-Strain Relationship

Now that we can express  $m$  in terms of  $\gamma$ , we can use Eq. (2.15) to find  $f_x(\gamma)$ :

$$f_x(\gamma) = \kappa \left( \frac{4}{L} K[m(\gamma)] \right)^2 = \kappa \left( \frac{2\pi}{L} \right)^2 \sum_{i=0}^{\infty} b_i \gamma^i \quad (2.20a)$$

$$= \kappa \left( \frac{2\pi}{L} \right)^2 \left[ 1 + \frac{1}{2}\gamma + \frac{9}{32}\gamma^2 + \frac{21}{128}\gamma^3 \dots \right]. \quad (2.20b)$$

The first interesting thing about the stress is that it does not go to 0 as the strain approaches 0. Instead,  $\lim_{\gamma \rightarrow 0^+} f_x = \kappa \left( \frac{2\pi}{L} \right)^2$ , which is called the buckling threshold, since a flat membrane will only buckle if the stress on its ends is greater than or equal to the threshold. Next, we see that the stress always increases with  $\gamma$ , and for small strains we find

$$\frac{f_x(\gamma) - f_x(0)}{f_x(0)} = \frac{1}{2}\gamma + \mathcal{O}(\gamma^2). \quad (2.21)$$

The prefactor 1/2 does not depend on the type of boundary conditions of the buckle [9].

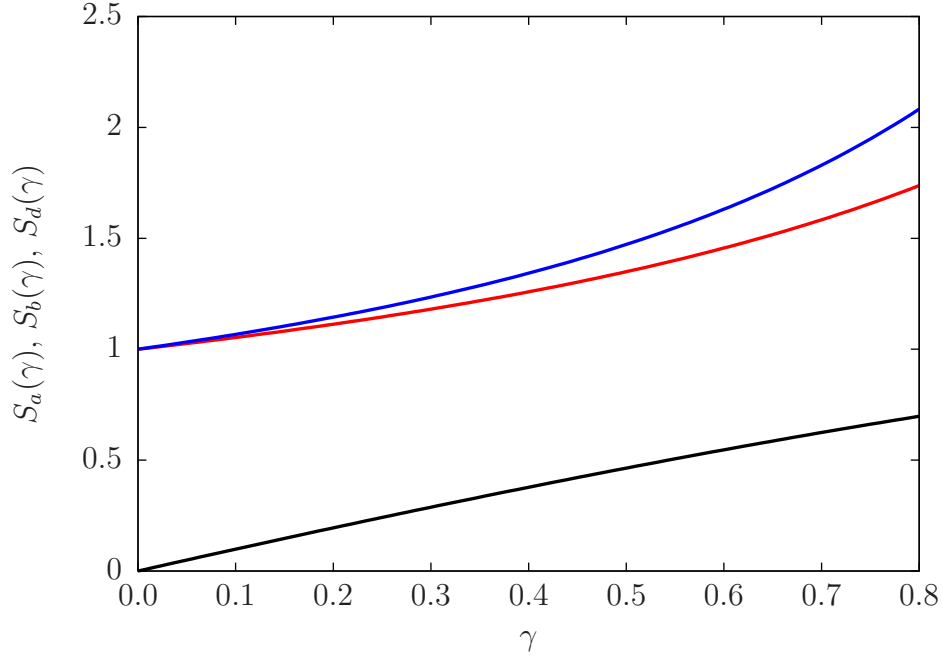


**Figure 2.2:** Sketch of the important series functions.  $S_a(\gamma) = m(\gamma) = \sum_{i=0}^{10} a_i \gamma^i$  is shown with the black solid line.  $S_b(\gamma) = \sum_{i=0}^{10} b_i \gamma^i$ , which is used to calculate  $f_x(\gamma)$  is shown in the red line.  $S_d(\gamma) = \sum_{i=0}^{10} d_i \gamma^i$ , which is used to calculate the fluctuation correction for  $f_x(\gamma)$  is shown in the blue line. The coefficients are given in Table 2.1.

We can now calculate the energy of the buckle as a function of strain by inserting Eq. (2.20a) and Eq. (2.17) into Eq. (2.10):

$$\mathcal{E} = \kappa(2\pi)^2 \frac{L_y^2}{A} \sum_{i=0}^{\infty} \frac{b_i \gamma^{i+1}}{i+1}, \quad (2.22)$$

This will prove useful later in this chapter when we look at the energetics of the buckling simulations.

Unlike sheets of solid material, the fluid lipid membranes also exert forces along the buckle ridges ( $y$ -direction). The strength of these forces can be found by differentiating the energy in Eq. (2.22) with respect to  $L_y$ . It turns out that the stress-strain relation in the  $y$ -direction is more difficult to measure, leading to a less precise determination of the bending modulus. For this reason, I will not go into the derivation of the forces in the  $y$ -direction. For interested readers, this information can be found in Hu *et al.* [108].

### 2.1.4 Isotropic stress

We now show a second derivation of the stress-strain relation using the stress tensor. With this derivation we will also be able to identify the isotropic stress of the buckles. We start by imagining a cut through the membrane at a given point along a chosen tangential direction  $\mathbf{t}$ . Let  $\mathbf{l}$  be a vector perpendicular to the cut and tangential to the membrane, and  $\mathbf{n}$  be the local membrane normal. The three vectors  $\{\mathbf{t}, \mathbf{l}, \mathbf{n}\}$  form a local orthonormal coordinate system.

We now imagine that the membrane on one side of the cut is removed and look at the force per unit length,  $\mathbf{f}$ , along the cut (in equilibrium, this force would be balanced by the removed part of the membrane). Expanding  $\mathbf{f}$  in the local coordinate system gives [108]:

$$\mathbf{f} = \left[ \frac{1}{2}\kappa (K_{\perp}^2 - K_{\parallel}^2) - \Sigma \right] \mathbf{l} + \kappa [K_{\perp\parallel}(K_{\perp} + K_{\parallel})] \mathbf{t} - \kappa(\nabla_{\perp}K)\mathbf{n}, \quad (2.23)$$

where  $K_{\perp}$  and  $K_{\parallel}$  are the local curvatures perpendicular and parallel to the cut,  $K_{\perp\parallel}$  is the off-diagonal element of the local curvature tensor,  $\nabla_{\perp}$  is the directional surface derivative along  $\mathbf{l}$ , and  $\Sigma$  is the isotropic tension.  $\Sigma$  is the curvature independent part of the surface stress. For ordinary fluid interfaces and films this is just the surface tension, but for the buckle  $\Sigma$  comes from the constraint linking the total and projected area. Also note that the contribution of  $\mathbf{f}$  along  $\mathbf{t}$  will vanish if we choose a cut where  $K_{\perp\parallel} = 0$ . This happens when  $\mathbf{t}$  points along a principal direction.

Specifically for a cut along the  $y$ -direction of a buckle,  $K_{\parallel} = K_{\perp\parallel} = 0$  and  $K_{\perp} = -\dot{\psi}$ , and Eq. (2.23) simplifies to:

$$\mathbf{f} = \left[ \frac{1}{2}\kappa\dot{\psi}^2 - \Sigma \right] \mathbf{l} + \kappa\ddot{\psi}\mathbf{n}. \quad (2.24)$$

The buckling stress  $f_x$  is just the projection of  $\mathbf{f}$  along the  $x$ -direction:

$$f_x = \left[ \frac{1}{2}\kappa\dot{\psi}^2 - \Sigma \right] \cos \psi - \kappa\ddot{\psi} \sin \psi. \quad (2.25)$$

Combining this with the Euler-Lagrange equation (2.8) and the first integral (2.9), we get an equation for  $\Sigma$ :

$$\Sigma = -f_x \cos \psi_i. \quad (2.26)$$

For  $\psi_i < \pi/2$ , this shows that  $\Sigma < 0$ , which confirms that the curvature-independent part of the membrane stress is initially compressive. As  $\gamma$  increases, we will eventually reach a point where  $\psi_i = \pi/2$  and there will be no isotropic stress in the buckle. This occurs when  $m = 1/2$ , which corresponds to a strain of  $\gamma = 2(1 - E[1/2]/K[1/2]) \approx 0.543$ . We must be careful to not confuse the isotropic stress with  $f_x$  or  $f_y$ , neither of which will vanish when  $\Sigma = 0$ . If we keep pushing the buckle,  $\Sigma$  becomes positive and a compressive force at the ends of the buckle leads to a tensile isotropic contribution to the overall stress.

### 2.1.5 Undulation correction for $f_x$

Thermal membrane undulations will affect the stresses of the buckle because the fluctuations shrink the projected surface area and contract the membrane. We can approximate the effect of the fluctuations with a flat membrane fluctuation theory. We will assume that there are no undulations in the  $y$ -direction, which is reasonable as long as we make  $L_y \ll L_x$ . Thus, we only need to look at fluctuations in the  $x$ -direction.

The undulations reduce the overall average arc length of the membrane (in both the flat and buckled state) by introducing wrinkles into the membrane. When we want to measure the length  $L$ , we measure the equilibrium box size  $L_x$  of a flat strip of membrane while no buckling force is applied. However, this is not the ground state length  $L_0$ . For the fluctuation correction, we first need to account for the difference between  $L$  and  $L_0$ .

We start by expanding the stress-free nearly-flat shape of a membrane,  $h(x)$ , as a Fourier series:

$$h(x) = \sum_q h_q e^{iqx}, \quad (2.27)$$

where  $q \in \frac{2\pi}{L}\mathbb{Z}$  and  $h_{-q} = h_q^*$ . The energy can now be expressed as:

$$\mathcal{E}[h] = L_y \int_0^L dx \left\{ \frac{1}{2} \kappa [h''(x)]^2 \right\}. \quad (2.28)$$

The equipartition gives the two-point correlation:

$$\langle h_q h_{q'}^* \rangle = \frac{k_B T}{L_y L \kappa q^4} \delta_{qq'}. \quad (2.29)$$

Up to quadratic order, the total arc length is then found to be

$$\frac{\langle L_0 \rangle}{L} = 1 + \frac{1}{2L} \int_0^L dx \langle [h'(x)]^2 \rangle = 1 + \frac{1}{2} \sum_q q^2 \langle |h_q|^2 \rangle = 1 + \frac{1}{2} \sum_q \frac{k_B T}{L_y L \kappa q^2}. \quad (2.30)$$

We can approximate this sum as an integral:

$$\frac{\langle L_0 \rangle}{L} \approx 1 + \frac{L}{2\pi} \int_{2\pi/L}^{\infty} dq \frac{k_B T}{L_y L \kappa q^2} = 1 + \frac{k_B T L}{(2\pi)^2 \kappa L_y} = 1 + \delta. \quad (2.31)$$

Thus the relative difference between  $\langle L_0 \rangle$  and  $L$  is given by the (hopefully small) parameter:

$$\delta = \frac{k_B T L}{(2\pi)^2 \kappa L_y}. \quad (2.32)$$

Using typical values for membranes, we find that it is normally on the order of 1% and hence indeed small.

We now want to replace  $L$  by  $L_0$  in the definition of  $\gamma$  and then Eq. (2.20). To linear order in  $\delta$ , we find

$$\langle L_0 \rangle^{-2} = L^{-2}[1 - 2\delta + \mathcal{O}(\delta^2)] , \quad (2.33a)$$

$$\gamma_0^i = \gamma^i + i\gamma^{i-1}(1 - \gamma)\delta + \mathcal{O}(\delta^2) . \quad (2.33b)$$

After some algebra, the fluctuation correction can be expressed as:

$$\delta f_x = -\frac{3k_B T}{2LL_y} \sum_{i=0}^{\infty} d_i \gamma^i \quad (2.34a)$$

$$= -\frac{3k_B T}{2LL_y} \left[ 1 + \frac{5}{8}\gamma + \frac{27}{64}\gamma^2 + \dots \right] , \quad (2.34b)$$

where the coefficients  $d_i = \frac{2}{3}[(i+2)b_i - (i+1)b_{i+1}]$  are listed in Table 2.1. To lowest order in  $\gamma$ , the ratio of the correction to the ground state stress is

$$\left| \frac{\delta f_x}{f_x} \right| \approx \frac{3}{8\pi^2} \times \frac{L}{L_y} \times \frac{k_B T}{\kappa} . \quad (2.35)$$

For the simulations we perform, this effect is in the percent range and thus barely affects the results for  $f_x$ .

## 2.2 Summary of Buckling Theory

Let us now summarize the main results for both the shape and the stress-strain relation. The shape of the membrane is expressed in the parametric form:

$$x(s) = 2\lambda \text{E}[\text{am}[s/\lambda, m], m] - s , \quad (2.36a)$$

$$z(s) = 2\lambda \sqrt{m} (1 - \text{cn}[s/\lambda, m]) . \quad (2.36b)$$

The parameter  $\lambda = \sqrt{\kappa/f_x}$  can be expressed as

$$\lambda = \frac{L}{2\pi} \sqrt{\sum_{i=0}^{\infty} b_i \gamma^i} \quad (2.37)$$

The stress-strain relation with the fluctuation correction along the buckle is

$$f_x(\gamma) = \kappa \left( \frac{2\pi}{L} \right)^2 \sum_{i=0}^{\infty} b_i \gamma^i - \frac{3k_B T}{2LL_y} \sum_{i=0}^{\infty} d_i \gamma^i . \quad (2.38)$$

Finally, the energy of the compressed buckle is:

$$\mathcal{E} = \frac{4\pi^2 \kappa L_y}{L} \sum_{i=1}^{\infty} \frac{b_{i-1}}{i} \gamma^i \quad (2.39)$$

## 2.3 Simulation Setup

We now discuss the setup for the molecular dynamics simulations. We start with some theoretical considerations, move to practical considerations, and finally describe the outcomes of the simulations themselves.

### 2.3.1 Theoretical Considerations

One thing to take into consideration is the maximum curvature of the buckle. It has been shown that there is a slight curvature-dependence on the effective rigidity of fluid membranes [93]. From Eq. (2.9), we see that  $R_{\min} = \dot{\psi}_{\max} = \dot{\psi}(0) = 2\sqrt{m}/\lambda$ . By combining this equation with Eq. (2.15) and Eq. (2.17) we find that

$$\frac{L}{R_{\min}} = 8\sqrt{m(\gamma)}K[m(\gamma)] \quad (2.40a)$$

$$= 4\pi\sqrt{\gamma} \left[ 1 + \frac{3}{16}\gamma + \frac{39}{512}\gamma^2 + \frac{303}{8192}\gamma^3 \right]. \quad (2.40b)$$

For example, at  $\gamma = 0.5$ ,  $R_{\min}$  is 10 times smaller than  $L$ . Thus, if we want to limit our simulations to stay below a maximum curvature over a range of strains, we know how long the membrane must be.

Also, the fluctuation analysis that we choose assumes that there are no fluctuations in the  $y$ -direction, thus we need to simulate strips of membrane with  $L_y \ll L$ . This is actually a bonus, since it means that we can simulate fewer lipids and makes the method more efficient. We still need  $L_y$  to be large enough so that a lipid does not directly interact with its mirror images from the periodic boundary conditions and to avoid finite size effects. For example, the simulations of the Cooke membrane,  $L_y = 12.0\sigma$ , while  $L_x = 66.75\sigma$ . With this value for  $L_y$ , the strip has around 10 lipids across. This thin strip is 0.18 times smaller than a square membrane.

### 2.3.2 Creating the Buckles

The first step in the process is to create buckles at different strains. We will discuss four different techniques: active compression, back-mapping, approximate transformation, and exact transformation. All methods have been used to varying degrees of success. The exact transformation has shown the most success in terms of how fast the buckles can reach equilibrium.

#### Active compression

The first technique is to use active compression to create the buckle. The idea is to slowly reduce the box length in the  $x$ -direction until the membrane buckles, and then continue to push until we have reached the desired buckling strain. This can be done

in two ways: (1) apply a barostat with excess pressure along the  $x$ -direction, and (2) shrink the box length in small steps while allowing the membrane to relax between each box shrinking step.

For implicit solvent models, we do not have to worry about the  $z$ -direction, as long as  $L_z$  is large enough for the buckle to not interact with its periodic image. For explicit solvent models, we need to increase  $L_z$  as we decrease  $L_x$  to ensure that the solvent density remains unchanged. This can be accomplished by applying a barostat along the  $z$ -direction.

Active compression can cause major problems when we start with a flat membrane. As we push a flat membrane past the buckling threshold, we break the symmetry in creating the buckle. When this happens, we might excite higher order buckling modes, that are unstable, but require time to decay. This can be avoided by explicitly breaking the symmetry ahead of time by pre-imposing a small buckle on the membrane (through a coordinate transformation discussed below) and then create the larger buckle using active compression.

### Back-mapping from a buckled lower resolution model

If we already have a low resolution course-grained buckle, we can create buckles for a new model by back-mapping from the old. The only requirement is that the aspect ratios of the lipids in each model are close to each other. This was used to create the first early MARTINI buckles. There is a built-in GROMACS routine that is described in Rzepiala *et al.* [110]. This method works well when we already have a low resolution model in equilibrium then can be back-mapped easily into a high resolution so that the high resolution model can quickly reach equilibrium.

### Approximate transformation of a flat membrane

For small strain ( $\gamma \lesssim 0.2$ ), the buckle shape can be reasonably approximated using a cosine function:

$$\begin{pmatrix} x \\ y \\ z \end{pmatrix} \rightarrow \begin{pmatrix} x L_x/L \\ y \\ z + z_a \cos(2\pi x/L) \end{pmatrix}, \quad (2.41)$$

where the buckling amplitude is given by

$$z_a = 2\lambda\sqrt{m(\gamma)} = \frac{L}{\pi} \sqrt{\frac{\sum_{i=0}^{\infty} a_i \gamma^i}{\sum_{i=0}^{\infty} b_i \gamma^i}} \quad (2.42a)$$

$$= \frac{L\sqrt{\gamma}}{\pi} \left[ 1 - \frac{5}{16}\gamma - \frac{25}{512}\gamma^2 - \frac{121}{8192}\gamma^3 \dots \right]. \quad (2.42b)$$

This simple transformation does not take into account the correct tilt of the lipids and the approximation becomes less accurate as  $\gamma$  increases. The first Plum buckles

were created by first creating small buckles using this method and then actively compressing them.

### Exact transformation of a flat membrane

The best way to create the buckles is to transform the positions of the lipids in a flat bilayer to their theoretical position. Specifically, for each lipid we first need to choose a position to represent the lipid. A point close to the pivotal plane [111] appears to be a reasonable choice; we chose the middle bead for the Cooke model, the C1A bead for MARTINI, and AS12 bead for the Plum model. We then use the  $x$ -position of this point as the arc length, and then translate each particle of the lipid using the theoretical shape equations (2.14). Using Eq. (2.13), we can calculate the angle of the normal vector of the lipid to the buckle with respect to the  $x$ -axis. We use this angle to rotate the lipid about the central position of the lipid.

For all models, it is necessary to follow the transformation with a short warm-up simulation with softened potentials to relax overlap in the tail regions of the lipids. For explicit solvent models, we buckle the solvent-free system and then add the solvent afterwards.

### 2.3.3 Simulation Parameters

Table 2.3.3 summarizes the important parameters of the simulations: model type, temperature, number of lipids, solvent, and box lengths. For the Cooke model, we used the “standard” values for the simulation length and energy units, specifically,  $w_c/\sigma = 1.6$  and  $k_B T/\epsilon = 1.1$ . The simulations were performed in ESPRESSO [112] with a Langevin thermostat [113], and a time step  $\delta t = 0.002\tau$ .

The MARTINI DMPC model was simulated using GROMACS 4.5 [114]. A Berendsen thermostat [115] with a time constant  $\tau_T = 1$  ps and reference temperature  $T = 300$  K. The time step was  $\delta t = 20$  fs. The Lennard-Jones and Coulomb cutoffs were 1.2 nm, and the neighbor list ranged up to 1.2 nm; it was updated every 10 steps. A Berendsen barostat [115] was also used with  $P_x = P_y = P_z = 1$  bar and  $\kappa_{T,x} = \kappa_{T,y} = 0$  (which keeps  $L_x$  and  $L_y$  fixed),  $\kappa_{T,z} = 3 \times 10^{-5}$  Pa.

The Plum DOPC model was simulated using ESPRESSO [112] with simulation units  $\sigma = 1$  Å, energy  $\epsilon = k_B T \approx 4.28 \times 10^{-21}$  J at  $T = 310$  K, and time  $\tau = 0.062$  ps. The time step is  $\delta t = 0.02\tau$ . A DPD thermostat [116] was used with a friction coefficient  $\gamma_f = 1\tau^{-1}$ , a cutoff of 15 Å, and a time constant  $\tau_T = 0.02\tau$ .

## 2.4 Simulation Results

We now apply the theoretical analysis from section 2.1 to the simulation results. First, we will look at the stress-strain relation for each model, from which we can derive the bending modulus. Next, we look at the shape of the buckles and discuss how to

Model	lipid	$T$	$\frac{\text{beads}}{\text{lipid}}$	$N_{\text{lipids}}$	$N_{\text{solvent}}$	$L$	$L_y$
Cooke	$w_c/\sigma = 1.6$	$1.1 \epsilon/k_B$	3	1344	—	$66.75 \sigma$	$12.0 \sigma$
MARTINI	DMPC	300 K	10	1120	19 623 1 bead=4 H <sub>2</sub> O	46.75 nm	7.1 nm
Plum	DOPC	310 K	17	902	—	48.5 nm	7.1 nm

**Table 2.2:** Summary of the properties of the three lipid models compared in this section.

compare the theoretical shape to the simulation data. Finally, we explore the energetics of the simulations and use the results to extract the temperature dependence of the bending modulus.

### 2.4.1 Stress-Strain Relation

We start with the stress-strain relation (2.20) for the three models from which we can infer the value of  $\kappa$ . The results are shown in Fig. 2.3, Fig. 2.4, Fig. 2.5 for the Cooke, MARTINI and Plum buckles respectively. We see that the fluctuation correction in the  $x$ -direction is indeed small. Also, the deviation between data and theory is larger at small strains ( $\gamma < 0.05$ ) for the Cooke model, which might be caused by the compressive stress having a relatively larger effect at smaller strains, or by another effect that we first discuss in Ch. 3

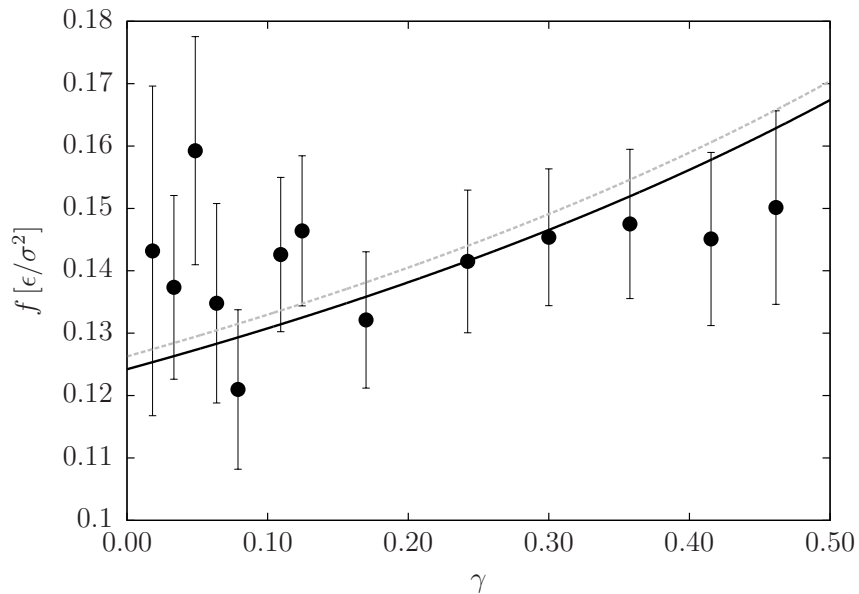


**Figure 2.3:** The stress-strain relationship for the Cooke model. The filled circles are the measured stress in the  $x$ -direction (along the buckle). The black line is the theoretical fit including the fluctuation correction, with  $\kappa$  as the fitting parameter. The gray dotted line is the prediction without the fluctuation correction.

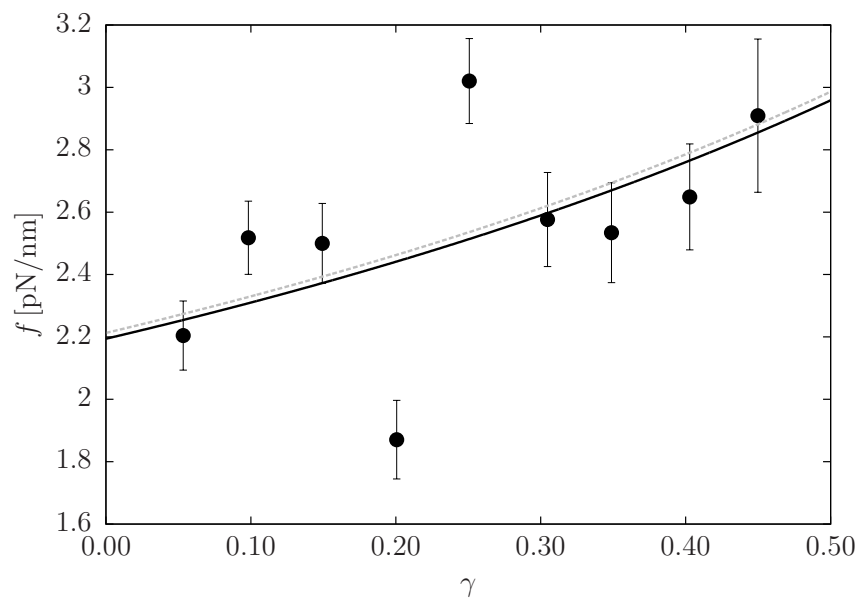


**Figure 2.4:** The stress-strain relationship for the MARTINI model.

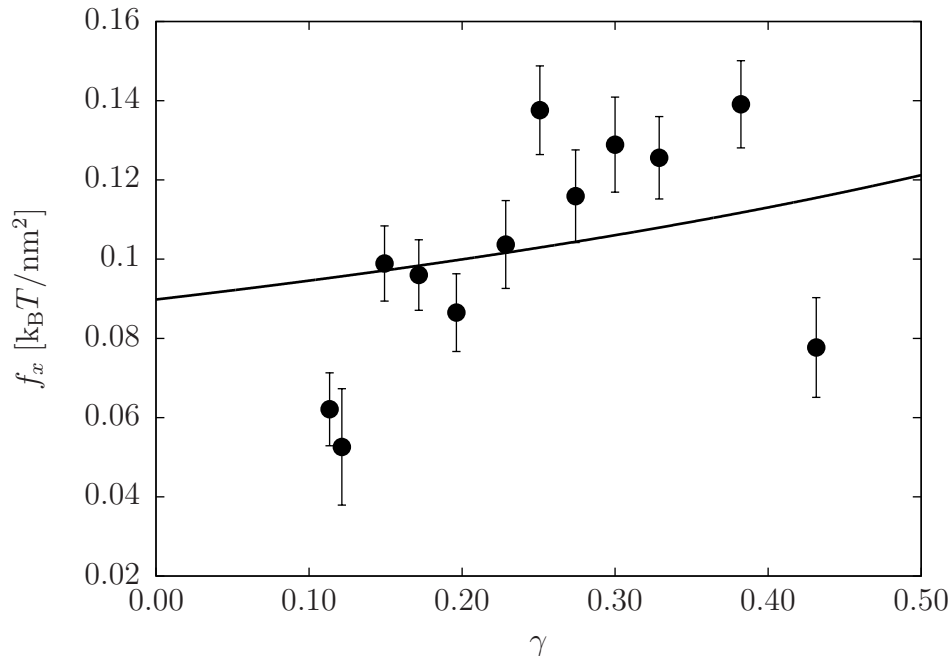


**Figure 2.5:** The stress-strain relationship for the Plum model. The theory does a poorer job describing the Plum model than the other models.

From the stress-strain relation, we obtain values for  $\kappa$  for each model, which are presented in Table 2.3. The table also includes a list of previous results for the models except for the Plum DOPC model, for which the bending modulus has not been measured. The bending modulus for Plum POPC has been measured [60], but we were unable to successfully apply the buckling protocol to the Plum POPC model because the simulations never reached an equilibrium value, despite the fact that they were run longer than for the other models. The stress would continue to randomly jump during the simulations which coincided with defects forming in the membrane. More success was found using the Plum DOPC model, which is the model that we will discuss.

For the Cooke model, the result using the buckling method agrees within error bars with two of the three previous reported results. The one exception [103] is lower compared to the other measurements. It was performed with the tether method and included results from tethers with large curvatures. The error of those values did not justify a curvature-dependent fit, but later work [79] with more accurate results showed the need for a curvature-dependent effective rigidity. When the old data is reanalyzed with the correction, the new value shifts into agreement with the other results,  $\kappa = (11.9 \pm 0.7) k_B T$ . For MARTINI DMPC, the value of the bending modulus is smaller than previous measurements derived from undulation measurements.

Model	$\kappa/k_B T$	$\kappa/k_B T$ [Ref], method
		$11.7 \pm 0.2$ [103], T
Cooke	$12.8 \pm 0.4$	$12.5 \pm 1$ [103], HF
		$12.44 \pm 0.26$ [79], T
		36 [92], HF
MARTINI	$29.0 \pm 1.0$	40.3 [117], HF
		40.5 [80], HF
PLUM	$5.49 \pm 0.4$	—

**Table 2.3:** Summary of the measured bending rigidity  $\kappa$  as derived from the buckling stress in  $x$ -direction. Various previous results for  $\kappa$  using different methods (HF for height fluctuation methods and T for using the force along a tether) are given in the last column.

## 2.4.2 Getting the Shape of Buckled Membranes

As shown in subsection 2.1.1, the theory predicts the shape of the buckled membrane in addition to the stress-strain relation. The shape of the buckle does not depend on the material parameters of the membrane, so we cannot use it to extract information about  $\kappa$ , but it does act as an important check for how well the theory describes the buckles.

In order to compare the shape of the simulated buckle to the theory, we must relate two thick monolayers of discrete lipids to a continuous two dimensional sheet. Therefore, we need to project the position of each lipid to the midplane. We resolve this by first treating the position of each lipid as the position of one or the average of a few particles of the lipid. Specifically, we want the position to be close to the pivotal plane value. At the start of the project, we did not have a good value for the position of the pivotal plane, so we made an guess. For the Cooke model, we choose the position of the middle bead. For the MARTINI model, we choose the average position of the two CA beads (the first carbon group of each tail). For the PLUM model, we choose the average of AS11 and AS21. Next, we find the vector that connects the head of the lipid to the tails. For the Cooke model, this is simply the vector between the head bead and the second tail bead. For the MARTINI model, we use the vector between the P04 bead and the average of the C3A and C3B beads (bottom tail beads). For the PLUM model, we choose the vector between the GL bead and the average of the AS15 and AS25 beads.

Finally, we shift the position of the reference bead in the direction of this vector by the average distance from the particle to the midplane, which was found using a flat membrane. Fig. 2.6 shows the original position and the projected position of the middle bead from a snapshot of a Cooke simulation. After we project the lipids to the midplane, we shift the membrane so that the minimum value in the  $z$ -direction is at  $x = 0$ , so that we are consistent in how we look at different snapshots of the same

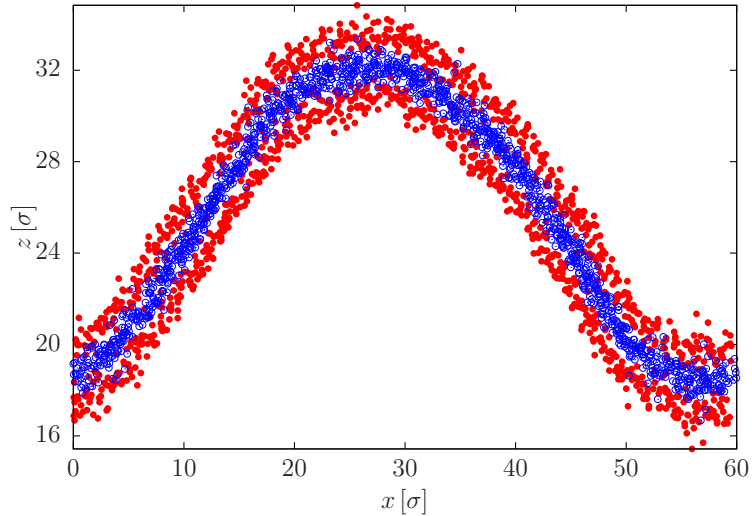


**Figure 2.6:** The position of the middle bead in a Cooke buckle bilayer. The red solid circles are the original position of the beads. The blue open circles are the positions after they have been shifted to the midplane. Note that the  $x$ - and  $z$ -directions are not to scale.

buckle. Fig. 2.7 shows a snapshot of the Cooke model before and after the membrane has been shifted.

There are a couple of different ways to get the shape from here. The easiest way is to bin the particles and then take their average position in the  $z$ -direction. There are two problems with this technique. First, this does not give a continuous function that could aid in future analysis. Second, the bin size can have a subtle effect on the final result. If the bins are too small, there may be too much noise in the shape. If the bins are too large, we will underestimate the sharpness of the buckle at the local maximum and minimum parts of the buckle.

One potential way is to fit using smoothing splines [118]. The main difficulty with splines is storing and transferring the coefficients that describe the spline to other programs for later analysis.

The periodicity of the buckles makes expanding the shape as a Fourier series attractive. The most straightforward way to obtain the coefficients would be to bin the particles and then perform numerical integration, but the binning still can cause problems. Instead, we fit the particles to a Fourier series using  $\chi^2$  minimization. This changes the value of the coefficients by a small amount (on the order of a percent) compared to binning and integrating.

We still need to determine how many terms we should use: too few and we cannot properly describe the shape, but too many terms will lead to over-fitting and capture the noise from the simulation. We determined the valid coefficient range by measuring the length of the buckle for different numbers of coefficients. Fig. 2.8 shows how the

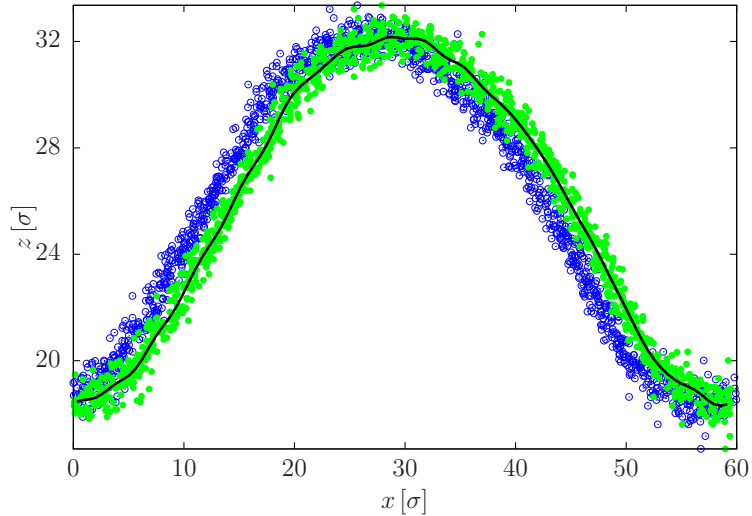


**Figure 2.7:** This figure shows how a Cooke membrane is shifted. The blue open circles are the positions of the middle beads after they are shifted toward the midplane. The green solid circles are the positions of the beads after the minimum of the buckle has been shifted to  $x = 0$ . The minimum is found by averaging the positions of all beads with  $z$ -position within 5 percent of the  $z$ -position of the bead with the minimum position. The black line is the Fourier series fit. Note that the  $x$ - and  $z$ -directions are not to scale.

length changes with the number of Fourier coefficients for the Cooke a Cooke buckle. Initially, the length should change as more terms are added, but it will then settle at a fixed length, only to then increase again as the new terms only add wiggles due to the noise.

The membrane fluctuates during the simulation, so that it often does not look like the theoretical shape at a specific point in time. Fig. 2.9, Fig. 2.10, and Fig. 2.11 show the range of fluctuations that a membrane undergoes during a simulation for the Cooke, MARTINI, and Plum models, respectively. For all three models, the membranes fluctuate around a buckle shape. The Plum model shows the most fluctuations; the MARTINI model shows the least, and the Cooke model is in between. When we measure the bending modulus, it will come as no surprise that the Plum model has the smallest and the MARTINI model has the largest bending modulus. The extent of fluctuations for the Plum model makes analyzing the shape more difficult than for the other models.

To remove fluctuations, we average the coefficients for each snapshot. It is easy to see that averaging the coefficients is the same as averaging the shapes:

$$\langle z(x) \rangle = \left\langle \sum_n a_n \cos \left( \frac{2\pi n x}{L} \right) \right\rangle = \sum_n \langle a_n \rangle \cos \left( \frac{2\pi n x}{L} \right). \quad (2.43)$$

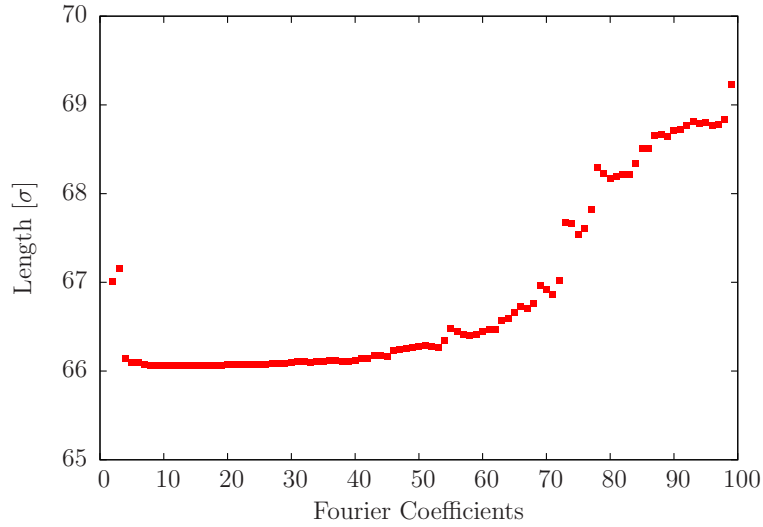


**Figure 2.8:** The length of the Fourier series fit as a function of the number of terms in the series. The length reaches a peak at the third coefficient (the results for one coefficient is not shown) before settling at a lower value for a range of coefficients. After 20 coefficients, the length begins to increase, signifying that the fit is beginning to over-fit the noise in the simulation. From this graph, we would expect that using between 10 and 20 coefficients should give the best results.

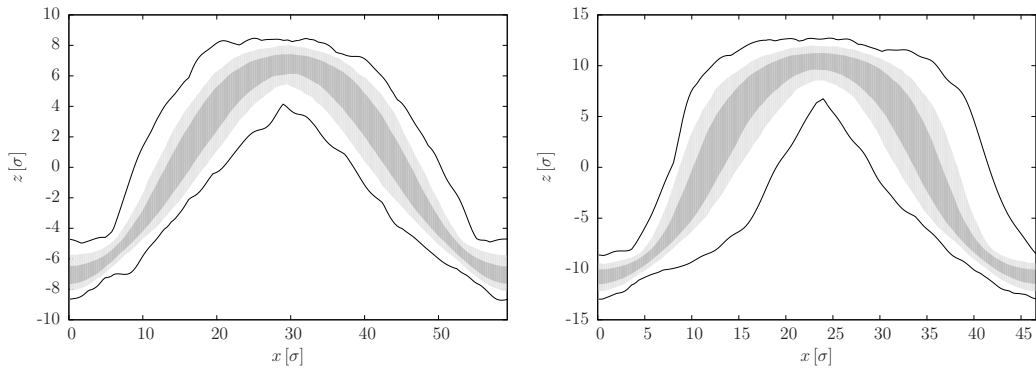


**Figure 2.9:** The graph shows the range in shapes for the Cooke membrane at two different strains (Left:  $\gamma = 0.11$ ; Right:  $\gamma = 0.29$ ) as it fluctuates. For each snapshot, the membrane is first shifted so that its minimum is at  $x = 0 \sigma$  and the shape is centered so that the middle of the membrane is at  $z = 0 \sigma$ . 68 percent of the membrane snapshots fall in the dark grey band. 95 percent fall in the light grey band. The two black lines are the maximum and minimum position of the membrane over the simulation.

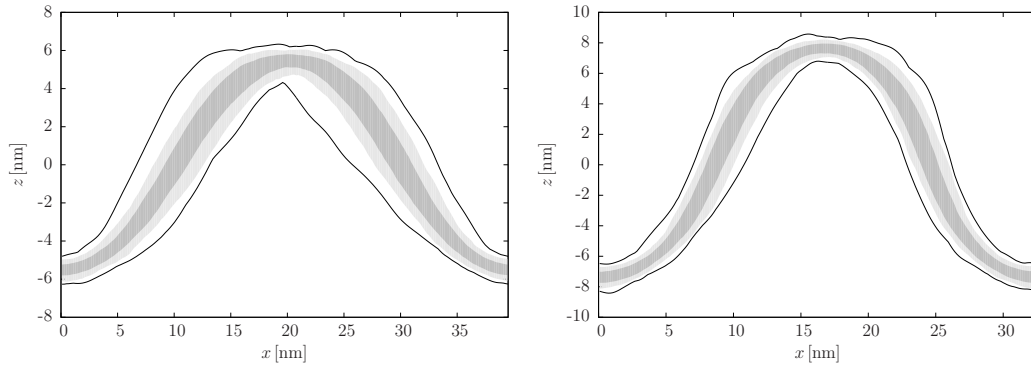


**Figure 2.10:** The graph shows the range in shapes of a MARTINI membrane as it fluctuates. Left:  $\gamma = 0.15$ . Right:  $\gamma = 0.30$ . The alignment of the membrane for each snapshot and the colors are the same as in Fig. 2.9.

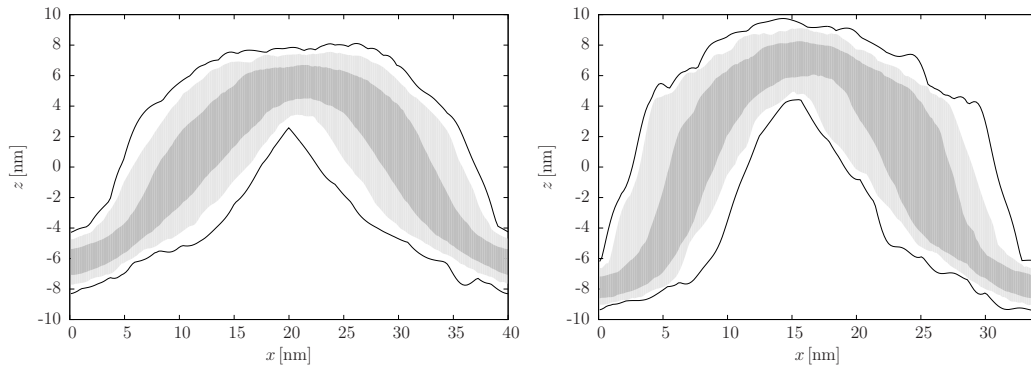


**Figure 2.11:** The graph shows the range in shapes of a Plum membrane as it fluctuates. Left:  $\gamma = 0.16$ . Right:  $\gamma = 0.28$ . The alignment of the membrane for each snapshot and the colors are the same as in Fig. 2.9.

To increase our sampling of fluctuations and improve the averaging, we enforce the symmetries which we know exist in equilibrium. Practically, this means that we perform three reflections of the shape from each snapshot. Specifically, we reflect the buckle around  $x = L_x/2$ , reflect around  $y = L_y/2$  and shifting the membrane in the  $x$ -direction by  $L_x$ , and finally, reflect around  $y = L_y/2$ , shifting the membrane in the  $x$ -direction by  $L_x$ , and then reflecting the membrane around  $x = L_x/2$ . This is visualized in Fig. 2.12

### 2.4.3 Shape of Buckles

Now that we have the simulation shapes, we check to see how well the theoretical prediction matches the shapes. Figs. 2.13, 2.14, and 2.15 show the average shape for the Cooke model at  $\gamma = 0.11$ , the MARTINI model at  $\gamma = 0.15$ , and the PLUM model at  $\gamma = 0.12$  respectively. For all three models, the theory successfully predicts

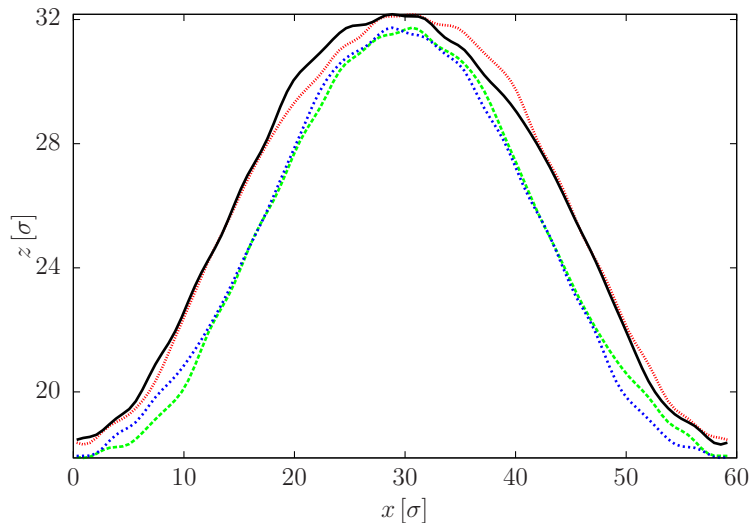


**Figure 2.12:** This figure shows the four shapes derived from one snapshot of a simulation. The black solid line is the fit from the original particles. The red line is the fit from reflecting the particles about the line  $x = L_x/2$ . The blue line is from reflecting the particles about the line  $y = L_y/2$  and shifting the particles. The green line is from reflecting the particles about the line  $y = L_y/2$ , shifting, and then reflecting about  $x = L_x/2$ .

the simulation shape for these strains. As the strain increases, the deviation between simulation and theory increases. This can be quantified by looking at the root mean squared deviation (RMSD) between the two:

$$\text{RMSD} = \sqrt{\frac{1}{L_x} \int_0^{L_x} dx [z_{\text{theory}}(x) - z_{\text{simulation}}(x)]^2}. \quad (2.44)$$

Figs. 2.16 and 2.18 show the RMSD as a function of strain for the Cooke and PLUM simulations respectively. This suggests that higher order corrections of the curvature might be needed at large strains, and we will discuss this further in Chapter 4.

## 2.5 Energetics of Fluid Membranes

An analysis of the energy of the buckled membranes provides insight into the temperature dependence of the bending rigidity near the simulation temperature. We first compare the *free* energy  $\mathcal{E}(\gamma)$  to the potential energy  $E(\gamma)$  as a function of strain from the simulations. The free energy of the buckle is found by integrating the stress-strain relation which we have previously calculated in Eq. (2.22).

The potential energy of the membrane can be calculated directly from the simulation. We set  $E(\gamma = 0) = 0$ . For implicit solvent models, we can just find the total

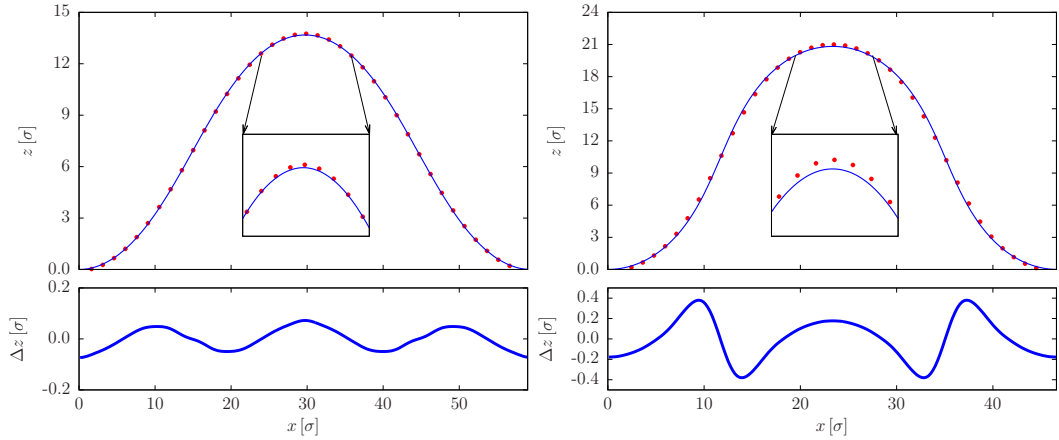


**Figure 2.13:** Comparison between the average simulated and theoretical buckle shape for a Cooke membrane. Top-left: The average shape of the Cooke model buckle at  $\gamma = 0.11$  is shown with red circles. The blue line is the predicted Euler buckle shape. Bottom-left: The residual between the simulation and the theory. The theory does a good job matching the simulation shape with a RMSD of  $0.038 \sigma$ . Recall that there is no fitting parameter for the theory, so this is a true prediction. Top-right: The average shape of the Cooke model buckle at  $\gamma = 0.29$ . Bottom-right: The residual between the simulation and the theory. The deviation between the theory and simulation shape is greater for this larger strain. The RMSD is  $0.17 \sigma$ .

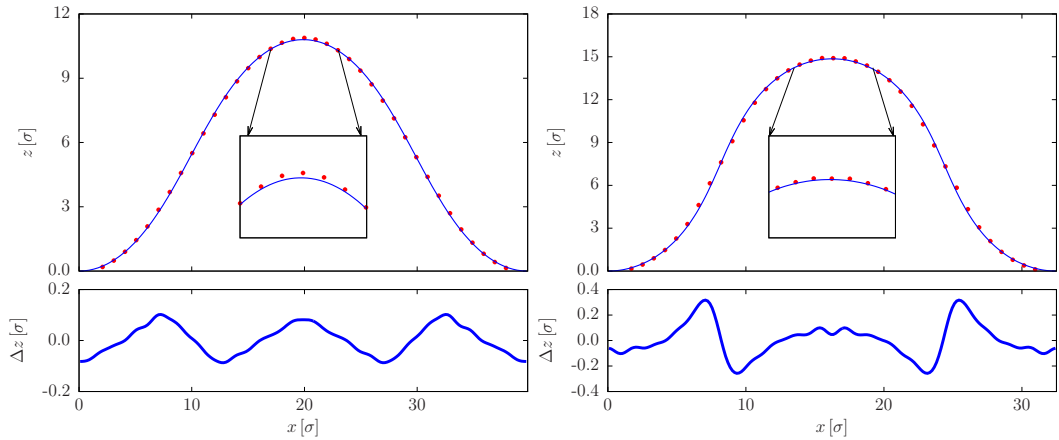


**Figure 2.14:** Comparison between the average simulated and theoretical buckle shape for a MARTINI membrane. Top-Left: The average shape of the Cooke model buckle at  $\gamma = 0.15$  is shown with red circles. The blue line is the predicted Euler buckle shape. Bottom-Left: The residual between the simulation and the theory. The RMSD is  $0.053 \sigma$ . Top-Right: The average shape of the Cooke model buckle at  $\gamma = 0.30$  is shown with red circles. The blue line is the predicted Euler buckle shape. Bottom-Right: The residual between the simulation and the theory. The RMSD is  $0.11 \sigma$ .

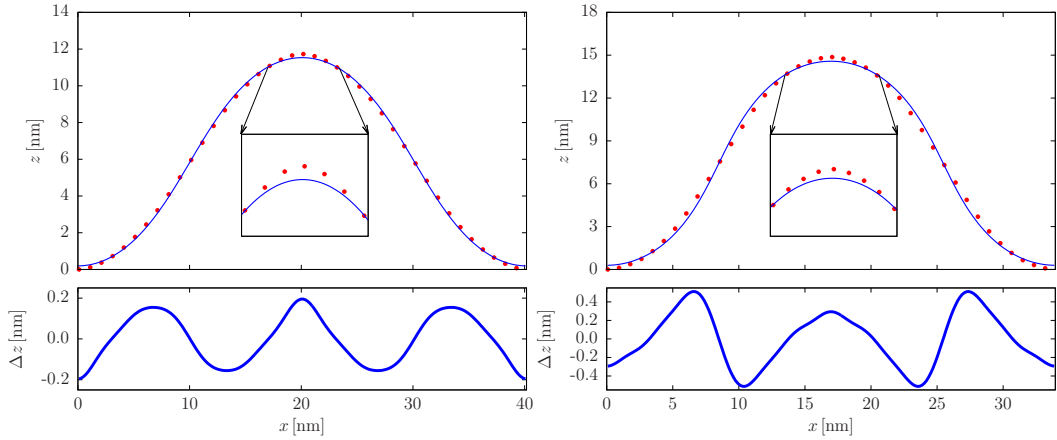


**Figure 2.15:** Comparison between the average simulated and theoretical buckle shape for a PLUM membrane. Top-Left: The average shape of the PLUM model buckle at  $\gamma = 0.16$  is shown in red circles. The blue line is the predicted Euler buckle shape. Bottom-Left: The residual between the simulation and the theory. The RMSD is  $0.11\sigma$ . Top-Right: The average shape of the PLUM model buckle at  $\gamma = 0.28$  is shown in red circles. The blue line is the predicted Euler buckle shape. Bottom-Right: The residual between the simulation and the theory. The RMSD is  $0.25\sigma$ .

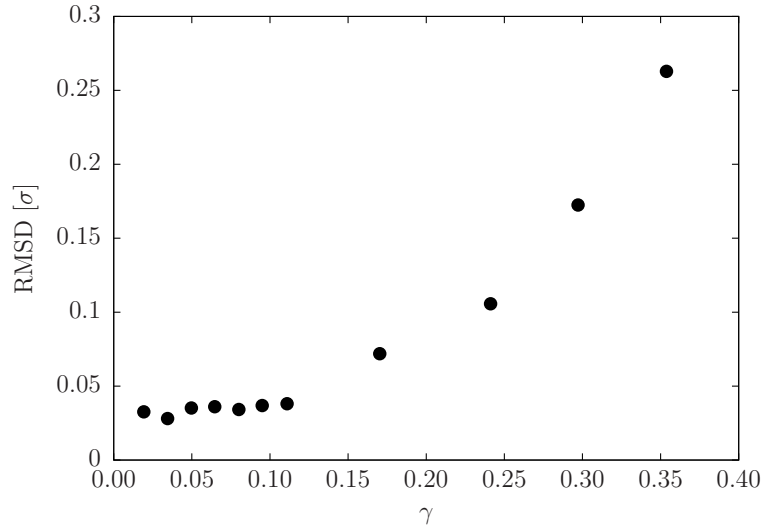


**Figure 2.16:** The RMSD from the shape prediction at different strains for the Cooke model. At low strain, the RMSD is very small which is impressive considering that there is no fitting parameter for the figure. As the strain increases, the difference between the simulation and theoretical shapes increase. For the larger strains, the method we use to measure the shape of simulations can no longer be used because the membrane can have overhangs.

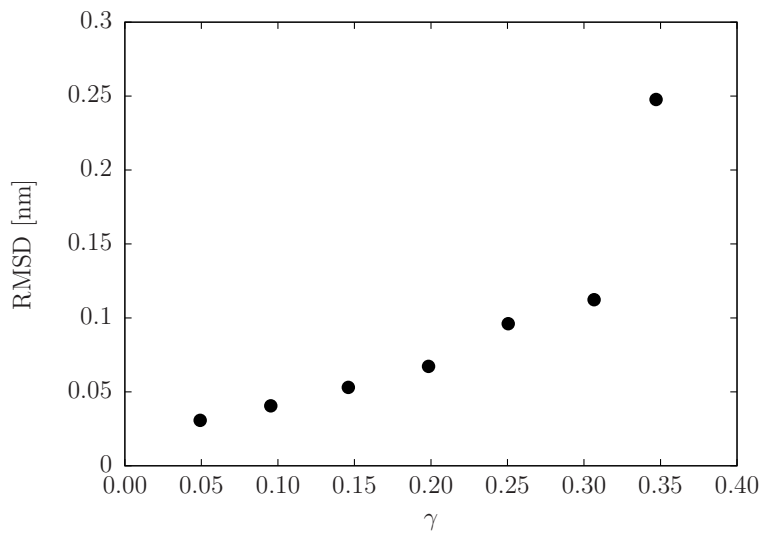


**Figure 2.17:** The RMSD from the shape prediction at different strains for the Martini model. Much like the Cooke model, at low strain the RMSD is very small but increases with strain. There is a large jump in the RMSD between  $\gamma = 0.3$  and  $\gamma = 0.35$ .

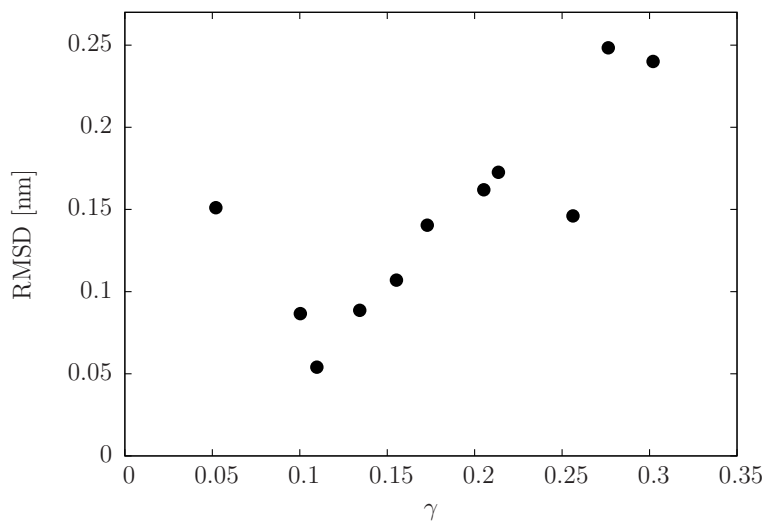


**Figure 2.18:** The RMSD from the shape prediction at different strains for the PLUM model. Outside of the buckle at  $\gamma = 0.04$ , the RMSD of the buckles increases with strain.

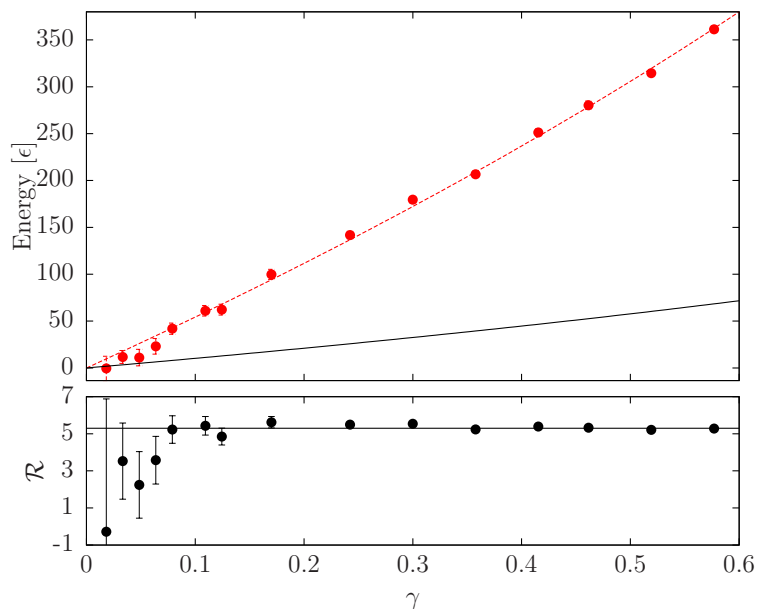


**Figure 2.19:** Top: Comparison of the energy,  $E_{\text{sim}}$ , of the Cooke model buckling simulations (filled red circles) with the free energy,  $\mathcal{E}(\gamma)$ , of the buckles (solid black line). The energy is shifted so that at zero strain the energy vanishes. The free energy was calculated using Eq. (2.39) with  $\kappa = 12.8 k_{\text{B}}T$ . The dashed red line comes from fitting the energy to the equation  $E_{\text{sim}} = E_0 + \mathcal{R}\mathcal{E}(\gamma)$  with  $E_0$  and  $\mathcal{R}$  as fitting parameters. Bottom: The ratio between the simulation energy and the buckling free energy is shown. The ratio is approximately constant.

potential energy in the simulation and then shift the energies by a constant factor. For explicit solvent models, we have to worry about the potential energy contribution of the solvent. If we keep the number of solvent molecules constant, then the solvent potential energy should be the same for every simulation, and we can remove it by shifting the energy for each simulation. However, fixing the number of solvent molecules for all  $\gamma$  will make the simulations less efficient, because most simulations will have more solvent than necessary.

Fig. 2.19 shows the energetics for the Cooke model. The figure shows that, as  $\gamma$  increases, the energy and free energy also increases. This is not surprising given that we have to do work on the system to buckle a membrane. Second, the *free* energy is always less than the potential energy, which means that the entropy  $S(\gamma)$  favors bending. Finally, the ratio of the energy to the free energy,

$$\mathcal{R} = \frac{E_{\text{pot}}(\gamma)}{\mathcal{E}(\gamma)}, \quad (2.45)$$

is essentially constant. The compression of the membranes at low strains causes the deviation in the ratio. Figs. 2.20 and 2.21 show the energetics for the MARTINI and PLUM simulations, respectively.

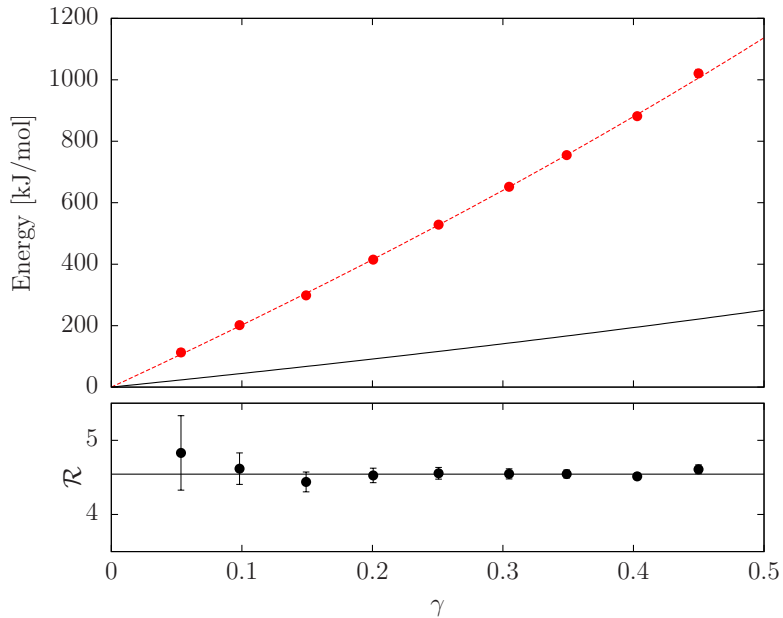


**Figure 2.20:** Comparison of the energy ( $E_{\text{sim}}$ ) of the MARTINI model buckling simulations with the free energy ( $\mathcal{E}(\gamma)$ ) of the buckles. The description of the symbols and methods is the same as in Fig. 2.19. The free energy was calculated using  $\kappa = 29.0 k_{\text{B}}T$ . Bottom: The ratio between the simulation energy and the buckling free energy is shown. The ratio is approximately constant.

Since the bending modulus  $\kappa$  is the free energy per unit area per unit squared curvature, we can separate it into an energetic part  $\kappa_E$  and an entropic part  $T\kappa_S$  where  $\kappa = \kappa_E - T\kappa_S$ , just like the free energy itself. The ratio of the energetic and entropic parts will have the same ratio  $\mathcal{R}$ . The Cooke and MARTINI models have similar values for  $\mathcal{R}$ , with  $\mathcal{R} = 5.43 \pm 0.12$  for Cooke and  $\mathcal{R} = 4.59 \pm 0.08$  for MARTINI. The ratio of the Plum model,  $\mathcal{R} = 9.3 \pm 1.0$ , is almost double the ratios of the other models.

The question now becomes what we can tease out of this ratio, which turns out to be the temperature dependence of the bending modulus. We can relate the entropic bending modulus to the total bending modulus by

$$\kappa_S = -\frac{\partial \kappa}{\partial T} . \quad (2.46)$$

It follows that

$$\frac{\partial \log \kappa}{\partial \log T} = 1 - \mathcal{R} . \quad (2.47)$$

If we make the assumption that  $\mathcal{R}$  does not change with the temperature, then the

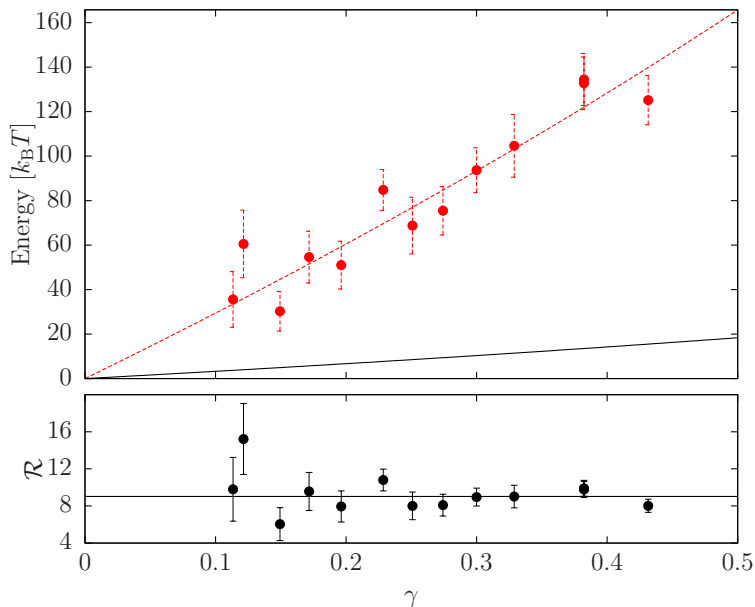


**Figure 2.21:** Comparison of the energy ( $E_{\text{sim}}$ ) of the PLUM model buckling simulations with the free energy ( $\mathcal{E}(\gamma)$ ) of the buckles. The description of the symbols and methods is the same as in Fig. 2.19. The free energy was calculated using  $\kappa = 5.49 k_B T$ . Bottom: The ratio between the simulation energy and the buckling free energy is shown. The ratio is approximately constant.

temperature dependence of the bending modulus is:

$$\kappa(T) = \kappa_0 \left( \frac{T_0}{T} \right)^{\mathcal{R}-1}, \quad (2.48)$$

where  $T_0$  is a specific reference temperature and  $\kappa_0 = \kappa(T_0)$ . Of course, it is not guaranteed that  $\mathcal{R}$  is constant, but as long as it does not strongly change with  $T$ , Eq. (2.48) will provide a good approximation in the region around  $T_0$ . Since  $\mathcal{R} > 1$  for the studied models, the membranes become more flexible as the temperature increases. This is the intuitive reason why entropy should favor bending.

It is not thermodynamically necessary that  $\mathcal{R} > 1$ . In fact for some lipids, membranes soften upon *cooling* when slightly above their main phase transition [119–121], which means that entropy disfavors bending in this case.

In fact, these experiments [119–121] suggest that at 300 K (3 K above the transition temperature into the ripple phase)  $\mathcal{R}$  is negative for DMPC. This result might seem counterintuitive, but it is not forbidden by thermodynamics. These experimental results for DMPC are very different from the simulation results. There is one simple explanation for this that deals with the difference in transition temperatures for real DMPC and MARTINI DMPC. MARTINI DMPC underestimates the main transition temperature of DMPC,  $T_m$ . For real DMPC,  $T_m \approx 297$  K, while for MAR-

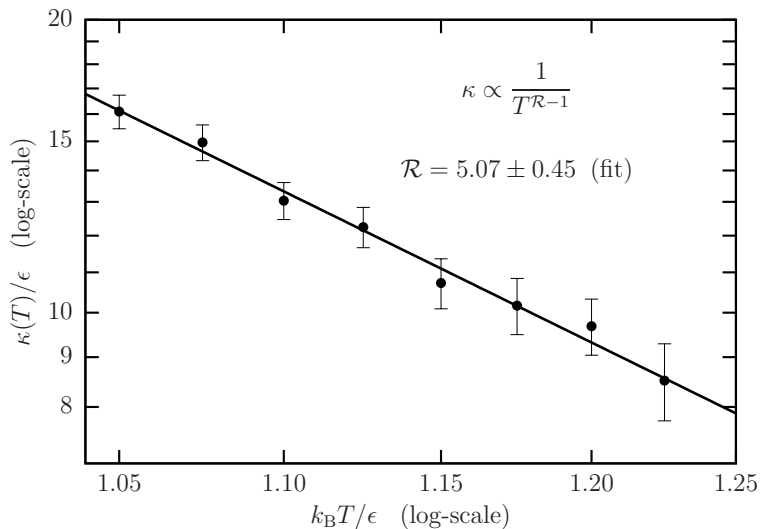


**Figure 2.22:** The temperature dependence of the bending modulus  $\kappa(T)$  for the Cooke model (log-log plot). The measurements were performed by simulating tethers. The line is a fit to Eq. (2.48) with  $\mathcal{R}$  and  $\kappa_0$  as fitting parameters. The  $\mathcal{R}$  value from the slope agrees with the value determined from analysing the energetics of buckles at a single temperature within error bars.

TINI DMPC  $T_m \approx 274$  K [59]. Thus, our MARTINI simulations at 300 K are way above the transition temperature, and behave similar to DOPC when it is not near its  $T_m$ . Experiments on DOPC safely above the main transition temperature (30 – 60 K) suggest that  $\mathcal{R} = 2.8 \pm 0.2$  [122]. The discrepancy between the DMPC simulations and experiment are most likely caused by the difference in the phase transition temperature between the two.

## 2.6 Discussion

We have shown how the buckling method can be used to measure the bending modulus of fluid membranes, using the Cooke, MARTINI, and PLUM models as examples. In addition, by looking at the energetics of the simulation, we can obtain the local temperature dependence of the bending modulus. The method is efficient, requiring the simulation of only a strip of membrane and does not need to sample slow fluctuation modes. Finally recall that actively bending a membrane in a buckle should work better for stiffer membranes, such as membranes in the gel-phase. This will be the topic of the next chapter.

# Chapter 3

## Buckling Gel Membranes

In this chapter, we will examine buckled membranes in the gel phase, with the primary goal of determining the bending modulus. As we argued in Chapter 2, the buckling method should perform even better with stiffer membranes, and gel phases are believed to be significantly stiffer than their fluid counterparts. However, we will see that Helfrich theory fails to properly describe the buckled gel-phase membranes. Specifically, we find that the gel membranes soften upon bending, which leads to curvature localization and negative compressibility—neither of which are predicted by the theory using the Helfrich Hamiltonian. We propose a theoretical framework that expands on Helfrich theory with an energy density that smoothly transitions from a quadratic to a linear curvature dependence, which introduces a new cross-over length scale  $\ell$ . With this new theory, we describe the shape of the buckles, examine the stress-strain relation, and finally extract both the bending modulus and the new length scale  $\ell$  from simulations.

### 3.0.1 Gel phase Membranes

When a fluid lipid bilayer is cooled below the main phase transition temperature, it can enter a number of different phases. One of the main phases is the gel-phase ( $L_{\beta'}$ ), which is primarily characterized by an increased ordering of the tails of the lipids, normally observed by measuring the lipid tail order parameter [23, 24]. The straightening of the tails leads to an increase in the membrane thickness and a reduction of the area per lipid [22, 24]. Most important for this thesis, the rigidity of the membrane greatly increases.

Gel-phase membranes have not been studied to the same extent as fluid phase membranes, because with few exceptions, such as the stratum corneum [123, 124], most *in vivo* lipid membranes are in the fluid phase. However, chemists can now synthesize a large number of lipids with a wide range of main phase transition temperatures, from below the freezing temperature of water to over 75° C [125]. This has increased the interest of bioengineers, hoping to take advantage of the material

properties of these membranes for applications such as drug delivery [8, 126, 127]. Permeation through gel membranes is much slower than that of the fluid phase, with the maximum permeability rate occurring around the phase transition temperature [126]. Thus the general idea is to store the drug inside a vesicle in the gel phase and then heat the part of the body where the drug is to be delivered above the transition temperature, releasing the drug in the targeted area. This means that the lipids that form the vesicle need their transition temperature to be slightly above the temperature of the human body.

Besides such potential bioengineering applications, studying the bending properties of gel-phase membranes might reveal exciting exotic behavior<sup>1</sup>. As we will see, gel membranes have the interesting mechanical property of curvature localization, which under the right conditions leads to negative compressibility. This phenomenon has been studied previously in wide isotropic beams [9], floating elastica [128–131], and elastic metamaterials [9]. Though negative compressibility normally exacerbates the failure modes of a material, this property can be useful for some applications, for instance in mechanical sensors and microactuators [9, 130, 131]. The vast amount of information available concerning the structure and thermodynamics of lipid membranes makes them attractive candidates to study negative compressibility. In addition, the ability to trigger this exotic behavior simply by cooling below the main phase transition temperature, which can be tuned using suitable lipids or mixtures of lipids, makes lipids promising candidates for use in switchable elastic nano-devices.

### 3.0.2 Motivation for using buckling method for gel-phase membranes

We know that lipid membranes in the gel-phase are much stiffer than their fluid counterparts [132], making traditional fluctuation methods impractical as we discussed in Chapter 2. Recall that fluctuation methods measure the amplitude of the fluctuating modes (undulation [60, 81–84, 86, 88, 92, 93] or orientation fluctuations [19, 89, 91, 133]) which are inversely related to the bending modulus, and thus the signal is very small for gel membranes. The other active buckling methods discussed in Chapter 2 will still have equilibrium difficulties, making them impractical. Thus, the buckling method appears to be ideal for gel-phase membranes.

## 3.1 Simulation setup

In this section, we first cover the two lipid models that we use in the simulations. Next, we discuss how we create the gel membranes and then the buckles. Finally, we

---

<sup>1</sup>In the interest of full disclosure, this is of course a post-factum rationalization of the historical development. We only found out about the unexpected behavior after we started studying the gel-phase membranes. We entered this project under the belief that it would be a straightforward extension of the fluid phase.

go over some of the main difficulties that were encountered in the simulations as well as how we handled the problems.

### 3.1.1 Lipid models: Cooke

For the model parameters that we use ( $w_c/\sigma = 1.6$ ), the Cooke model undergoes a single phase transition from the fluid phase to the gel phase with transition temperature  $k_B T_m \approx 0.97\epsilon$  [54, 55]. As with all lipids when they enter the gel phase, the area per lipid drops, the diffusion constant decreases by two orders of magnitude and the orientational order parameter abruptly increases [54, 55].

The Cooke gel membranes do not have spontaneous average tilt, and thus we will not be able to tell if tilt has an effect on the buckling of gel membranes. The qualitative results of the Cooke model should have more significance for lipids that do not display tilt, such as PE lipids [134]. Finally, though the Cooke model exhibits many of the characteristics of a gel-phase, we remind the reader that it is a highly coarse-grained model which was developed with the fluid phase in mind. We expect it to behave qualitatively like a gel-phase membrane, but we caution against reading too much into the quantitative values.

### 3.1.2 Lipid models: MARTINI

Just as with the fluid membranes, we will use the MARTINI model of DMPC [57]<sup>2</sup>. Rodgers *et al.* have looked at the phase behavior for a number of MARTINI lipid types including DMPC [59].

For MARTINI DMPC, the main phase transition is at 274 K. The area per lipid drops at the phase transition to approximately  $0.46 \text{ nm}^2$ . Also, the order parameter and the height of the membrane both increase discontinuously at the phase transition, and the diffusion constant decreases by two orders of magnitude; all of these results are consistent with a gel phase [59].

As with the Cooke model, the MARTINI DMPC model does not show any systematic tilt. This is different from real DMPC, and again, we should be careful to not read too much into the specifics of MARTINI DMPC. Instead, our focus is on the qualitative results.

### 3.1.3 Simulation parameters

We used the standard tuning for the Cooke model with  $w_c/\sigma = 1.6$ , but with the temperature reduced to  $T = 0.85 \epsilon/k_B$ . The simulations were performed using ESPResSo [112], employing a Langevin thermostat [113], with a time step of  $\delta t = 0.002 \tau$ . The simulation box dimensions were kept fixed for each buckle simulation.

---

<sup>2</sup>The resolution of MARTINI prevents it from distinguishing between DMPC and DLPC.

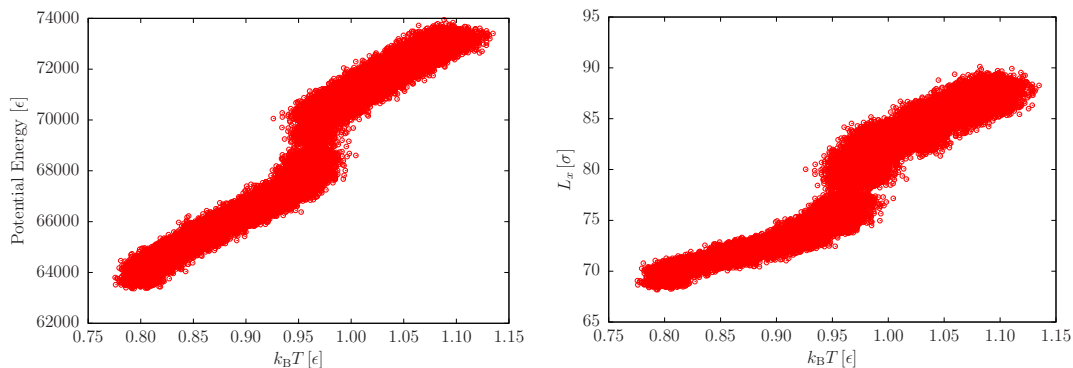


**Figure 3.1:** As we reduce the temperature for the Cooke model, the potential energy (left) and strip length (right) jumps at the main transition temperature.

The MARTINI simulations were performed using GROMACS 4.5 [114], employing a Berendsen thermostat [115] with a time constant  $\tau_T = 1$  ps at a reference temperature of  $T = 265$  K. Ten percent of the solvent consists of “antifreeze” particles; this percentage has been shown to prevent the solvent from freezing, while having little effect on the membrane [57, 59]. The simulation used an integration time step  $\delta t = 30$  fs, which is smaller than what is normally used for fluid membrane simulations, but has previously been shown to be more appropriate for gel simulations [59]; a 1.2 nm cutoff for the neighbor list which is updated every 10 steps; a relative dielectric constant  $\epsilon_r = 15$ , and 1.2 nm cutoffs for Lennard-Jones and Coulomb interactions. The barostat for the  $z$ -direction was set to  $P = 1$  bar and  $\kappa_T = 3 \times 10^{-5}$  Pa.

### 3.1.4 Creating the gel membranes

To create the gel membranes, we slowly cool simulations of flat membrane strips by reducing the temperature by  $0.005 \epsilon/k_B$  for the Cooke model and 1K for the MARTINI model, running the simulation at this temperature for  $2000 \tau$  for Cooke and 18 ns for MARTINI, and then repeat the process. The simulations of flat membranes are done at constant tension, because the area per lipid changes as the temperature changes, and the simulation box needs to change accordingly. Unlike most simulations, where we isotropically couple the pressure along all three simulation axes, we must apply a separate barostat for all directions. This is necessary to help the lipids order themselves when the membrane enters the gel phase.

As we cool the membranes, we observe jumps in the energy and box length at the main phase transition (Fig. 3.1), showing that we did move through the transition to the gel phase.

### 3.1.5 Creating buckles

We create the buckles using the exact transformation method described in Chapter 2. After creating the buckles, we need to perform a standard warm-up where we slowly remove caps on the potentials. For the MARTINI simulations, we first add the anti-freeze and then the water solvent. The position of each anti-freeze particle is randomly chosen, and the particle is kept as long as no other particle is within a cutoff distance which was 0.21 nm. The process is continued until enough anti-freeze particles are added to the simulation. After the anti-freeze is in place, the simulation box is fully solvated and then water particles are removed that are within 0.21 nm of a non-water particle. For the MARTINI simulations, an energy minimization step is performed both before and after the solvent is added.

### 3.1.6 Comment on Simulation Difficulties

There are two main difficulties with the simulation of gel buckles. The first problem, which applies to any simulation of gel membranes, is the long times required to reach equilibrium. To make matters worse, the simulation may enter a state characterized by long stretches where the energy and stress are both constant, only to be terminated by a sudden jump where the energy drops and the stress increases. An example is shown in Fig. 3.2. These jumps also do not necessarily decrease in magnitude as the simulation increases, which prevents us from being able to extrapolate the equilibrium values. For the simulation in Fig. 3.2, it appears that the time between jumps increases with the number of jumps. Other simulations have shown a long time (most of the simulation) before any jumps, so we have not been able to confirm if this increase in time between jumps always holds. We can only run the simulations longer than normal and hope that if we do not see a jump, the simulation is in equilibrium. Thus, we only know for sure that we have a lower bound on the stress for each simulation. The number of jumps appears to depend on how smoothly the buckle is created, with a large number of jumps occurring when the gel buckle is created by either cooling a fluid buckle or by compressing a flat gel buckle. When we create the buckles using the parametric equations of the shape, we see far fewer jumps, most likely because we start with fewer defects.

Second, the buckle deforms to such an extent that it can no longer be described as a continuous membrane at large strains. Fig. 3.3 shows a snapshot of a Cooke membrane at  $\gamma = 0.21$ , where the inner monolayer (the monolayer with the larger curvature) breaks at the points of highest curvature. As our subsequent theoretical analysis will suggest, this might be a property of gel-phase bilayers and not a failure of the simulations. For the membranes that we simulate, this break occurs at strains of  $\gamma > 0.2$ , but we can easily avoid this by only simulating buckles at smaller strains.

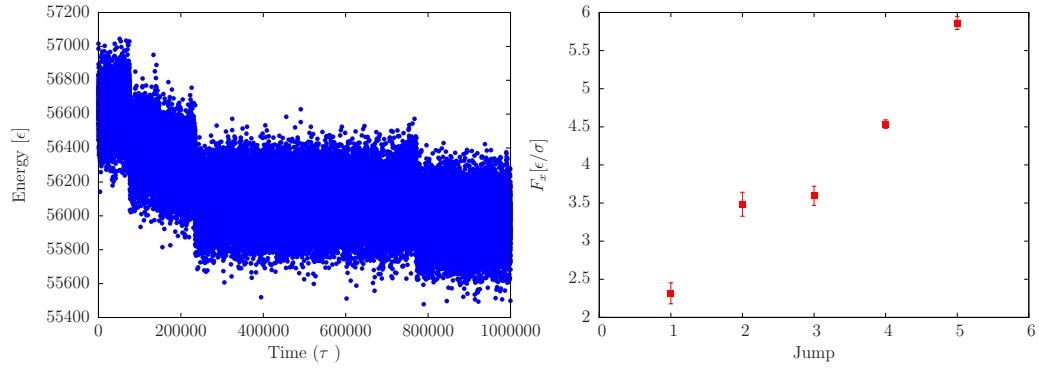


**Figure 3.2:** Left: The potential energy of a Cooke buckle versus time during the start of a simulation. The energy appears to fluctuate around a constant value, as if the system is in equilibrium, before making a sudden sizable jump. This makes it very difficult to determine when the system is in equilibrium. Right: The measured force in  $x$ -direction as a function of the jumps in the energy. Force increases with each jump, often by a large amount.

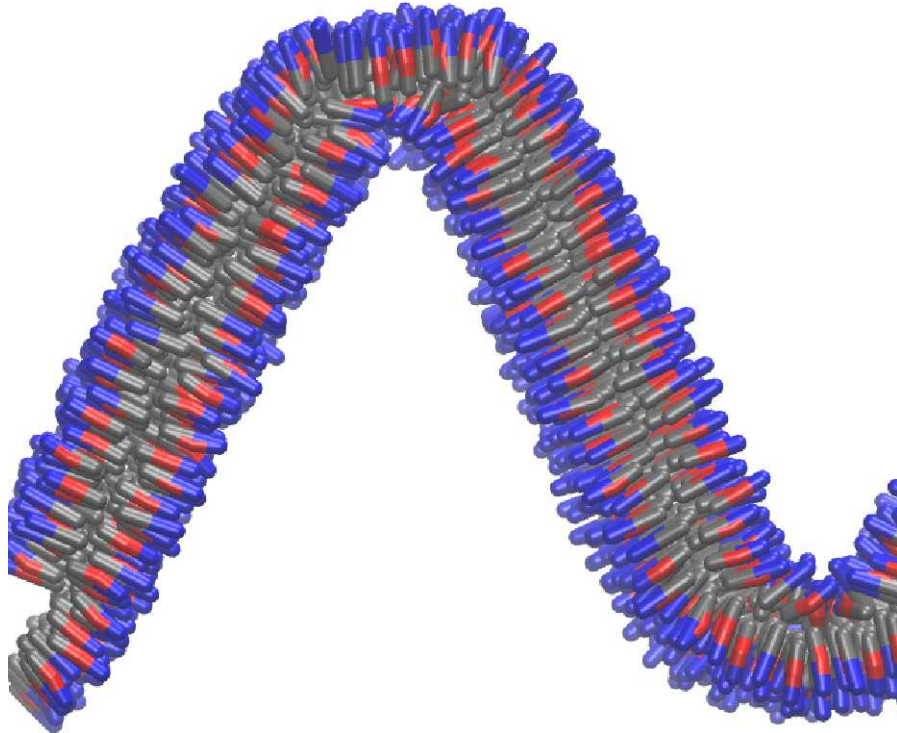


**Figure 3.3:** Snapshot of a Cooke gel buckle at  $\gamma = 0.21$ . The leaflet under the largest curvature has formed a crease and now forms two flat monolayers.

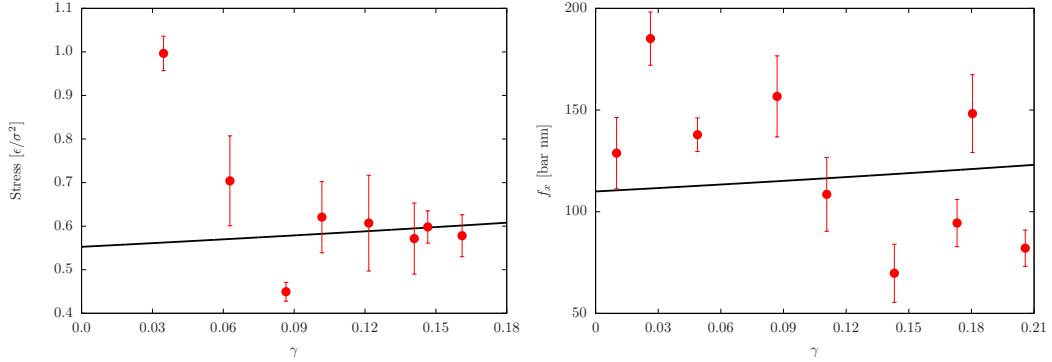


**Figure 3.4:** Left: The stress as a function of strain for the Cooke gel buckle simulations is shown in red. The black line is the best fit using Eq. 2.20 derived from Helfrich theory. Right: The stress for the MARTINI simulations is shown in red. The black line is again the best fit from Helfrich theory. In both cases, the fit is poor: the stress in the simulations decreases with increasing strain, the opposite of what the theory predicts.

## 3.2 Applying Helfrich Theory to Gel Membranes

Once we have the simulations set up properly and run them long enough to feel reasonably confident that they are at equilibrium, we can try to extract the bending modulus, just like we did for the fluid buckles, by fitting the stress-strain relation. This relation is shown in Fig. 3.4, together with the best fit from Helfrich theory. It is clear that the simulation results fail to fit the Helfrich buckling theory, not just quantitatively, but qualitatively. The theory requires the stress to increase with strain, but the stress seems to decrease for both models (though the effect is larger for the Cooke model). This implies that the buckles have a negative compressibility, which is fairly exotic behavior that does not occur for Euler buckles.

If we brazenly attempt to extract the bending modulus from the poor fit, we find that the value of  $\kappa = 48.2 \pm 5.9 k_B T$  for Cooke and  $146 \pm 17 k_B T$  for MARTINI is only 4 (Cooke) to 5 (MARTINI) times greater than in the fluid phase, which is surprisingly small considering that experiments suggest that it should be around an order of magnitude larger [132].

In Fig. 3.5, we compare the energy and the free energy derived from Helfrich theory and calculate the ratio between the two. The ratio ( $\mathcal{R} = 8.9 \pm 1.7$ ) is almost twice the ratio in the fluid phase. If we project the temperature dependence of the bending modulus for both the gel and fluid phase membranes (shown in Fig. 3.6), the gel-phase calculation predicts smaller values for the bending modulus in the fluid phase, including at the phase transition. This would suggest that there would be a small decreasing jump at the phase transition when the membrane is cooled. Though this is possible, it is unlikely and suggests that there is a problem with this analysis.

To understand the origin of this problem, we compare the shape of the gel buckles

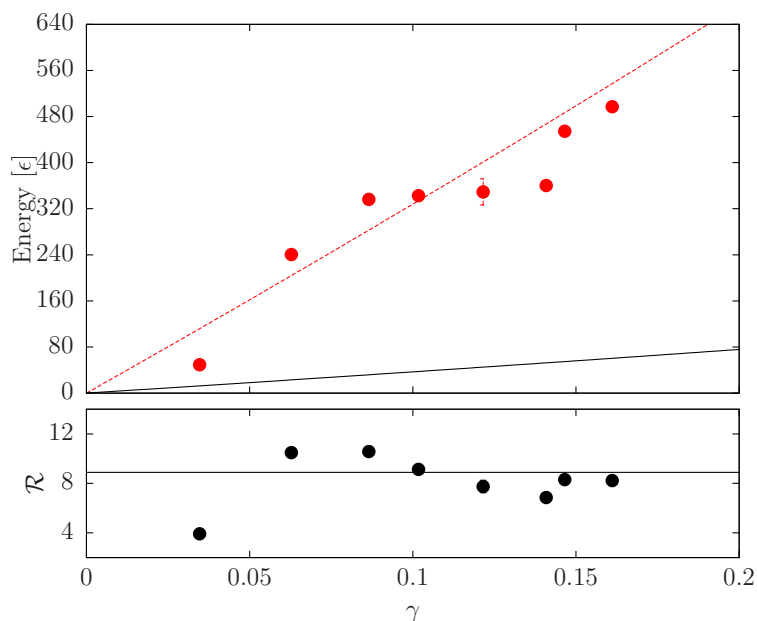


**Figure 3.5:** Top: The energy of Cooke gel buckles versus the dimensionless strain. The red circles are the shifted potential energy of the buckles. The black line is the free energy of the buckles, assuming that Helfrich theory is the correct description for the buckles. The red line is the best fit curve, assuming that the potential energy is a constant ratio of the free energy. Each measurement has error bars, but they are too small to see. Bottom: The ratio of the energy to the free energy for each simulation. The fit for the ratio is poor, which is consistent with the poor fit to the stress-strain relationship.

to the predicted shape from Helfrich theory. We get the shape of the gel buckles using the process described in Chapter 2. Fig. 3.7 and Fig. 3.8 show the range of fluctuations that the membrane undergoes during a simulation for the Cooke and MARTINI models respectively. The fluctuations are much smaller for the membranes in the gel phase than in the fluid phase, as is to be expected.

Fig. 3.9 compares the classical Euler shape with the simulation shape for a Cooke buckle at  $\gamma = 0.08$ . We see the deviation in the shape, though small, is non-random and is much larger than the deviations at this strain in the case of fluid buckles (Fig. 2.13). The curved regions at the turning points are more curved than the Euler prediction, while the flat regions are flatter. This suggests that gel-membranes experience curvature softening at large curvatures. Fig. 3.10 shows the RMSD between the simulation shapes and the Euler buckle for the Cooke membrane. Even at small strains, there is a large deviation that increases with the strain. Fig. 3.11 shows the shape of a MARTINI buckle at  $\gamma = 0.16$  which also shows a similar deviation to the Euler shape. The RMSD for the MARTINI buckles (Fig. 3.12) shows a small relatively constant value for  $\gamma \leq 0.1$  but also becomes much larger as the strain

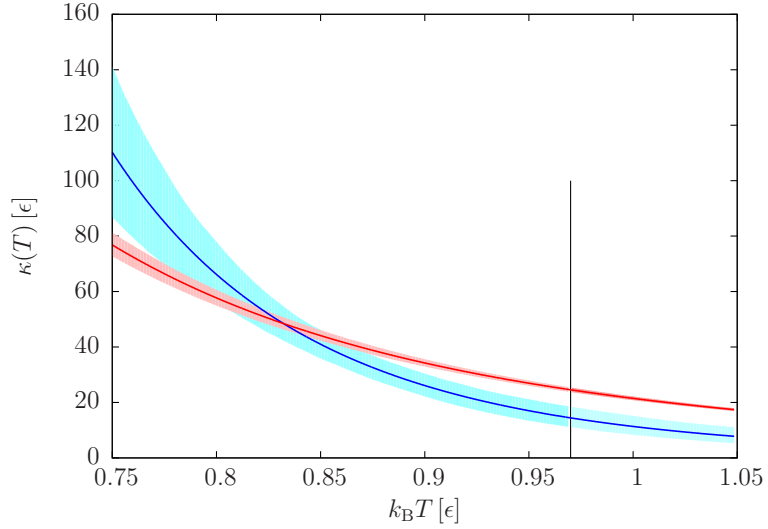


**Figure 3.6:** The temperature dependence of  $\kappa$  using Eq. 2.45 to calculate  $\mathcal{R}$  and Eq. 2.48 for the temperature dependence. The temperature dependence from the fluid measurement is shown in red with with the 0.66 confidence band in red. The temperature dependence from the gel measurement is shown in blue with the 0.66 confidence band in cyan. For both cases, the dependence is extended beyond the phase transition which is shown with the black vertical line. The gel measurement is surprisingly low, and the value of the gel bending modulus is actually lower than the value of the fluid bending modulus at the phase transition.

increases.

### 3.3 Theory

In this section, we discuss how we expand on the Helfrich framework in order to more accurately describe the gel-phase buckles. We start by proposing a new energy functional that accounts for the curvature softening observed in the shape of the gel-phase buckles. We then go into the details of how we solve the Euler-Lagrange equations of this functional, which describe the shape of the buckles. From this, we calculate the value of  $\kappa$  plus the new material parameter  $\ell$  by suitable fitting.

#### 3.3.1 Modifying Helfrich Theory

We need to modify the Helfrich Hamiltonian in order to properly describe gel phase buckles. The curvature localization exhibited by the simulated shapes suggests that the energy penalty for large curvatures is lower than what Helfrich theory would predict. Perhaps the easiest modification to think about is extending Helfrich theory by

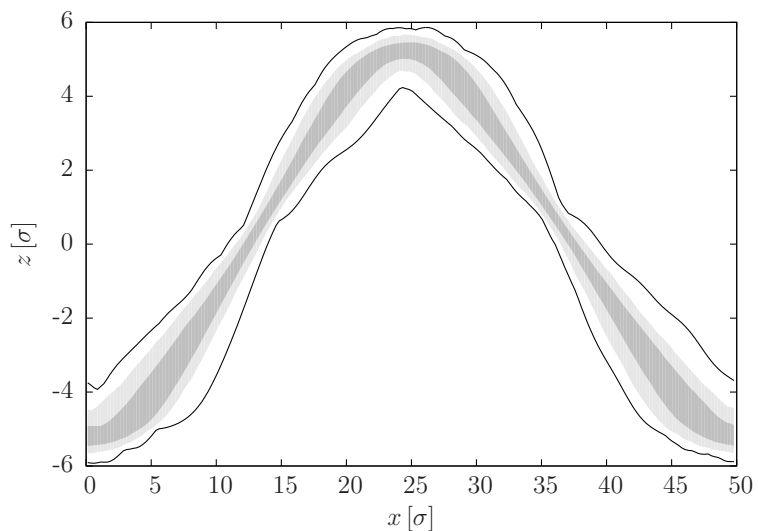


**Figure 3.7:** The graph shows the range in shapes of a Cooke membrane as it fluctuates. For each snapshot, the membrane is first shifted so that its minimum is at  $x = 0 \sigma$  and the shape is centered so that the middle of the membrane is at  $z = 0 \sigma$ . 68 % of the membrane snapshots fall in the dark grey band. 95 % fall in the light grey band. The two black lines are the maximum and minimum position of the membrane over the simulation.

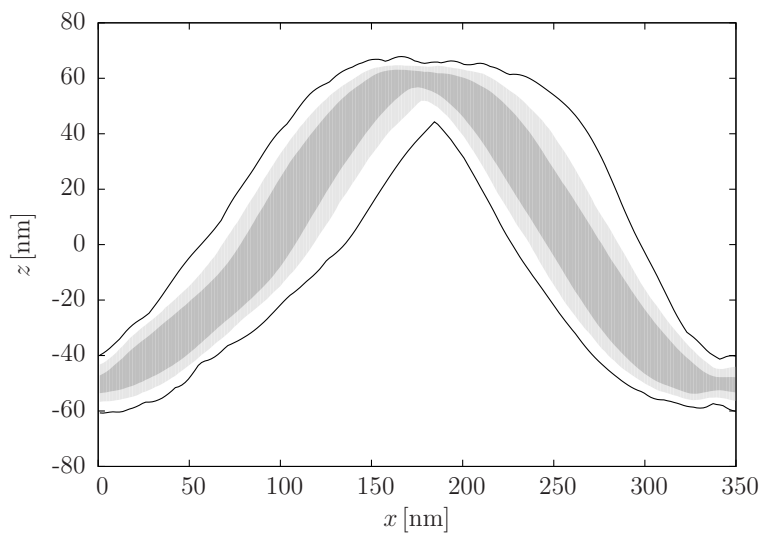


**Figure 3.8:** The graph shows the range in shapes of a MARTINI membrane as it fluctuates. The alignment of the membrane for each snapshot and the shapes are the same as in 3.7.

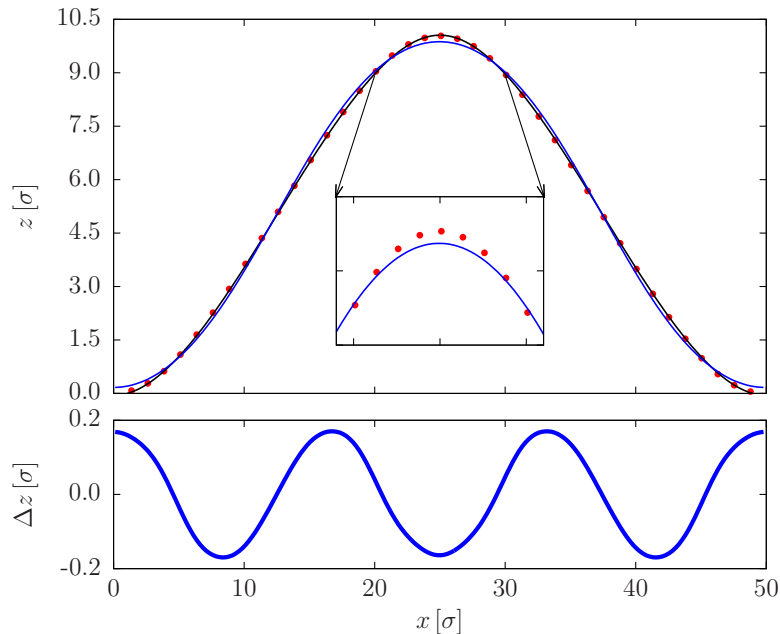


**Figure 3.9:** Top: The shape of the simulation of the Cooke membrane at  $\gamma = 0.08$  is shown with red dots. The blue line is the shape predicted by Helfrich theory. The prediction fails to capture the sharpness in the regions of large curvature and the flatness between these regions. The insert emphasizes the deviation at the maximum of the buckle. Bottom: The difference between the shape of the theoretical prediction and the simulation is shown.

a quartic term that has a negative pre-factor. This would pose a problem, though, because the energy density would not be bounded below, which in turn could potentially lead to problems with the numerical solutions—besides the fact that it is theoretically unsatisfying. We could bound the energy density below by adding a sixth order term in the curvature, but then we would need two new parameters, and we want to make sure that we do not add unphysical structure to the functional.

Our goal is to add higher order terms where the moduli are related by only two parameters, the bending modulus  $\kappa$  and a new length parameter  $\ell$ . In addition, the functional must be bounded below and should ideally be convex. A convenient way to achieve this is by using a functional form that crosses over from a quadratic to a linear dependence of the curvature at a characteristic curvature scale  $\ell^{-1}$ . There are multiple functions that process these qualities, but some are easier to work with than

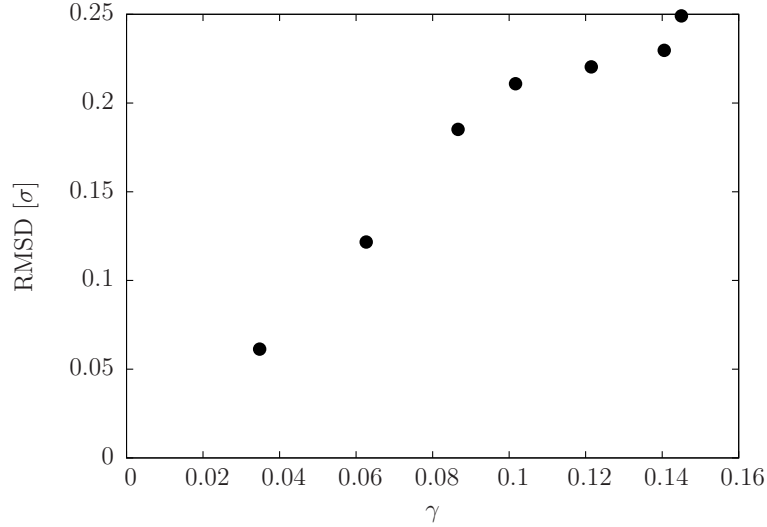


**Figure 3.10:** The RMSD between the simulation shape and the shape predicted by Helfrich theory as a function of strain for the Cooke gel-phase. The RMSD is much larger and increasing more at these low strains than for the buckles in the fluid phase (Fig. 2.16).

others. We chose the following functional [135]:<sup>3</sup>

$$\tilde{e}(K) = \kappa \ell^{-2} \left[ \sqrt{1 + \ell^2 K^2} - 1 \right] \quad (3.1a)$$

$$= \begin{cases} \frac{1}{2} \kappa K^2 - \frac{1}{8} (\kappa \ell^2) K^4 + \mathcal{O}(K^6) & , \quad K \ll \ell^{-1} \\ \kappa \ell^{-1} (|K| - \ell^{-1}) + \mathcal{O}(K^{-1}) & , \quad K \gg \ell^{-1} \end{cases} . \quad (3.1b)$$

At small curvatures, the equation looks like Helfrich theory modified by a negative quartic term. At large curvatures, the energy increases linearly with the curvature.

There are other higher order terms that could matter for gel phase lipids. The first set are terms that depend on the Gaussian curvature,  $K_G$ , mainly  $K^2 K_G$  and  $K_G^2$ . Since we are investigating planar buckles,  $K_G = 0$ , so even if these terms might be relevant to gel membranes, they do not affect buckles and thus we cannot investigate them. However, there is another term,  $(\nabla K)^2$ , which is also of inverse quartic order in length. This term could also lead to curvature softening as long as its modulus is negative. We initially leave out this term only for pragmatic reasons, since we would have to include more moduli and it would make the theory harder to solve. We will see that the simulations agree well with the new theory without a  $(\nabla K)^2$  term. This suggests (but does not prove) that its effect is small.

<sup>3</sup>It turns out that there is a physical interpretation of this functional which we did not know about when we chose it. We will discuss the surprising physics connection later in this chapter. We chose this specific functional primarily because it was the easiest one to work with.

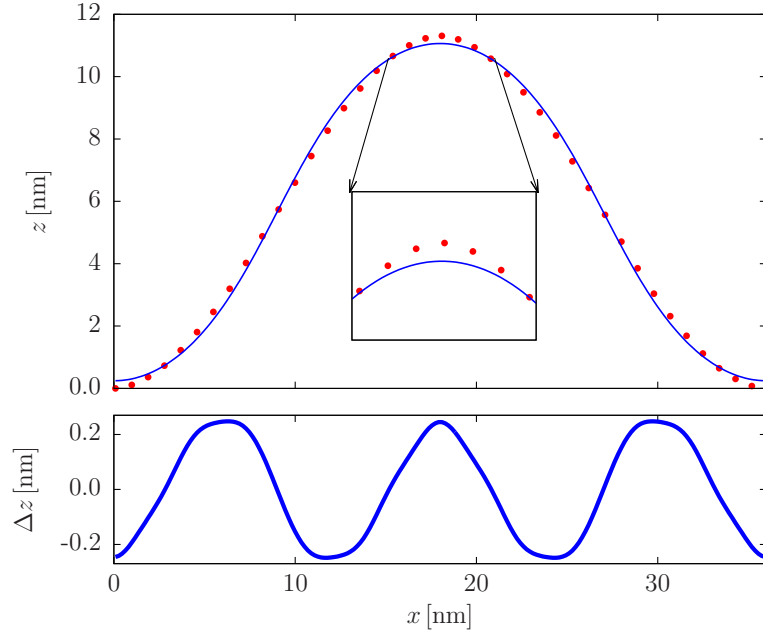


**Figure 3.11:** Top: The shape of the simulation of the MARTINI membrane at  $\gamma = 0.16$  is shown with red dots. The blue line is the shape predicted by Helfrich theory. The prediction fails to capture the sharpness in the regions of large curvature and the flatness between these regions. The insert emphasizes the deviation at the maximum of the buckle. Bottom: The difference between the shape of the theoretical prediction and the simulation is shown.

### 3.3.2 Predicting the shape and stress in the new theory

We now need to solve the Euler-Lagrange equation for the new energy functional, similar to what we did for the Helfrich theory. We again will describe the shape through the angle  $\psi(s)$  of the profile's tangent vector with respect to the horizontal as a function of arc length  $s$  with  $K = -d\psi/ds = -\dot{\psi}$ . The energy of the buckle is

$$\mathcal{E} = \kappa L_y \int_0^L ds \left\{ \frac{1}{\ell^2} \left[ \sqrt{1 + \ell^2 \dot{\psi}^2} - 1 \right] + \frac{1}{\lambda^2} \left[ \cos \psi - \frac{L_x}{L} \right] \right\} . \quad (3.2)$$

We again vary  $\mathcal{E}[\psi(s)]$  with respect to  $\psi$  to find:

$$\delta \mathcal{E} = \kappa L_y \int ds \left\{ \frac{\dot{\psi}}{\sqrt{1 + \ell^2 \dot{\psi}^2}} \delta \dot{\psi} - \lambda^{-2} \sin \psi \delta \psi \right\} . \quad (3.3)$$

After integrating by parts, this leads to the Euler-Lagrange equation:

$$-\lambda^{-2} \sin \psi = \frac{d}{ds} \frac{\dot{\psi}}{\sqrt{1 + \ell^2 \dot{\psi}^2}} . \quad (3.4)$$

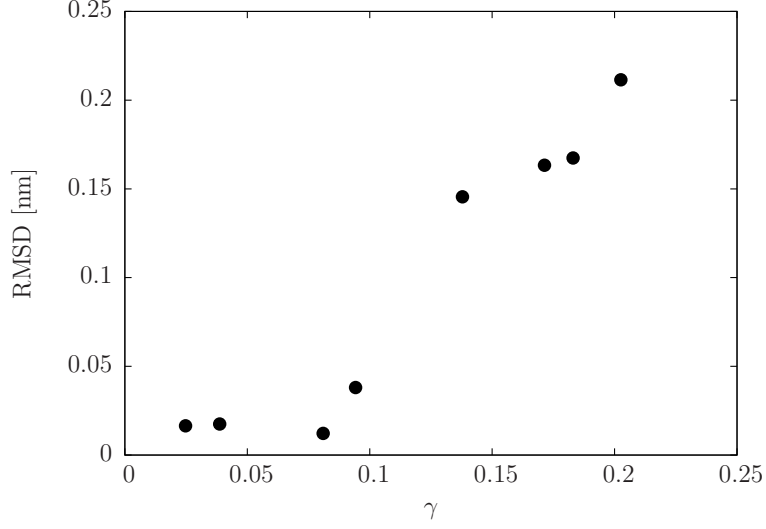


**Figure 3.12:** The RMSD between the simulation shape and the shape predicted by Helfrich theory as a function of strain for the MARTINI DMPC gel-phase. Unlike in the case of the Cooke model, Helfrich theory appears to do a good job at small strains ( $\gamma \leq 0.1$ ), but the two shapes diverge rapidly at higher strains.

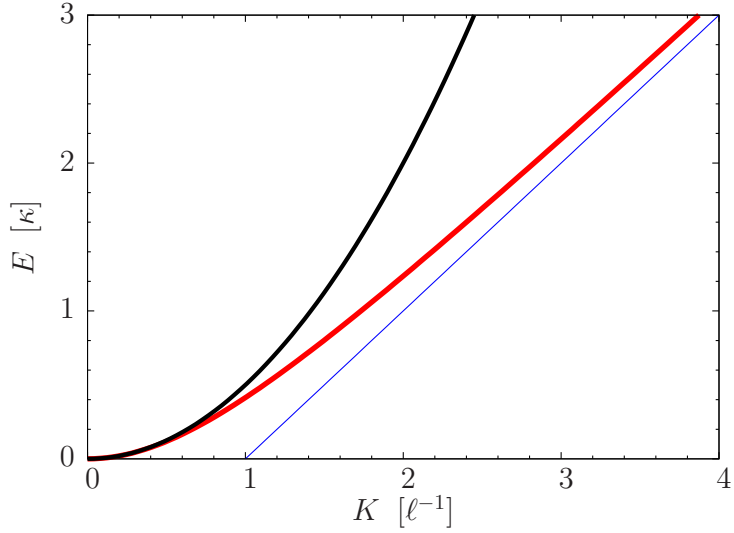


**Figure 3.13:** Graph of curvature energy functions. The black line is the total curvature contribution of the Helfrich Hamiltonian ( $E/\kappa = \frac{1}{2}K^2$ ). The red line is the energy function of the modified theory. At small curvatures, the energy looks quadratic, but becomes linear at large curvatures. The small blue line shows the asymptotic behavior of the linear theory. The crossover from the quadratic to linear nature is centered at  $K = \ell^{-1}$ .

We still have the same boundary conditions as before, and we measure the arc length from the inflection point,  $\psi(s=0) = \psi_i$  and  $\dot{\psi}(s=0) = 0$ .

Eq. (3.4) can be integrated using the integrating factor  $\dot{\psi}$ .

$$\frac{\ell^2}{\lambda^2}(\cos \psi(s) - \cos \psi_i) = 1 - \frac{1}{\sqrt{1 + \ell^2 \dot{\psi}^2}}. \quad (3.5)$$

We now will define  $\tilde{f}_x = \ell^2/\lambda^2 = \ell^2 f_x/\kappa$  and perform some algebra to get a more useful form of Eq. (3.5):

$$\ell \dot{\psi} = \sqrt{\left[1 - \tilde{f}_x(\cos \psi - \cos \psi_i)\right]^{-2} - 1}. \quad (3.6)$$

Separating variables, we obtain the quadrature

$$s = \ell \int_{\psi_i}^{\psi(s)} d\psi \frac{1}{\sqrt{\left[1 - \tilde{f}_x(\cos \psi - \cos \psi_i)\right]^{-2} - 1}}. \quad (3.7)$$

This equation has three parameters: the inflection angle  $\psi_i$ , the scaled stress  $\tilde{f}_x$ , and the crossover length  $\ell$ . We still have two boundary conditions: the periodicity and confinement on the membrane,  $\psi(L/4) = 0$  and  $x(L/4) = L_x/4$ , respectively, which can be used to find the first two parameters. In order to find the value of  $\ell$ , we need to fit the theory to the measured shape. This is fundamentally different from the Helfrich buckles, where the shape of the buckle does not depend on the material parameters of the membrane.

For small  $\ell$  and small  $\tilde{f}_x$  (note that small  $\tilde{f}_x$  follows directly from small  $\ell$ ) we can expand the right side of Eq. 3.7, which leads to:

$$s = \int_{\psi_i}^{\psi(s)} \frac{\lambda}{\ell} \frac{d\psi}{\sqrt{2(\cos \psi - \cos \psi_i)}} + \mathcal{O}(\ell), \quad (3.8)$$

which is just the quadrature of the Euler buckle.

We can also express the shape of the buckle as quadratures. Using the fact that  $ds = d\psi/\dot{\psi}$ , we find that  $dx = \dot{x} ds = \cos \psi d(\psi/\dot{\psi})$ , and  $dy = \dot{y} ds = \sin \psi d(\psi/\dot{\psi})$ .

$$x = \ell \int_{\psi_i}^{\psi(s)} d\psi \frac{\cos \psi}{\sqrt{\left[1 - \tilde{f}_x(\cos \psi - \cos \psi_i)\right]^{-2} - 1}}, \quad (3.9)$$

$$y = \ell \int_{\psi_i}^{\psi(s)} d\psi \frac{\sin \psi}{\sqrt{\left[1 - \tilde{f}_x(\cos \psi - \cos \psi_i)\right]^{-2} - 1}}. \quad (3.10)$$

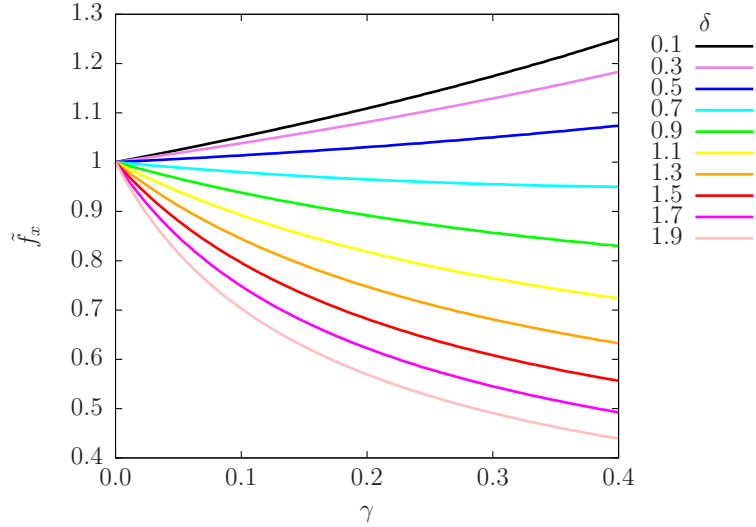


**Figure 3.14:** Graph of  $\tilde{f}_x$  as a function of  $\gamma$  for different values of  $\delta$ . The values of  $\delta$  for each colored line are shown in the key. The three lines with the smallest values of  $\delta$  have positive compressibility, while the remaining seven exhibit negative compressibility. The critical value of  $\delta$  where negative compressibility starts is at  $\delta = 1/\sqrt{3} \approx 0.58$ .

With these equations, we can fit the shape of buckled membranes to the simulations to obtain values for  $\ell$  and  $\tilde{f}_x$ . Once we know these parameters and the stress  $f_x$  measured from the simulations, we can obtain  $\kappa$ .

We would like to express everything in terms of the dimensionless strain  $\gamma = 1 - L_x/L$ , just as with the Helfrich theory. Using the same expansion and matching coefficients technique that was used for the fluid buckle equations, we can express the stress in terms of  $\gamma$  and the additional dimensionless parameter  $\delta = 2\pi\ell/L$ :

$$f_x(\gamma, \delta) = \kappa \left( \frac{2\pi}{L} \right)^2 \left[ 1 + \frac{1}{2} (1 - 3\delta^2) \gamma + \frac{9}{32} \left( 1 - \frac{14}{3}\delta^2 + \frac{31}{3}\delta^4 \right) \gamma^2 + \dots \right] \quad (3.11)$$

For  $\delta > \delta_c = 1/\sqrt{3}$ , the slope of the stress-strain relation becomes negative, meaning that the membrane will have a negative compressibility. Unfortunately, Eq. (3.11) no longer converges in this regime and we must rely on numerically fitting the shape. Fig. 3.14 shows how  $\tilde{f}_x$  changes for different values of  $\delta$ .

## 3.4 Results

We now want to apply the new theory to the simulations of gel membranes. In the first subsection, we describe how we perform the fit. Next, we examine how well the

new theory predicts the shape, before looking at the new stress-strain relation and measuring the bending modulus. Finally, we explore the energetics of the buckles.

### 3.4.1 Fitting the Simulations to the New Theory

As we mentioned above, the series expansion does not converge when  $\delta > 1/\sqrt{3}$ , which happens to be the regime of our gel buckles. Therefore, we have to turn to numerics. We find the value of  $\tilde{f}_x$  and  $\delta$  by minimizing the squared difference between the simulation shape and the numerically determined theoretical shape for specific  $\tilde{f}_x$  and  $\delta$ .

These fits are computationally expensive, which makes attempts to sample the simulation shape many times in order to perform an error analysis impractical. To create a rough error estimate for  $\delta$  and  $\tilde{f}_x$ , we partition each simulation into equal time blocks. For each block, we calculated the average shape, and then fit the shape to get the values from the theory for each block. At this point, we have four parameters for each block,  $\delta$ ,  $\tilde{f}_x$ ,  $L$ , and  $f_x$ . We calculate the value of  $L$  from the simulated shape from each block. In order to obtain an error estimate for  $\ell$  and  $\kappa$ , we use a bootstrapping method where we resample from a multi-variable Gaussian distribution where we assume that the four parameters are correlated.

### 3.4.2 Shape

Now that we have applied the new theory to the simulations, we first want to confirm that it can describe the shape of the simulated buckles. Fig. 3.15 and Fig. 3.16 show the average shape for a Cooke buckle and a MARTINI buckle respectively. The shape from the new theory does a much better job of describing the shape from the simulation than the Helfrich theory. This is also true for the MARTINI model when  $\gamma > 0.1$ .

Fig. 3.17 shows the RMSD between the theoretical shapes and the simulation for the Cooke model. The new theory consistently describes the shape better regardless of the strain value. Fig. 3.20 shows the RMSD for the MARTINI model. At  $\gamma < 0.08$  the shape is described equally well by both Helfrich theory and the new theory. As the strain increases, the new theory is still able to properly describe the shape of the buckles.

The best fit value of  $\ell$  for the Cooke model is  $\ell = 24.8 \pm 1.1 \sigma$  while for the MARTINI model is  $\ell = 13.4 \pm 0.6 \text{ nm}$  (Table 3.1). Fig. 3.18 shows the measured values of  $\ell$  for the Cooke simulations, and Fig. 3.21 shows the same for the MARTINI simulations. The Cooke model shows a small decrease in the value of  $\ell$  with respect to the strain, whereas  $\ell$  appears constant for MARTINI. For the Cooke model, the measurements at small strains have larger errors, and the change in  $\ell$  with strain may reflect on problems measuring the shape.

Using the best fit value of  $\ell$  for each model, we can look at how the RMSD between

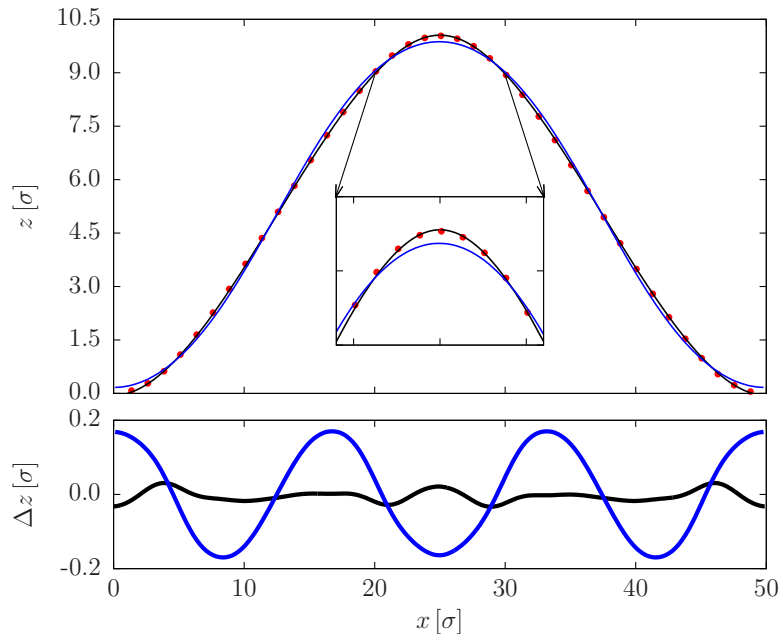


**Figure 3.15:** Comparison between the average simulated and theoretical gel buckle shapes for the Cooke model. Top: The average shape of the Cooke model buckle at  $\gamma = 7.7\%$  is shown in red circles. The blue line is the predicted Euler buckle shape. As we have seen before, the Euler shape does not match the simulation. The black line is the best fit from the new extended theory, using  $\ell$  as the fitting parameter. The vertical axis is stretched approximately fivefold for better visibility. Bottom: The residuals between the simulation and the two theories is shown using the same coloring as the top. The RMSD for the Euler buckle is  $0.122\sigma$ , whereas the RMSD for the extended theory is only  $0.015\sigma$ , nearly an order of magnitude smaller.

the Euler shape and the shape predicted by the new theory depends on the strain. Fig. 3.19 shows the RMSD for the Cooke model, and Fig. 3.22 shows the same for the MARTINI model. In both cases, the RMSD increases with the strain, with the increase being greater for the Cooke model because it has a larger  $\ell$ .

### 3.4.3 Stress-strain Relation

Now that we know that the theory correctly describes the shape, we turn to the stress-strain relation and extract the bending modulus. From the shape fit, we find  $\ell$  and the dimensionless strain variable  $\tilde{f}_x$ , which we can combine with the stress to get  $\kappa$ . The bottom panels in Figs. 3.23 and 3.24 show the values of  $\kappa$  for the Cooke and MARTINI simulations respectively, and we can see that within error bars,  $\kappa$  is independent of strain. The top graphs show the stress-strain relation expected for a gel membrane with the average  $\ell$  and  $\kappa$  from the simulations. In addition, if we take the average value of  $\kappa$  from each simulation, we can get two measures for the stress:

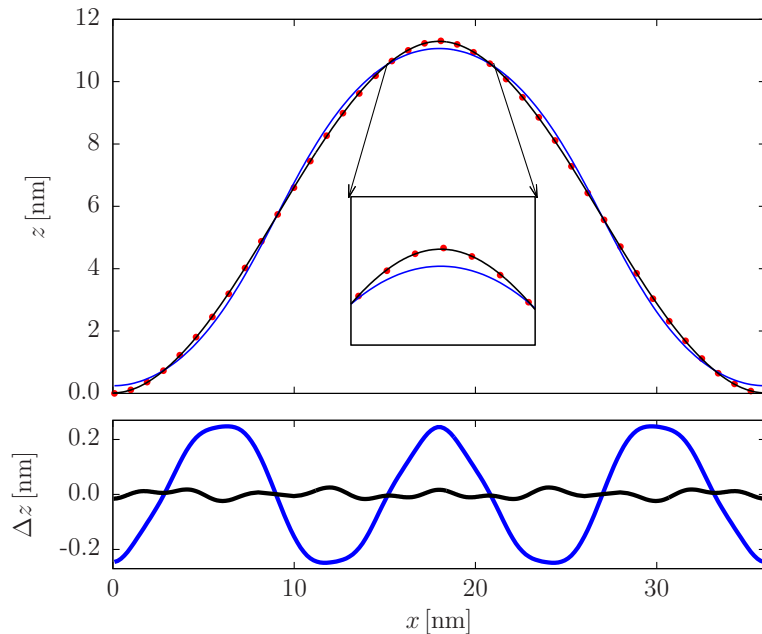


**Figure 3.16:** Comparison between the average simulated and theoretical gel buckle shapes for the MARTINI model. Top: The average shape of a buckle at  $\gamma = 0.17$  is shown in red circles. The blue line is the predicted Euler buckle shape, and the black line is the best fit from the new theory, using  $\ell$  as the fitting parameter. The vertical axis is stretched by approximately a factor of three for better visibility. Bottom: The residuals between the simulation and the two theories is shown using the same coloring as the top. The RMSD for the Euler buckle is 0.167 nm, whereas the RMSD for the extended theory is 0.011 nm, over an order of magnitude smaller.

directly from the stress tensor, and by scaling the scaled stress  $\tilde{f}_x$  that is calculated from the shape. Both measurements of the stress agree with the theory and show a negative compressibility.

### 3.4.4 Values

Table 3.1 gives the material parameters derived from fitting the simulation data for the Cooke and MARTINI DMPC models. The first thing to notice is that for both models  $\kappa/k_B T$  is almost an order of magnitude larger than for the fluid membrane, in line with common expectations [132, 136, 137]. This shows that the seemingly small deviation in shape of the membrane from the Euler buckle prediction has a large effect on the inferred moduli. The second major observation is the size of  $\ell$ ; in both cases, it is substantially larger than the lipid size or even the membrane thickness, again confirming that the membranes cannot be described with just Helfrich theory.

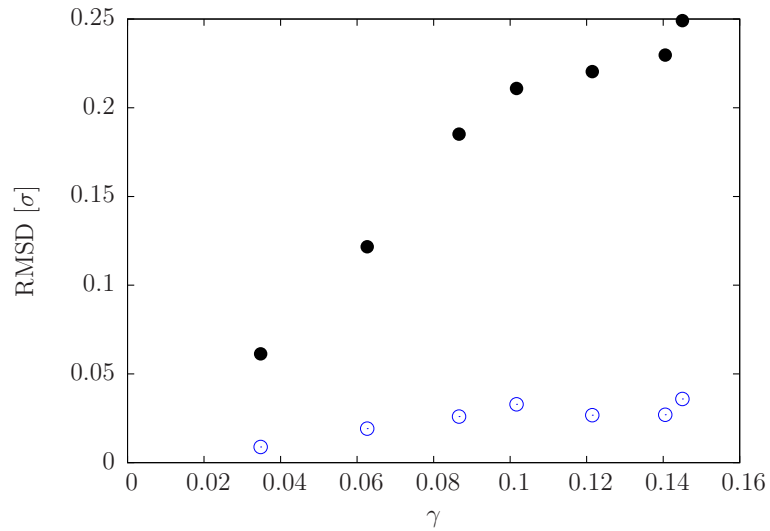


**Figure 3.17:** The RMSD between the simulation shape and the shape predicted by Helfrich theory (black solid circles) and the new theory (blue open circles) as a function of strain for the Cooke model. The new theory does a better job predicting the shape of the simulations at all strains and the RMSD stays relatively constant as the strain increase.

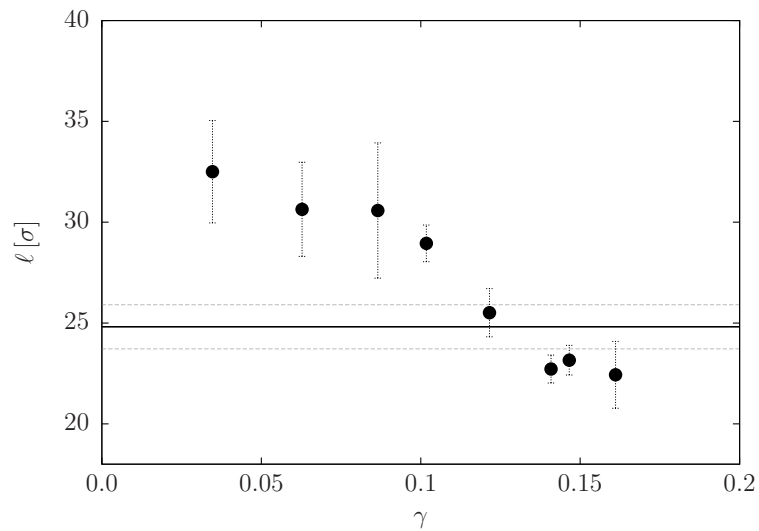


**Figure 3.18:** The value of  $l$  as a function of  $\gamma$  for the Cooke gel-phase simulations. The value of  $l$  decreases slightly with  $\gamma$ . However, the error in the measurement at small strains is larger, which stems in part from the increased difficulty of differentiating between the shapes with different values of  $l$  at small strain.

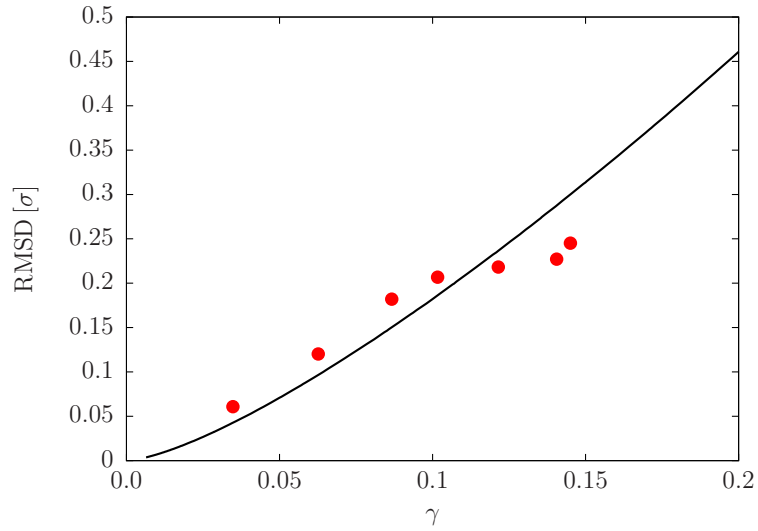


**Figure 3.19:** The RMSD between the shape predicted by the Helfrich theory and the shape predicted by the new theory as a function of strain. For the shapes from the new theory, we use the average value of  $\ell$  from the Cooke simulations,  $\ell = 24.8\sigma$ . The red circles use the value of  $\ell$  from each simulation.

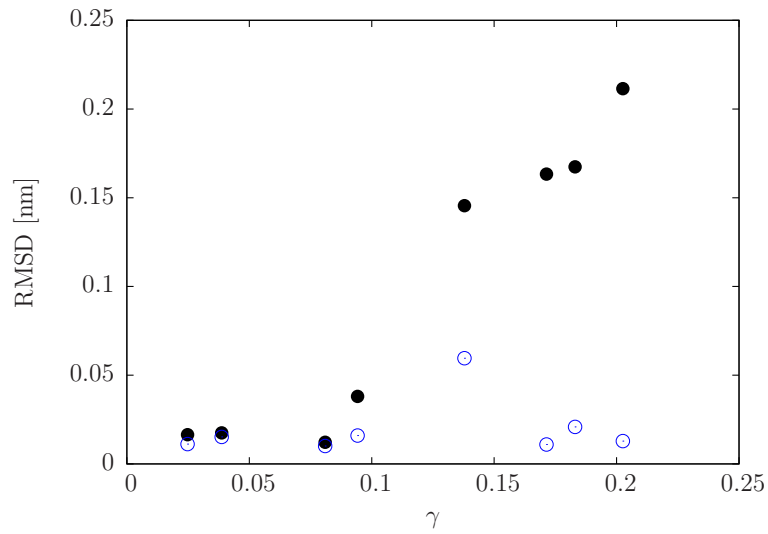


**Figure 3.20:** The RMSD between the simulation shape and the shape predicted by Helfrich theory (black solid circles) and the new theory (blue open circles) as a function of strain for the MARTINI model. At small strains ( $\gamma < 0.08$ ), the new theory and Helfrich perform similarly, but where as the Helfrich theory fails at larger strains, the new theory does well at larger strains.

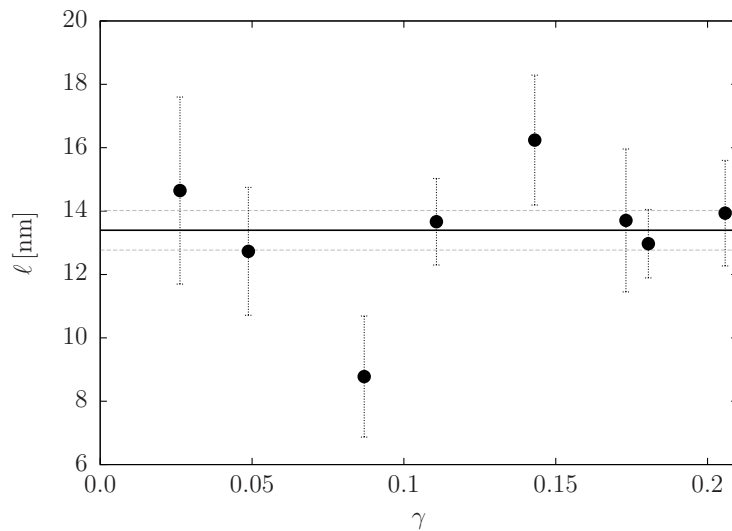


**Figure 3.21:** The value of  $\ell$  as a function of  $\gamma$  for the MARTINI gel-phase simulations. The data supports that  $\ell$  is independent of  $\gamma$  for the MARTINI model.

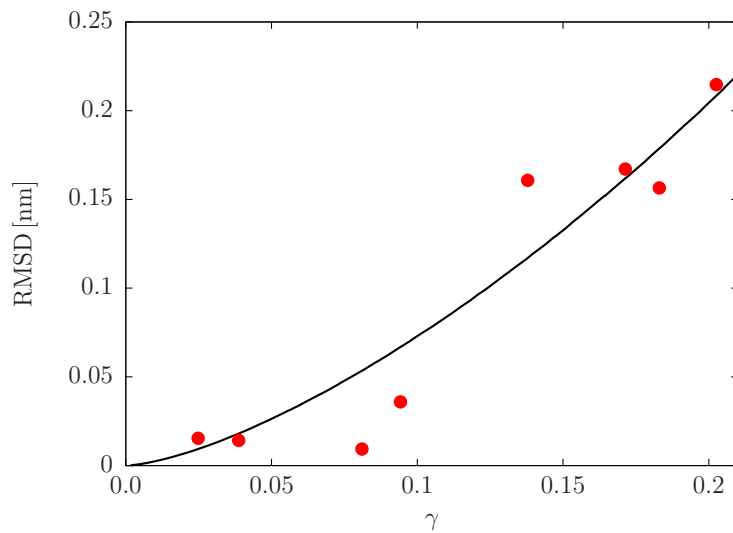


**Figure 3.22:** The RMSD between the shape predicted by the Helfrich theory and the new theory as a function of strain. For the shapes from the new theory, we use the average value of  $\ell$  from the MARTINI simulations  $\ell = 13.4$  nm. The red circles use the value of  $\ell$  from each simulation.

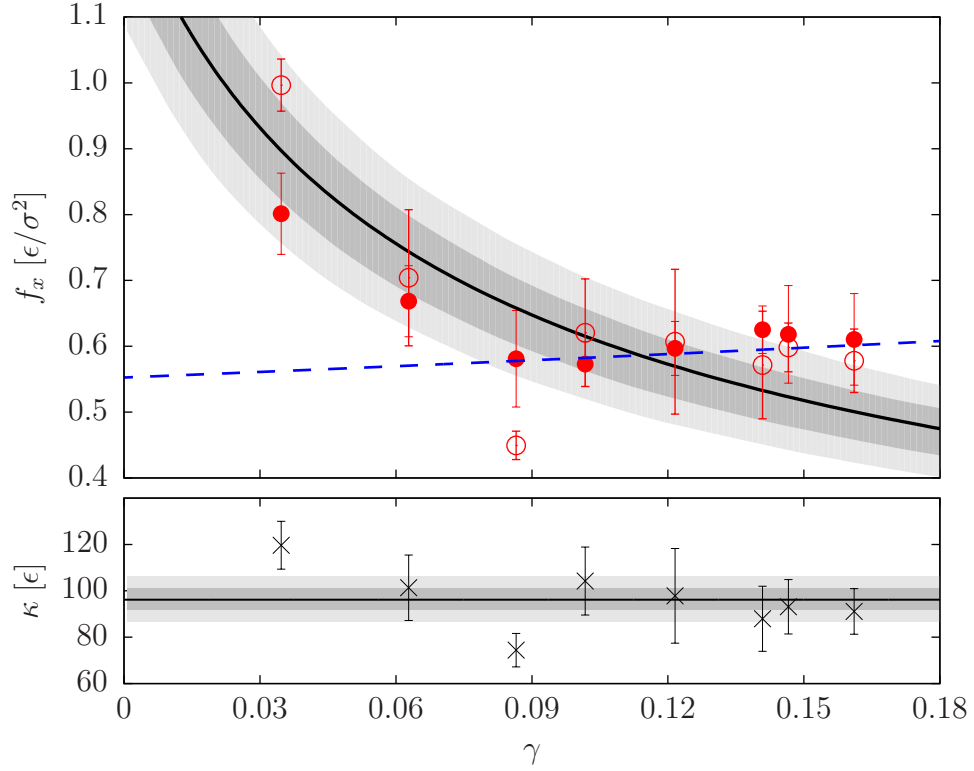


**Figure 3.23:** Top: The buckling stress  $f_x$  as a function of strain  $\gamma$  is plotted for the Cooke model. The open circles are calculated directly from the stress tensor. The filled circles are calculated by scaling  $\tilde{f}_x$  by  $\kappa/\ell^2$ , where  $\tilde{f}_x$  and  $\ell$  are calculated from the shapes of each simulation and  $\kappa$  is taken from the measured stresses by averaging over all simulations. The solid curve is the extended theory's prediction for  $f_x(\gamma)$  using the average value of  $\tilde{f}_x$  and  $\ell$ . The 68% (dark gray) and 95% (light gray) confidence bands are based on resampling from the individual simulation results. The dashed blue line is an attempted fit to the Helfrich theory. Bottom: The bending rigidity  $\kappa$  derived from each simulation for the Cooke model. The black line is the average value of  $\kappa$  from all simulations. The dark gray and light gray areas are the 68% and 95% confidence bands.

Model	$\kappa_{\text{fl}} [k_{\text{B}}T_{\text{fl}}]$	$\kappa_{\text{gel}} [k_{\text{B}}T_{\text{gel}}]$	$\ell$ (nm)	$w$ (nm)	$\ell/w$
Cooke	$12.8 \pm 4$	$96 \pm 5$	$27.5 \pm 2.2$	5.3	$5.2 \pm 0.4$
MARTINI	$29 \pm 1$	$230 \pm 10$	$13.9 \pm 0.5$	3.9	$3.6 \pm 0.1$

**Table 3.1:** The values for the fluid membranes are obtained using the buckling method (Chapter 2). The temperature differs between the fluid and gel phase: for the Cooke Model,  $T_{\text{fl}} = 1.1\epsilon/k_{\text{B}}$  and  $T_{\text{gel}} = 0.85\epsilon/k_{\text{B}}$ ; for the MARTINI Model,  $T_{\text{fl}} = 300$  K and  $T_{\text{gel}} = 265$  K. The length  $\ell$  is the new parameter of our theory. The bilayer width  $w$  is measured as the distance between head beads in the opposing planes for Cooke and between the phosphate beads in MARTINI.

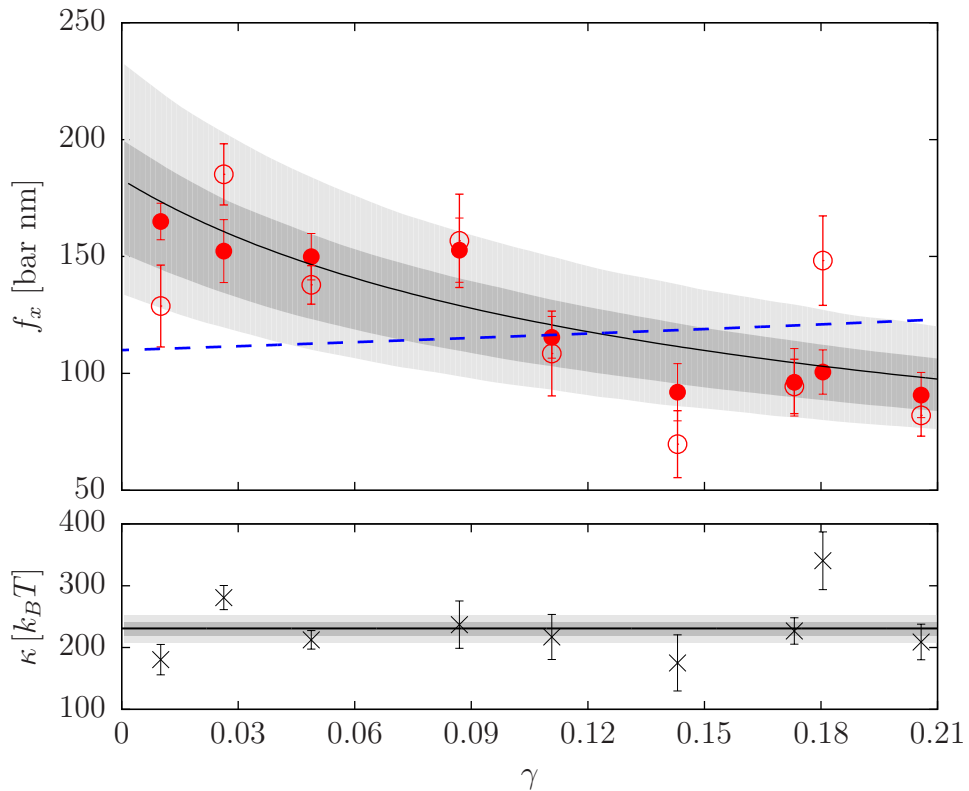


**Figure 3.24:** The buckling stress  $f_x$  as a function of strain  $\gamma$  is plotted for the MARTINI model. The symbols have the same meaning as in Fig. 3.23.

### 3.4.5 Energetics

For the fluid buckles, we were able to extract the temperature dependence of the bending modulus by analyzing the energetics of the buckles. We now explore if the same thing is possible for gel membranes, focusing first on the Cooke membranes and then turning to the MARTINI model. Fig. 3.25 shows the energy and free energy of the Cooke model as a function of strain. The free energy was calculated by numerical integration of the stress-strain relation using the average  $\delta$  from the simulations. Just as with the fluid membranes, the (shifted) energy is equal to the free energy times a constant,  $\mathcal{R} = 7.15 \pm 0.09$ , which is smaller than the ratio obtained using Helfrich theory ( $\mathcal{R}_{\text{Helf}} = 8.9 \pm 1.7$ ). It is still larger than the ratio for the fluid phase ( $\mathcal{R} = 5.43 \pm 0.12$ ). In all cases, the fits are worse than for the fluid simulations. This is most likely caused in part by some simulations still containing defects, though part of the reason is that the error of the mean for these gel simulations is consistently smaller than for fluid simulations because the membranes have much smaller fluctuations than in the fluid phase.

Since the ratio is constant with respect to strain, we again can use Eq. (2.48) to

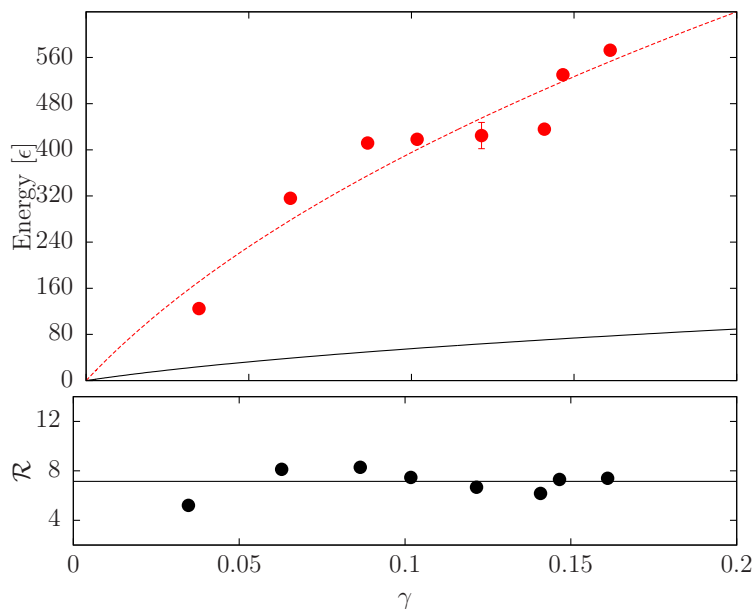


**Figure 3.25:** Top: The energy of the buckles versus the dimensionless strain. The red circles are the shifted potential energy of the buckles. Each point has error bars, but they are too small for most of the data points. The black line is the free energy of the buckles calculated from integrating the stress-strain relation derived from the new theory. The red line is the best fit curve assuming that the potential energy is a constant ratio of the free energy with  $\mathcal{R} = 7.15$ . Bottom: The ratio of the energy to the free energy for each simulation. Though the fit is not the best, it is better than the fit using Helfrich theory (Fig. 3.5).

find the temperature dependence of  $\kappa$ . Since the ratio is larger for the gel membrane,  $\kappa$  changes with respect to temperature more for gel membranes. Fig. 3.26 shows the temperature dependence of  $\kappa$  for the Cooke model under the assumption that the ratio is constant with respect to temperature except at the phase transition temperature. At the phase transition, the jump in  $\kappa$  is  $13.8\epsilon = 13.4k_B T$ . Thus, the new theory predicts that the bending modulus will jump as the membrane goes from the fluid to the gel phase, as opposed to the decrease as an analysis using Helfrich theory predicted. For simulations at  $k_B T = 0.9\epsilon$ ,  $\kappa = 68.7 \pm 5.8\epsilon$ , and for  $k_B T = 0.95\epsilon$ ,  $\kappa = 47.0 \pm 3.9\epsilon$ . In both cases, the measured value is slightly larger than the value predicted from the energetics at  $k_B T = 0.85$ . The large temperature dependence in the gel phase means that the jump at the phase transition is only a factor of two instead of one order of magnitude.

For the Cooke model in the fluid phase, the predicted bending modulus using  $\mathcal{R}$  was accurate over a large temperature range because  $\mathcal{R}$  barely changed with temperature. To check if this is the same for the gel phase, we calculate the ratio at  $k_B T = 0.90\epsilon$  and  $k_B T = 0.95\epsilon$ . For  $k_B T = 0.90\epsilon$ ,  $\mathcal{R} = 7.77 \pm 0.04$  which is slightly

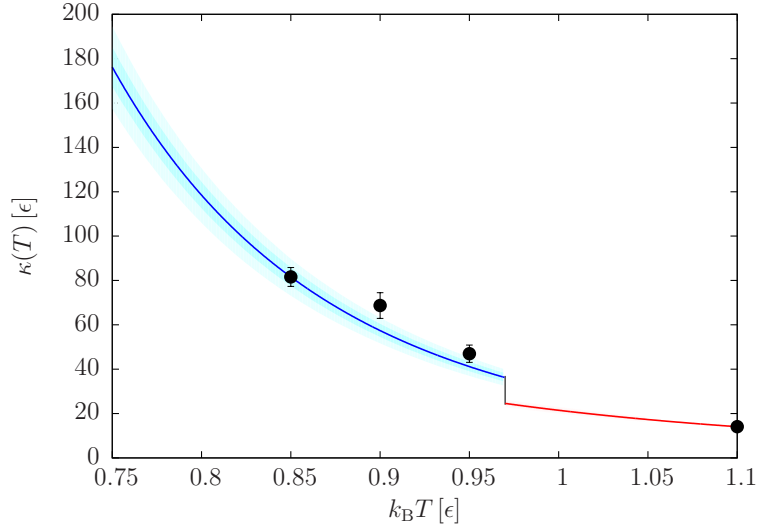


**Figure 3.26:** The temperature dependence of the bending modulus derived from analyzing the energetics of Cooke buckles is shown. The blue line is from the gel phase simulations at  $k_B T = 0.85 \epsilon$  with the dark and light cyan bands corresponding to the 68% and 95% confidence bands respectively. The red line is from the fluid phase simulations. There are also confidence bands for the fluid temperatures, but they are too small to be noticeable. The phase transition for the Cooke model is at  $k_B T_m = 0.97 \epsilon$ . The larger value of  $\mathcal{R}$  in the gel phase means that the bending modulus changes more rapidly than for the fluid phase. The black dots are the calculated values of  $\kappa$  using simulations of buckled membranes at the given temperatures. For the gel-phase, the derived temperature dependence of  $\kappa$  appears to slightly underestimate the value of  $\kappa$ , but it .

larger than for the buckle at  $k_B T = 0.85 \epsilon$ . At  $k_B T = 0.85 \epsilon$ ,  $\mathcal{R} = 15.5 \pm 0.2$  which is much larger than for the lower temperatures. Fig. 3.27 shows how the ratio changes with temperature.

We now turn to the energetics of the MARTINI model. Fig. 3.28 shows that at  $T = 265\text{K}$ ,  $\mathcal{R} = 8.71 \pm 0.04$ . This is almost double the value for the membrane in the fluid phase. Thus we suggest that the temperature dependence is greater for the MARTINI gel phase. Fig. 3.29 shows the predicted temperature dependence of  $\kappa$ . As with the Cooke model results, this is only an estimate, and its predictive power decreases as the temperature moves farther from the simulation temperature. Also, the behavior may be radically different in the temperature region around the main transition temperature, where in addition we cannot obtain valid results from simulations.

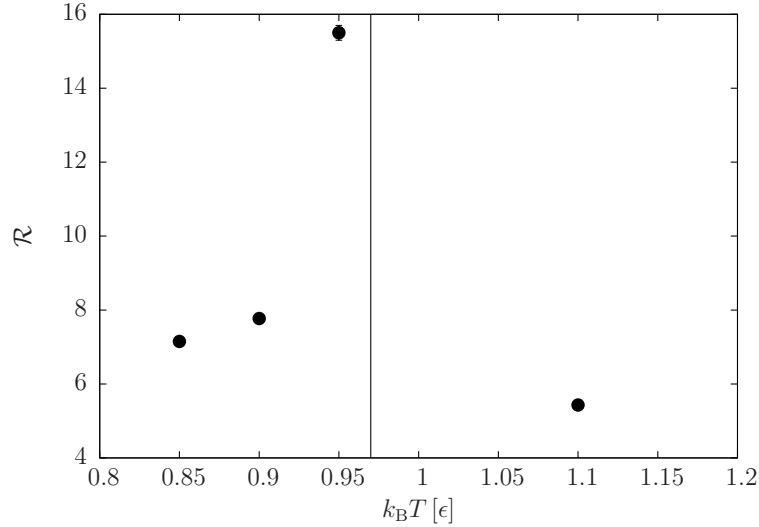


**Figure 3.27:** The temperature dependence of the value of  $\mathcal{R}$  for the Cooke model. The vertical black line marks the main transition temperature. For the gel phase,  $\mathcal{R}$  increases as the temperature gets closer to the transition temperature. In all cases,  $\mathcal{R}$  is larger for the gel phase than for the fluid phase.

### 3.5 Materials with Negative Compressibility

Recently, there has been a lot of effort in discovering, designing, and understanding materials that exhibit negative compressibility [9, 128–131]. This behavior has been observed in wide isotropic beams, metamaterials, and floating elastica. For most applications this is undesirable because it leads to large deformations and failure modes, but these properties can also enable novel application in mechanical sensors and microactuators [9]. This is especially true for thin materials that exhibit this behavior. Not only do the gel membranes have negative compressibility, but they are surprisingly thin compared to the other materials.

Oshri and Diamant have developed a framework for describing homogeneous thin compressible elastics from which our curvature functional (Eq. 3.1a) naturally arises. When combined with thin plate theory [76, 138], they can predict the value of  $\ell$  for compressible material, which they find to be very small,  $\ell = w/\sqrt{48}$ , where  $w$  is the thickness of the membrane. This implies that negative compressibility would occur only when the width-to-length ratio is greater than the critical ratio  $w/L > 2/\pi \approx 64\%$ , which corresponds to  $\delta = 1/\sqrt{3}$ , where thin-plate theory of course would no longer be valid. This dramatic difference in the value of  $\ell$  suggests that even though the gel membranes can be described with the same functional as compressible membranes, the underlying physics behind the phenomenon for gel membranes is not compressibility.

When finite-width corrections are accounted for, experiments and numerics have

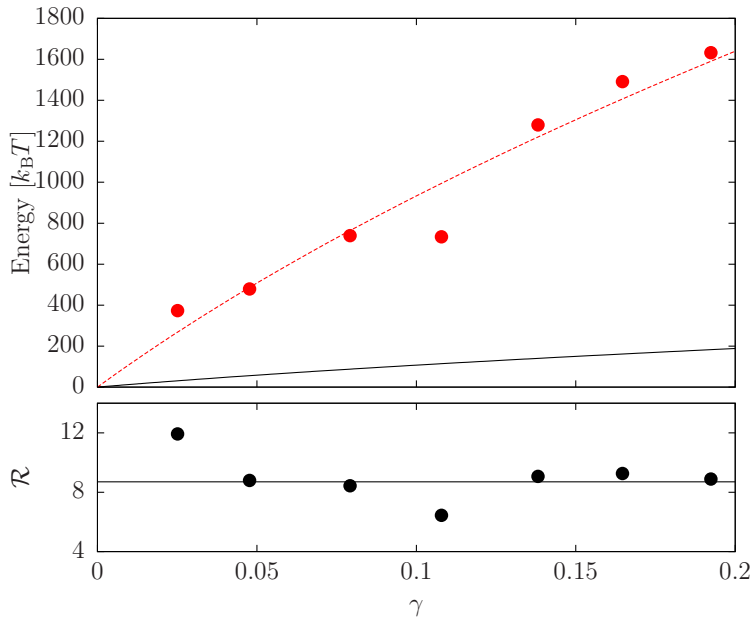


**Figure 3.28:** Top: The energy of the buckles versus the dimensionless strain for the MARTINI simulation. The red circles are the shifted potential energy of the buckles. The black line is the free energy of the buckles calculated from integrating the stress-strain relation derived from the new theory. The red line is the best fit curve assuming that the potential energy is a constant ratio of the free energy where  $\mathcal{R} = 8.71$ . Bottom: The ratio of the energy to the free energy for each simulation.

shown critical ratios of  $w/L$  as low as 12%. Some metamaterial beams have shown critical ratios as low as 5% [9]. In contrast, the Cooke and MARTINI models exhibit critical ratios of 1.8% and 2.6%, and thus have a more striking elastic response than state-of-the-art metamaterials. When we combine this with the fact that the main phase transition is tunable by lipid type and composition, these gel membranes are ideal model systems to test this exotic elasticity.

## 3.6 Discussion

We have shown that Helfrich theory does not accurately describe the buckling of gel-phase membranes. This is noticeable in the shape of the buckles as well as in the stress-strain relation. The membranes undergo curvature softening upon bending, which leads to curvature localization and negative compressibility. These effects can be described by a new energy density that is quadratic at low curvatures, but becomes asymptotically linear. With this new theory, we accurately describe both the shape and stress-strain relation, and from these, we extract the bending modulus as well

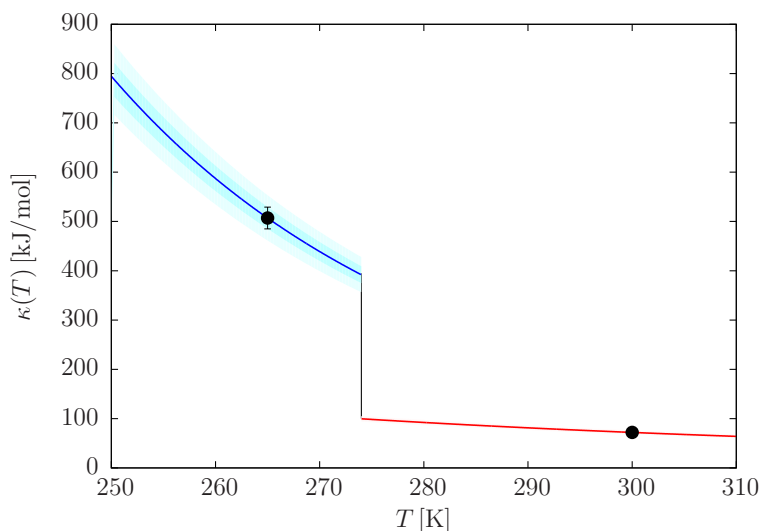


**Figure 3.29:** The temperature dependence of the bending modulus derived from analyzing the energetics of two MARTINI buckles (one each in the gel and fluid phase) is shown. The blue line is from the gel phase simulations with the dark cyan and light cyan bands corresponding to the 68% and 95% confidence bands respectively. The red line is from the fluid phase simulations. The phase transition for the MARTINI model is at  $T = 274$  K. The larger value of  $\mathcal{R}$  in the gel phase means that the bending modulus changes more rapidly than for the fluid phase.

as a new material parameter  $\ell$  that describes how the gel membrane physics deviate from Helfrich theory. Our new theory is only a phenomenological macroscopic theory and does not address the underlining microscopic physics behind the phenomenon.

We also note that both the Cooke model and MARTINI DMPC do not show intrinsic tilt in the gel phase. In fact this is one of the areas that MARTINI DMPC fails to properly model physical DMPC. However, the lack of tilt does not invalidate the finding because there are classes of lipids, such as PE lipids, that do not have an intrinsic tilt in their gel phase, but the theory may need to be further modified for lipids with intrinsic tilt. In fact, adding intrinsic tilt would potentially add new challenges because it would break a symmetry of the system. It has been shown that the fluctuation behavior of gel lipids is different along the tilt direction and against it [139]. This suggest that there could be a difference in the bending modulus depending on whether the tilt was along or across of the buckling direction.

The new insights into the mechanical properties by buckling gel-phase membranes will hopefully increase interest in the study of such materials. With a more complete understanding, these membranes may prove to be enticing parts of novel nanoscale systems.

## Chapter 4

# Revisiting the Buckling of Fluid Membranes

In this chapter, we reanalyze the fluid-phase buckles we first looked at in Chapter 2 with the theory described in Chapter 3. Recall that for the fluid phase buckles the stress-strain relationship predicted by Helfrich theory was a decent fit for the Cooke and MARTINI simulation results (Fig. 2.3, Fig. 2.4), and a poor fit for the Plum model (Fig. 2.5). The shape of the simulated buckles begin to diverge from the theoretical shape at larger strains (Figs. 2.16, 2.17, 2.18). The disagreement between the Euler and simulation shapes were smaller than what was seen for the gel-phase membranes, but still noticeable, suggesting that the fluid membranes might also have  $\ell$  values—small values, but not zero.

This possibility is compatible with previous findings because curvature softening has been observed in simulated membrane tethers. Assuming no curvature dependence to the bending modulus, the bending modulus is just Eq. 2.5 from Chapter 2 [103]. Results from Hu *et al.* [79] support a correction

$$\frac{F_z R_t}{2\pi} = \kappa + \frac{B}{R_t^2} \quad (4.1)$$

where  $B$ , a fitting parameter, is negative [108]. Let us begin by applying the new theory to membrane tethers and see if we get a similar result. The energy of the tether will be

$$E = A \frac{\kappa}{\ell^2} \left[ \sqrt{1 + K^2 \ell^2} - 1 \right], \quad (4.2)$$

where  $A = 2\pi R_t L_t$  is the surface area of the tether. The curvature of the tether is  $K = 1/R_t = 2\pi L_t/A$ , so the energy becomes

$$E = A \frac{\kappa}{\ell^2} \left[ \sqrt{1 + \left( \frac{2\pi \ell L}{A} \right)^2} - 1 \right]. \quad (4.3)$$

We now calculate the force required for holding the tether in place at constant area:

$$F_z = \left. \frac{\partial E}{\partial L_t} \right|_A = \frac{2\pi\kappa}{\sqrt{1 + (\ell/R_t)^2}}. \quad (4.4)$$

Thus,

$$\frac{F_z R_t}{2\pi} = \frac{\kappa}{\sqrt{1 + (\ell/R_t)^2}} \quad (4.5a)$$

$$\approx \kappa \left[ 1 - \frac{\ell^2}{2R_t^2} \right] \quad (4.5b)$$

Thus the fitting parameter in Eq. (4.1) is

$$B = -\frac{\ell^2}{2\kappa}, \quad (4.6)$$

showing that the empirical correction in Eq. (4.1) is indeed supplanted by our extension of Helfrich theory.

Using the data from Harmandaris and Deserno [103] gives  $\ell = 2.3 \pm 1.8\sigma$  for the Cooke model in the fluid phase. The data from Hu *et al.* [108] gives a value of  $\ell = 4.5 \pm 2.6\sigma$ . Fig. 4.1 shows a plot of  $F_z R_t / 2\pi$  as a function of  $R_t$  using the data from Hu *et al.* [108]. The fit using the new theory better describes the simulation results compared to Helfrich theory.

Turning from the tethers, in this chapter, we apply the same method of analyzing the shapes of the buckles to measure  $\ell$ , and then combine this with the stress to measure  $\kappa$ . We then look at how the new shape prediction improves on the Euler shape prediction. Next we look at the new predicted stress-strain relationship. Finally, we measure  $\ell$  and  $\kappa$  by fitting the theory directly to the stress-strain data taken from the simulations.

## 4.1 Analyzing the Shape of Fluid Membranes

We start this section by comparing the shape of the fluid simulations to the new theory for all three models. We then look at the predicted stress-strain relationship of the new theory.

### 4.1.1 Shape

Fig. 4.2 shows the same two fluid Cooke buckle simulations as we have previously seen, only this time the shape predicted by the new theory is also shown. In both cases, the new theory performs better than Helfrich theory. Fig. 4.3 shows the RMSD of both Helfrich and the new theory with respect to the simulations and confirms that the

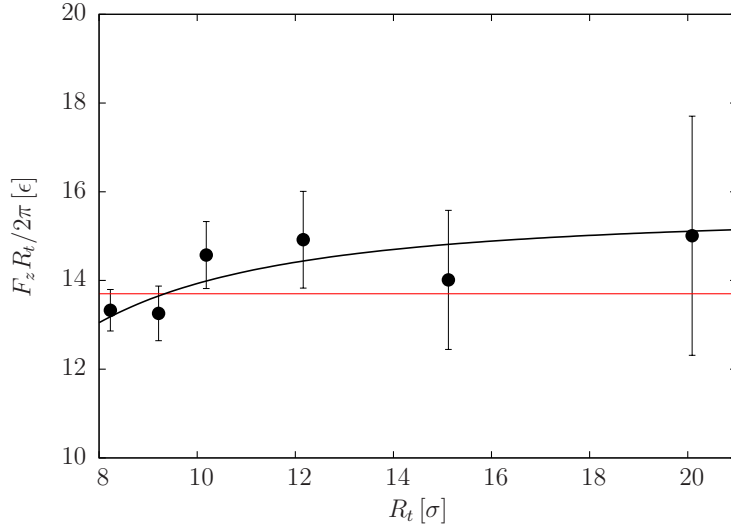


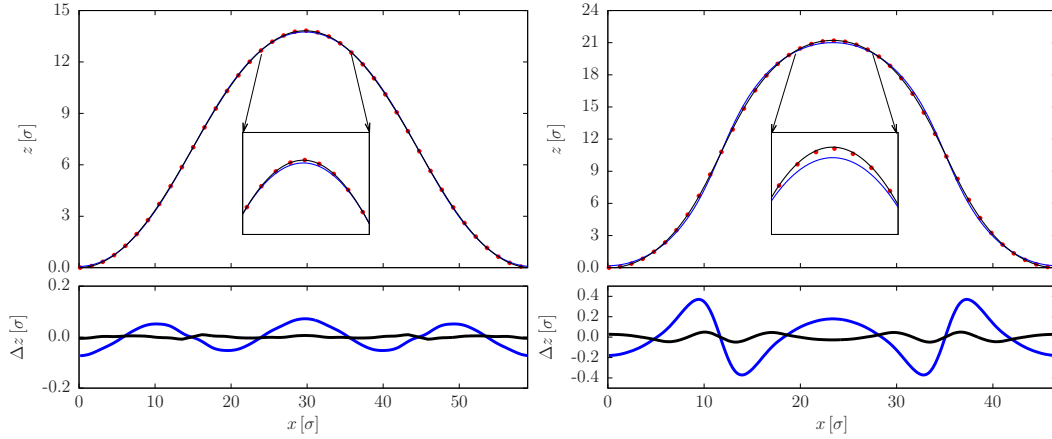
**Figure 4.1:** Graph of  $F_z R_t / 2\pi$  versus the radius of the tether  $R_t$ . If no correction is needed to Helfrich theory, then  $F_z R_t / 2\pi$  would be constant (red line). The black line is the prediction using theory described in Ch. 3 with  $\ell = 4.5$ . The fit using the new theory is superior to the prediction by Helfrich theory.

new theory describes the shape of buckles at higher strains much better than Helfrich theory. Fig. 4.4 and Fig. 4.5 show the shape analysis for the MARTINI model, while Fig. 4.6 and Fig. 4.7 show the same for the Plum model. In all cases, the new theory performs better at describing the averaged simulation shape than Helfrich theory.

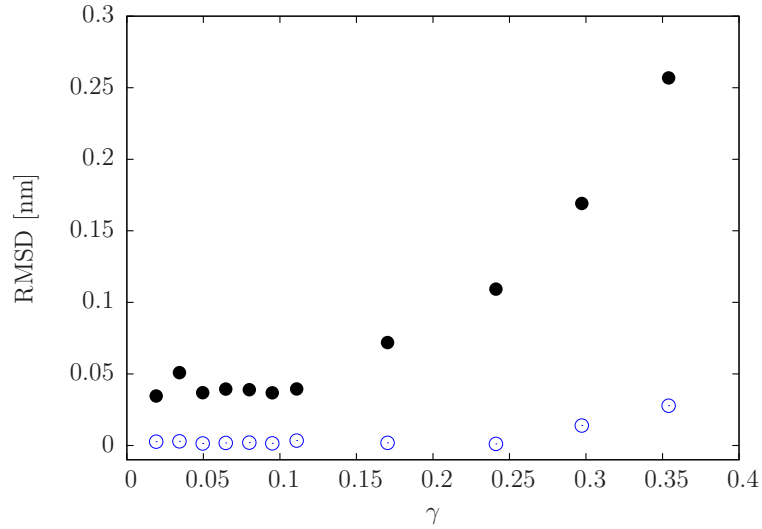
We now look at the measured values of  $\ell$  obtained by fitting the simulation shape to the theoretical shape. Fig. 4.8 shows  $\ell$  as a function of strain  $\gamma$ . For  $\gamma > 0.1$ ,  $\ell$  is constant, but for smaller strains,  $\ell$  is larger. Fitting  $\ell$  to a constant gives a value of  $\ell = 10.1 \pm 0.4 \sigma$ . This is smaller than for the gel phase by a factor of 2.7. This value of  $\ell$  corresponds to  $\delta = 0.95 \pm 0.04$ , which would imply that the fluid membranes are in the negative compressibility regime<sup>1</sup>. At small strains, the errors associated with the measurements are substantially larger. The shape barely changes with  $\ell$  meaning that the function we are trying to minimize during the fit (the squared difference between the theoretical and simulated shapes) is extremely flat around the minimum, and small errors in measuring the simulated shape can have a large effect.

Fig. 4.9 shows the characteristic length  $\ell$  versus the strain  $\gamma$  for the MARTINI fluid model. As with the Cooke model,  $\ell$  is constant for  $\gamma > 0.1$ . Fitting to a constant gives  $\ell = 8.1 \pm 0.8 \text{ nm}$ , which corresponds to  $\delta = 1.1 \pm 0.1$ . Thus in the fluid phase, the MARTINI membrane has a smaller value of  $\ell$  than in the gel phase, but the value for  $\delta$  would again imply that the MARTINI membrane also has negative compressibility,

<sup>1</sup>Recall that the critical value of  $\delta$ , beyond which the compressibility becomes negative, is  $\delta = 1/\sqrt{3} \approx 0.58$



**Figure 4.2:** Comparison between the average simulated, Helfrich predicted, and new theoretical buckle shape for two Cooke membranes. Top-left: The average shape of a buckle at  $\gamma = 0.11$  is shown in red circles. The blue line is the predicted Euler shape, and the black line is shape from the new theory. Bottom-left: The residual between the two theories and the simulated shape. The blue line is for Helfrich theory, and the black line is for the new theory. The RMSD for Helfrich is  $0.038\sigma$ , while the RMSD for the new theory is  $0.003\sigma$ . Both fits are good, but the new theory performs better. Top-right: The shape of a buckle at  $\gamma = 0.29$ . Bottom-right: The residues for the buckle at  $\gamma = 0.29$ . The RMSD for the Helfrich theory is  $0.17\sigma$  while the RMSD for the new theory is  $0.014\sigma$ .



**Figure 4.3:** The RMSD between the simulated shape and the Helfrich shape (black circles) and the new theoretical shape (blue open circles) for the Cooke buckles. For all strains, the new theory does better than the Helfrich theory.

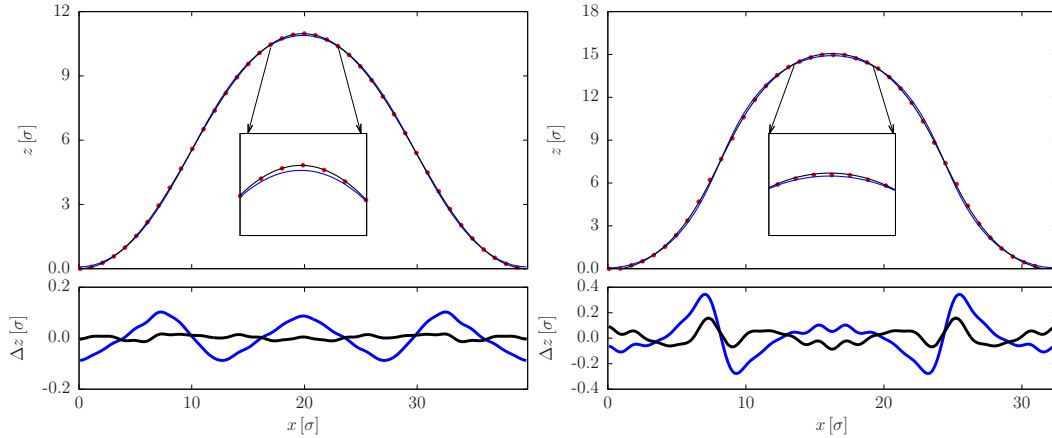


**Figure 4.4:** Comparison between the average simulated, Helfrich predicted, and new theoretical buckle shape for two MARTINI membranes. Top-left: The average shape of a buckle at  $\gamma = 0.15$  is shown. The symbols have the same meaning as in Fig. 4.2. Bottom-left: The residual between the two theories and the simulated shape. The RMSD for Helfrich is 0.053 nm, while the RMSD for the new theory is 0.008 nm. Both fits are good, but the new theory performs better. Top-right: The shape of a buckle at  $\gamma = 0.30$ . Bottom-right: The residuals for the buckle at  $\gamma = 0.30$ . The RMSD for the Helfrich theory is  $0.11 \sigma$  while the RMSD for the new theory is 0.048 nm.

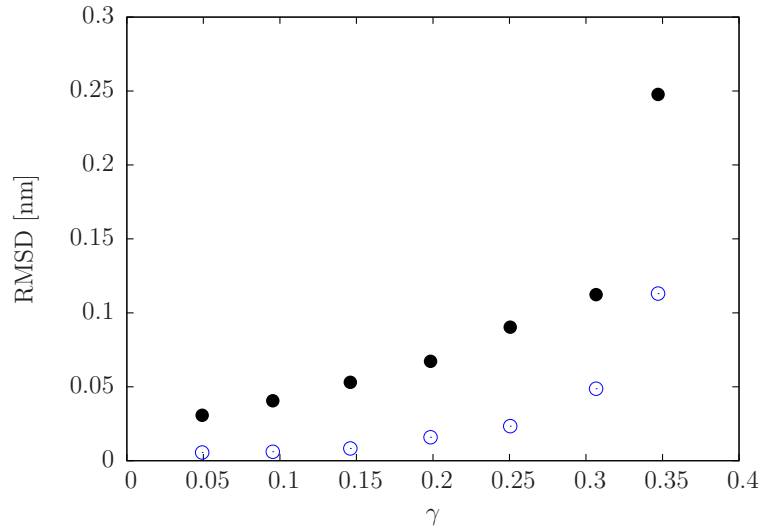


**Figure 4.5:** The RMSD between the simulated shape and the Helfrich shape (black circles) and the new theoretical shape (blue open circles) for the Martini buckles. For all strains, the new theory does better than the Helfrich theory.

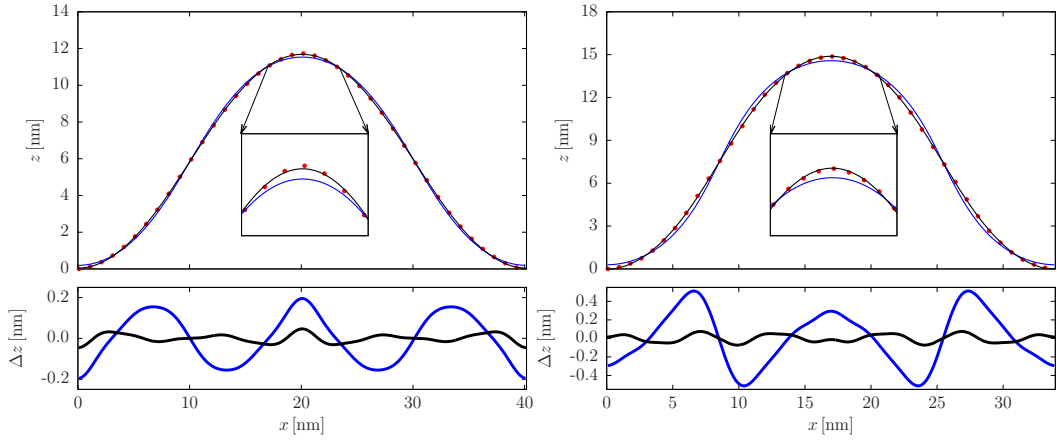


**Figure 4.6:** Comparison between the average simulated, Helfrich predicted, and new theoretical buckle shape for two Plum membranes. Top-left: The average shape of a buckle at  $\gamma = 0.16$  is shown. The symbols have the same meaning as in Fig. 4.2. Bottom-left: The residual between the two theories and the simulated shape. The RMSD for Helfrich is 0.11 nm, while the RMSD for the new theory is 0.02 nm. Top-right: The shape of a buckle at  $\gamma = 0.28$ . Bottom-right: The residuals for the buckle at  $\gamma = 0.28$ . The RMSD for the Helfrich theory is  $0.25\sigma$  while the RMSD for the new theory is 0.035 nm.

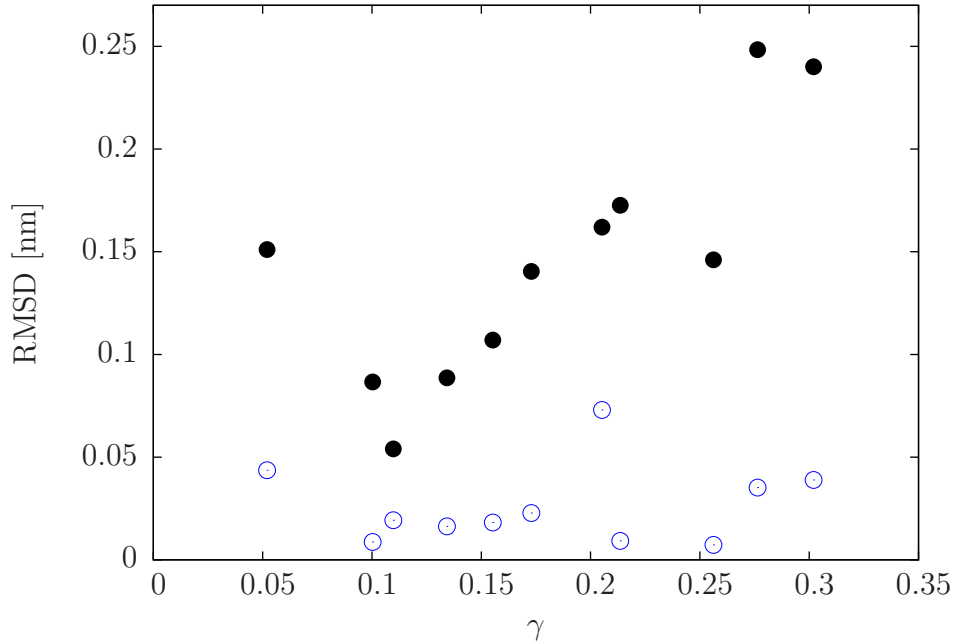


**Figure 4.7:** The RMSD between the simulated shape and the Helfrich shape (black circles) and the new theoretical shape (blue open circles) for the Plum buckles. For all strains, the new theory does better than the Helfrich theory.

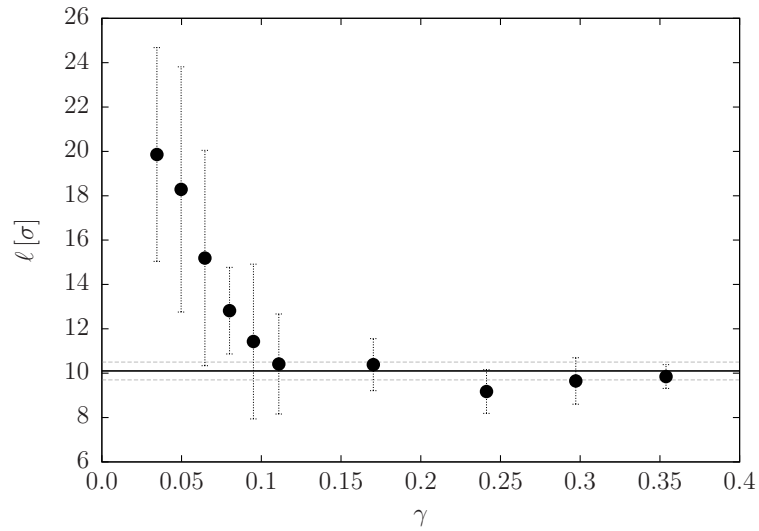


**Figure 4.8:** Graph of  $\ell$  versus the strain  $\gamma$  for Cooke fluid-phase membranes. At small  $\gamma$ ,  $\ell$  is consistently larger, though it also has much larger errors associated with it. This may be caused by the difficulty of measuring  $\ell$  for small strains.

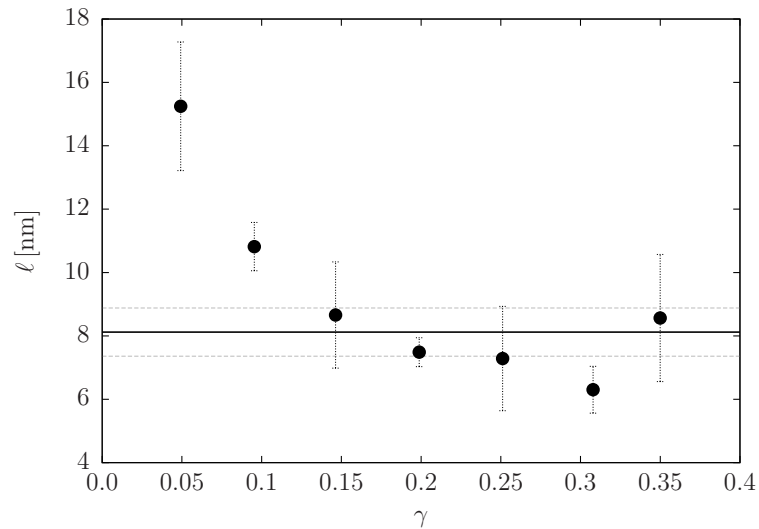


**Figure 4.9:** Graph of  $\ell$  versus the strain  $\gamma$  for MARTINI fluid-phase membranes. At small  $\gamma$ ,  $\ell$  is consistently larger just as with the Cooke model. This may be caused by the difficulty of measuring  $\ell$  for small strains.

but this could be caused by not measuring the average shape of the buckles to a high enough accuracy.

Fig. 4.10 shows  $\ell$  versus strain for the Plum fluid model. Fitting the simulation

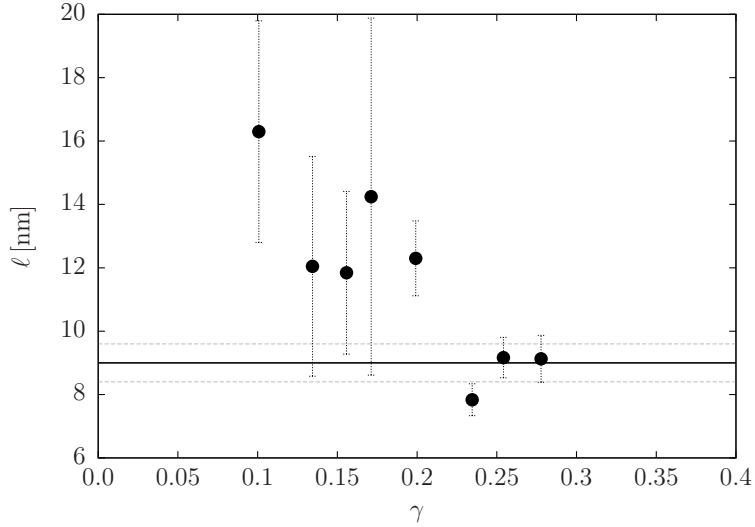


**Figure 4.10:** Graph of  $\ell$  versus the strain  $\gamma$  for the Plum fluid-phase membranes. The measurements at strains  $\gamma < 0.2$  are consistently larger than for larger strains, and they have much larger error bars.

values of  $\ell$  to a constant gives  $\ell = 9.0 \pm 0.6$  nm. This corresponds to  $\delta = 1.2 \pm 0.1$ . The Plum simulations at strains  $\gamma < 0.2$  have large error bars, stemming from the difficulty in measuring the shape of the Plum membranes.

For all three models, the measured values of  $\ell$  and  $\delta$  are surprisingly large. In addition, the standard deviations of the measurements at smaller strains are large. This all suggests that, at the moment, we may not be able to measure the shape of the fluid membranes (due to the way we handle fluctuations) sufficiently accurately. To confirm that there is a problem, we turn to the stress-strain relationship predicted by the shapes and show that it does not agree with the simulation results as well as Helfrich theory does.

### 4.1.2 Stress-strain Relationship from the Shape

Combining the shape analysis (specifically, the obtained value of  $\ell$ ) with the measured stress from the simulations, we calculate  $\kappa$  and the stress-strain relationship predicted by the new theory. Fig. 4.11, Fig. 4.12, and Fig. 4.13 show the stress-strain relationship for the Cooke, MARTINI, and Plum models respectively. For the Cooke and MARTINI membranes, the stress-strain relationship is plausible considering the data, but it fails to describe the data better than Helfrich theory. The new stress-strain relationship overestimates the stress at small strains, and underestimates it at large strains, which is opposite of what Helfrich theory predicts. Though the fit to the shapes is consistent with the simulation stress, this is more of a result of the large uncertainties than because the prediction matches the stress.

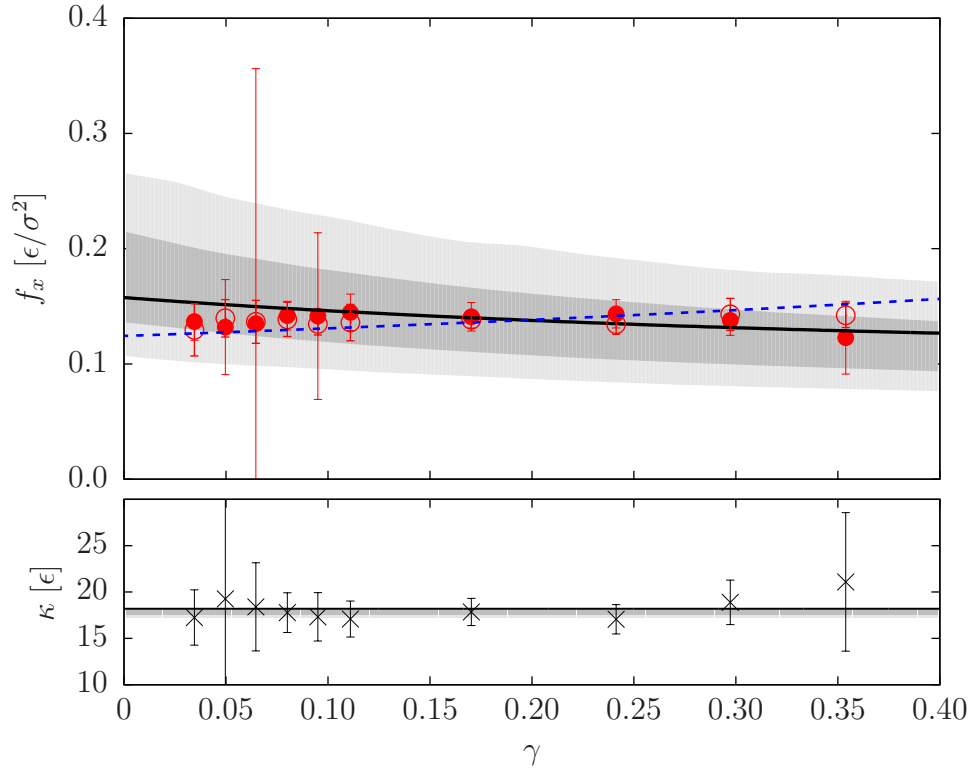


**Figure 4.11:** Top: The buckling stress  $f_x$  as a function of strain  $\gamma$  is plotted for the Cooke model. The open circles are calculated directly from the stress tensor. The filled circles are calculated by scaling  $\tilde{f}_x$  by  $\kappa/\ell^2$ , where  $\tilde{f}_x$  and  $\ell$  are calculated from the shapes of each simulation and  $\kappa$  is taken from the measured stresses by averaging over all simulations. The solid curve is the extended theory's prediction for  $f_x(\gamma)$  using the average value of  $\tilde{f}_x$  and  $\ell$  from the simulations. The 68% (dark gray) and 95% (light gray) confidence bands are based on resampling all data. The dashed blue line is an attempted fit to the Helfrich theory. Bottom: The bending rigidity  $\kappa$  derived from each simulation for the Cooke model. The black line is the average value of  $\kappa$  from all simulations, where  $\kappa = 17.7 \pm 0.3 \epsilon = 16.1 \pm 0.3 k_B T$ . The dark gray and light gray areas are the 68% and 95% confidence bands.

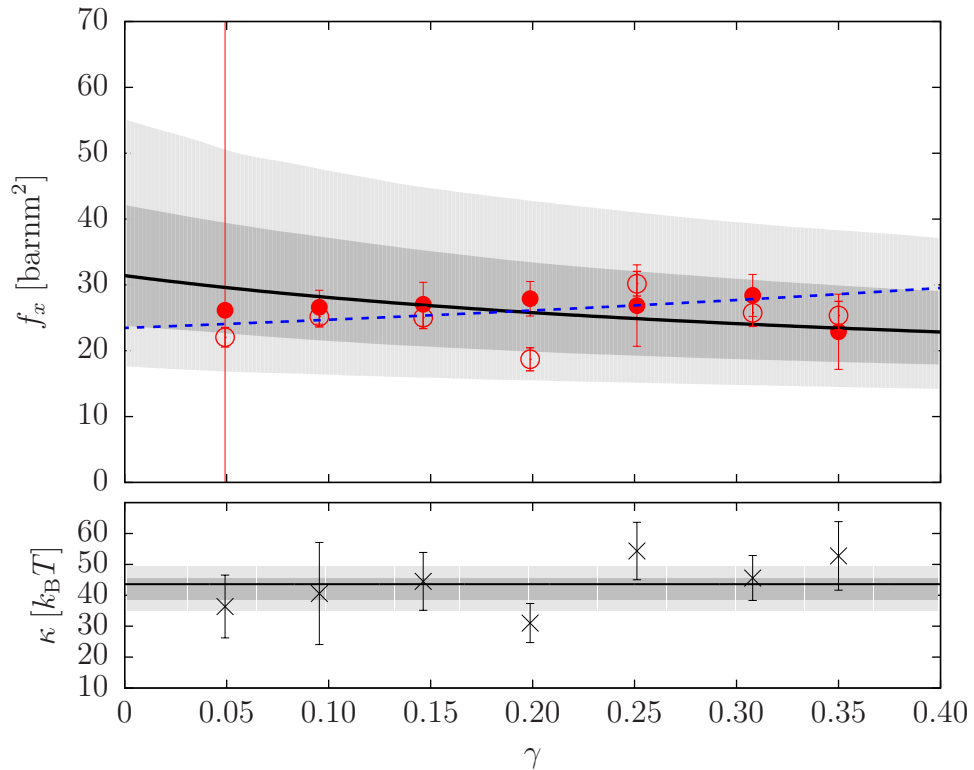


**Figure 4.12:** Top: The buckling stress  $f_x$  as a function of strain  $\gamma$  is plotted for the MARTINI model. The symbols have the same meaning as in Fig. 4.11. Bottom: The bending rigidity  $\kappa$  derived from each simulation for the MARTINI model. Fitting the data to a constant,  $\kappa = 42 \pm 3 k_B T$ .

For the Plum model, the predicted stress-strain relationship does a remarkably poor job of reproducing the stress measured directly from the simulations. Fig. 4.13 shows that the shape fit massively overestimates the stress at smaller strains. In addition, it predicts that the membrane has a negative compressibility while the stress is clearly increasing with strain. This is not the fault of the theory itself; rather, it is because we cannot calculate the shape of Plum buckles correctly due to the large fluctuations that occur during the simulations.

For all three models, the results from fitting to the shape suggest that the membranes should have negative compressibility. The stress from the simulations does not support this finding. This disagreement strongly suggests that there is a problem, at least for the fluid buckles, with how we are measuring the shapes of the buckles. It appears that a systematic error enters the average shape when we incorporate snapshots from a simulation when the buckle is undergoing a large fluctuation.

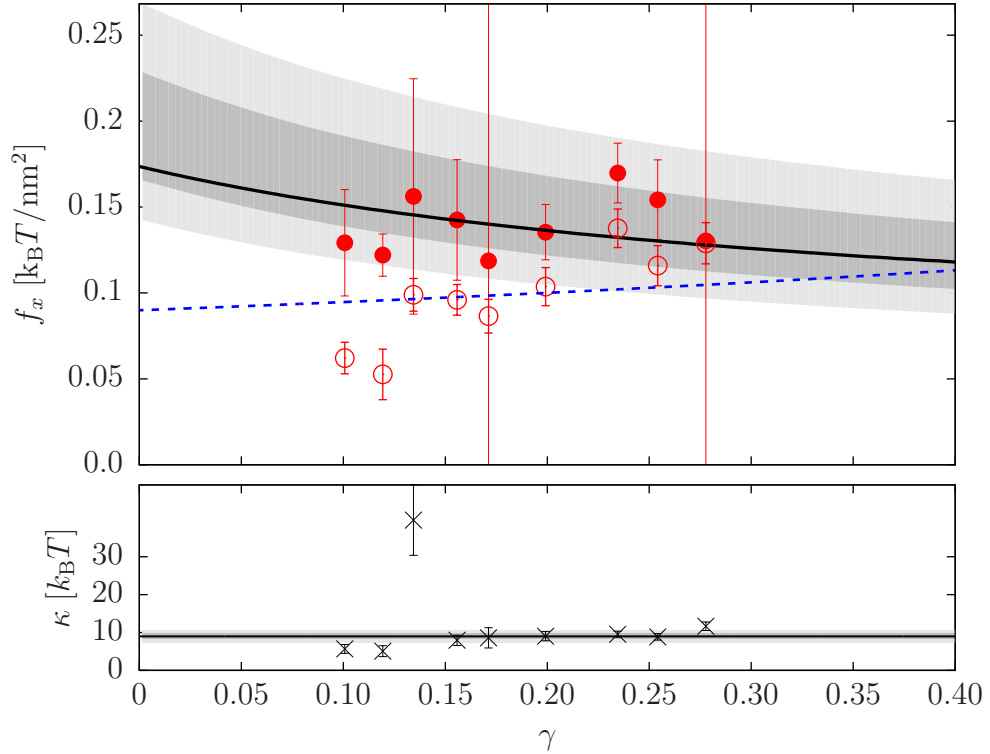


**Figure 4.13:** Top: The buckling stress  $f_x$  as a function of strain  $\gamma$  is plotted for the Plum model. The symbols have the same meaning as in Fig. 4.11. Unlike the other two models, the predicted stress (filled red circles) for each simulation is consistently larger than the actual measured stress (open circles). This causes the predicted stress-strain relationship to fail to match the stress measured from the simulations. This result suggests that we were unable to measure the shape correctly. Bottom: The bending rigidity  $\kappa$  derived from each simulation for the Plum model. Fitting the data to a constant,  $\kappa = 9.0 \pm 0.8 k_B T$ . The measured value for  $\kappa$  for  $\gamma = 0.13$  is much larger than for the other simulations.

## 4.2 Fit to Stress-strain Relationship

### 4.2.1 Stress-strain Relationship

Instead of relying on the analysis of the shape of the buckles to measure  $\ell$ , we can obtain  $\ell$  and  $\kappa$  by numerically fitting to the stress-strain relationship instead of to the shape of the buckles. For the Cooke model, the best fit is with  $\kappa = 14.9 \pm 0.8 \epsilon = 13.5 \pm 0.7 k_B T$  and  $\ell = 5.3 \pm 2.1 \sigma$ , which is over 5 times as small as in the gel phase. This bending modulus is slightly larger than the value obtained using Helfrich theory, though they are within error bars of each other. This value of  $\ell$  corresponds to  $\delta = 0.5 \pm 0.2$ , which is below to the transition to negative compressibility. Fig. 4.14 compares the stress-strain relationship for these values of  $\kappa$  and  $\ell$  to the prediction by

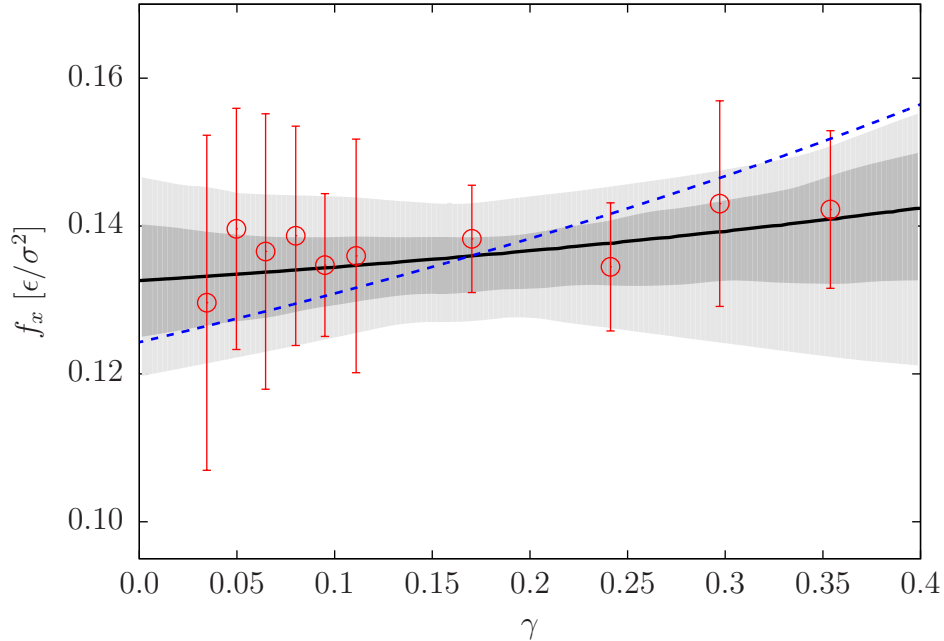


**Figure 4.14:** The buckling stress  $f_x$  as a function of strain  $\gamma$  for the Cooke model. The open circles are calculated directly from the stress tensor. The dashed blue line is the fit to the Helfrich theory from Chapter 2. The solid black curve is the fit for  $\delta$  and  $\kappa$  directly from the stress tensor measurements. The 68% (dark gray) and 95% (light gray) confidence bands are based on resampling the stress tensor measurements.

Helfrich theory. Not surprisingly, the new fit does a better job than Helfrich theory matching the simulations, by decreasing the rate at which the stress increases with strain.

For the MARTINI simulations, fitting to the stress-strain relationship gives  $\kappa = 30.5 \pm 1.3 k_B T$  and  $\ell = 1.76 \pm 1.64$  nm, which corresponds to  $\delta = 0.24 \pm 0.22$ . Thus fitting to the stress suggests that the MARTINI membrane is almost an Euler buckle. Fig. 4.15 shows the fitted stress-strain relationship.

For the Plum simulations, the stress actually increases with strain faster than predicted by Helfrich theory, which cannot be described by the new theory. Thus, the best fit is with  $\ell = 0$ , corresponding to Helfrich theory. The Plum model has unusual behavior compared to the other models, but the new theory does not improve on Helfrich theory in describing the model.

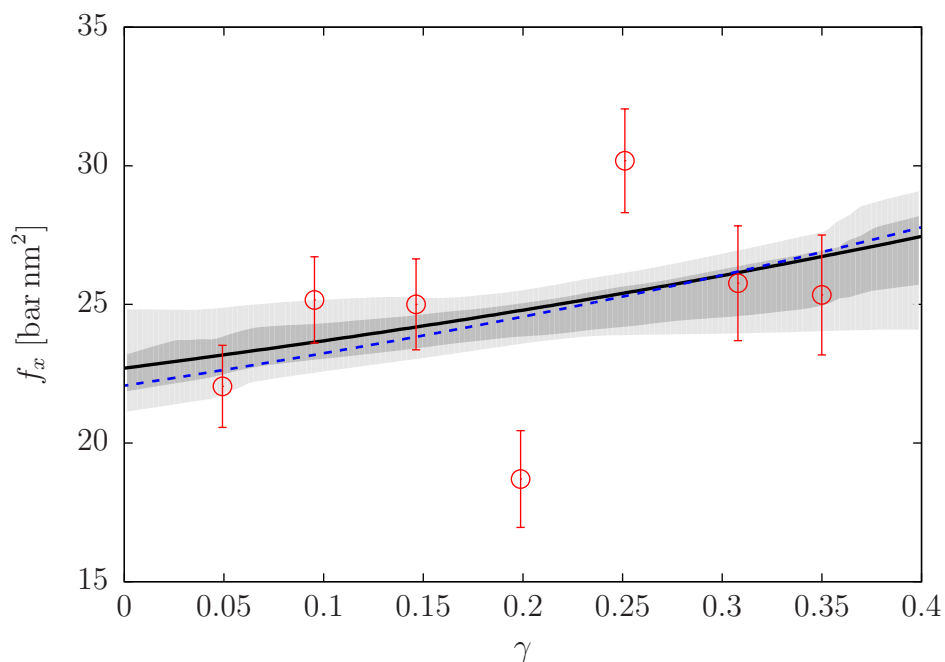


**Figure 4.15:** The buckling stress  $f_x$  as a function of strain  $\gamma$  for the MARTINI model. The symbols and curves have the same meaning as in Fig. 4.14

### 4.2.2 Shape

For completion's sake, we now check how the predicted shape using the characteristic length  $\ell$  obtained by the stress fit compares to the simulation shape. From our attempts to fit the new theory to the shape, we infer that there are problems with the way that we averaged the shape. Fig. 4.16 shows the RMSD for the Cooke membranes. The results are better slightly better than those from Helfrich theory, and the direct fit from Chapter 2 is still better. For the MARTINI membranes (Fig. 4.17), there is very little difference in the RMSD for the stress fitted shapes and the Helfrich buckles, since  $\ell$  is so small.

## 4.3 Summary of Material Parameters

Table 4.1 presents the values for  $\kappa$  and  $\ell$  of the three models discussed in this chapter. As discussed previously, the values of  $\ell$  obtained by fitting the new theory to the shapes are unrealistically large. This also leads to substantially larger values for  $\kappa$ . Fitting the new theory directly to the stress of the simulated buckles gives much smaller values of  $\ell$ , including 0 for the Plum model. The MARTINI model shows very little change from the values obtained using Helfrich theory. The Cooke model has the largest  $\ell$ , in fact it is just below the transition to negative compressibility. As

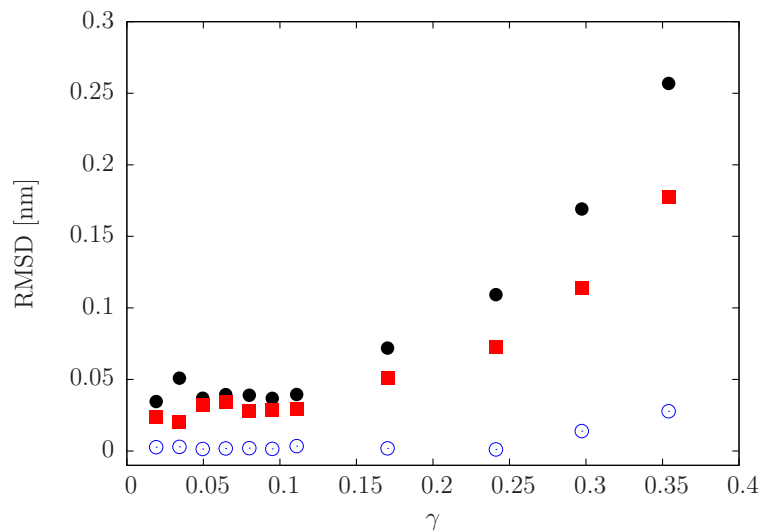


**Figure 4.16:** The RMSD between the simulated shape and the Helfrich shape (black circles), the theoretical shape fitted to the simulated shape (blue open circles), and the theoretical shape using the value of  $\ell$  from fitting directly to the stress-strain relationship (red filled square) for the Cooke buckles.

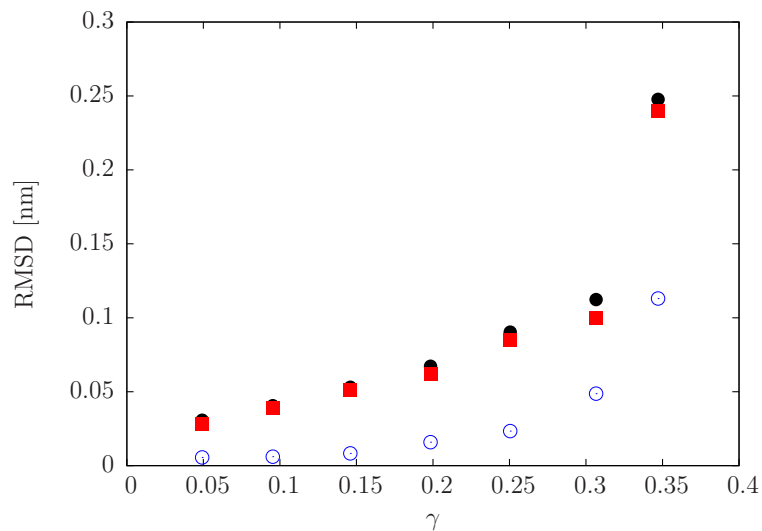


**Figure 4.17:** The RMSD between the simulated shape and the Helfrich shape (black circles), the theoretical shape fitted to the simulated shape (blue open circles), and the theoretical shape using the value of  $\ell$  from fitting directly to the stress-strain relationship (red filled square) for the MARTINI buckles.

Model	Helfrich		Shape Fit		Stress Fit	
	$\kappa [k_B T]$	$\ell$	$\kappa [k_B T]$	$\ell$ [nm]	$\kappa [k_B T]$	$\ell$ [nm]
Cooke	$12.8 \pm 0.4$	n/a	$16.1 \pm 0.3$	$11.1 \pm 0.4$	$13.5 \pm 0.7$	$5.8 \pm 2.3$
MARTINI	$29.0 \pm 1.0$	n/a	$42 \pm 3$	$8.1 \pm 0.8$	$30.5 \pm 1.3$	$1.76 \pm 1.64$
Plum	$5.49 \pm 0.4$	n/a	$9.0 \pm 0.8$	$9.0 \pm 0.6$	$5.49 \pm 0.4$	0

**Table 4.1:** Summary of the measured material values for the three models obtained by either fitting the stress using Helfrich theory, fitting the shapes of the buckles using the new theory, or fitting the stress using the new theory. Fitting using the shape gives values of  $\ell$  that are unrealistically large. Fitting the stress-strain relationship using the new theory shows an improvement over Helfrich, theory while changing  $\kappa$  by a few percent. Using the new theory to fit the stress for the Plum model gave the same result as with the Helfrich theory.

a result,  $\kappa$  increased by almost five percent.

## 4.4 Discussion

In this chapter, we have applied the theory presented for gel-phase membranes in Chapter 3 to the fluid-phase membranes discussed in Chapter 2. Specifically, we have fitted the new theory to the shapes of the simulated buckles and to the stress-strain relationship. For the Cooke and MARTINI models, both techniques give a non-zero  $\ell$  and a larger value of  $\kappa$  compared to Helfrich theory. Unfortunately, there is a substantial discrepancy in the values obtained from the two fitting techniques. Fitting to the shapes consistently gives unrealistically large values of  $\ell$  and the resulting theoretical stress-strain relationship does not match the simulations. Fitting to the stress directly gives more believable results and improves on Helfrich theory in describing the stress, though its improvement on describing the shapes compared to Helfrich theory is small.

Qualitatively, the results support the theory that the Cooke and MARTINI membranes undergo curvature softening compared to Helfrich theory. The extent is much smaller than in the gel-phase.

We believe that the discrepancy in results from fitting to the shape or the stress stems from the way that we average the simulation shapes, which struggles with large fluctuations in the shape. The lack of large fluctuations in the gel-phase case explains why we did not have this problem in Chapter 3. A better understanding of the fluctuations around the ground state is necessary before we can confidently extract material parameters from the shape.

# Chapter 5

## Coarse-graining Elastic Networks

We now turn our attention away from membranes and explore a technique to create coarse-grained elastic networks. As we mentioned in Chapter 1, networks have proven useful in investigating the thermal motions of proteins [62–75] and RNA [140–147]. In addition, the relative simplicity of networks make them attractive models to study the theoretical underpinnings of coarse-graining [148].

Though simple networks are surprisingly useful, there is always a desire to improve them. The most common way to improve an elastic network<sup>1</sup> is to iteratively refine the spring constants by comparing the fluctuations of the network in an MD simulation with an all-atom reference simulation [71]. This can lead to very accurate networks, but is computationally expensive, primarily because it requires an atomistic simulation to be performed.<sup>2</sup>

In this chapter, we will discuss a procedure to efficiently create a low resolution elastic network that accurately preserves the fluctuations of the protein. The method involves first creating a Hessian network,<sup>3</sup> which requires us to calculate the Hessian matrix of a suitably chosen high resolution model. Next, the unwanted degrees of freedom of the Hessian network are integrated out, which creates a low resolution Hessian network. We then create an elastic network from the low resolution model. The accuracy of the final elastic network depends on which particles are removed, and an efficient search to determine which particles to remove will improve the accuracy of the method, all without the need for an atomistic reference.

We test the method with a protein and RNA crystal structure. For both cases, the choice of which particles to remove has a large effect on the ability of the final elastic network to reproduce the fluctuations of the high resolution model. This choice of particles to remove will be called the “reduction”. In this chapter we focus

---

<sup>1</sup>We remind the reader that by “elastic network” we mean a network that depends on the distance between particles. This is not to be confused with a Gaussian network.

<sup>2</sup>If we had to perform an atomistic simulation for every network we wanted to make, we might as well just run atomistic simulations.

<sup>3</sup>A reminder: a Hessian network is quadratic with respect to the displacement of particles from their equilibrium position.

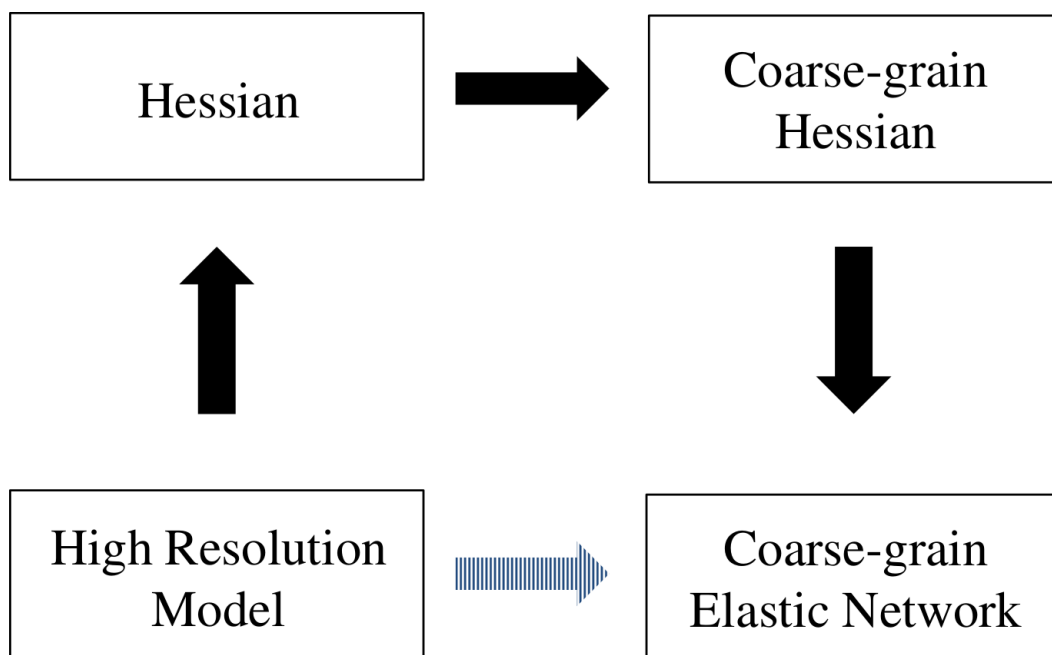


**Figure 5.1:** Anticipated work flow of the proposed method. The goal is to create the CG EN from the high resolution protein model (blue arrow). In order to do to this, we first must calculate the Hessian from the protein model. We then calculate the CG Hessian from the high resolution Hessian. Finally, we create a CG EN from the coarse-grained Hessian.

on describing the strength of different reductions without the need to run an MD simulation, as well as ways to search for preferable reductions.

## 5.1 Theory

The method to create the coarse-grained (CG) elastic network (EN) consists of three parts:

1. Calculate the high resolution Hessian matrix,
2. Calculate the low resolution Hessian matrix by integrating out the degrees of freedom of some particles,
3. Create the low resolution EN from the low resolution Hessian matrix.

The flow of the method is shown in Fig. 5.1. We now go into each part in greater detail.

### 5.1.1 Creating the Hessian

The first step is to calculate the Hessian matrix from the high resolution model. The Hessian matrix is a square matrix that contains all second order derivatives of the potential energy of the protein model:

$$H_{i,j}^{\mu,\nu} = \frac{\partial^2 E}{\partial r_i^\mu \partial r_j^\nu}, \quad (5.1)$$

where  $i, j$  are the labels of the particles and  $\mu$ , and  $\nu$  denote the spatial components. Thus, the Hessian matrix for a system of  $N$  particles is a  $3N \times 3N$  matrix. The Hessian can be partitioned into  $3 \times 3$  submatrices, each of which represents the interaction between two particles. The eigenvalues of the submatrix correspond to the strength of the interaction in the principle axis between the particles (along the axis between the two particles and two other perpendicular positions). If the original interaction is only along the axis between the two particles, then the submatrix only has one non-zero eigenvalue.

We can always calculate the Hessian using the definition (Eq. 5.1), but for certain models, the Hessian can be calculated easier. For example, the Hessian matrix for the Gaussian network model described in Chapter 1 is just the spring constant times the Kirchhoff matrix [63]. For elastic network models, the elements of the Hessian can be calculated using [149]

$$H_{i,j}^{\mu,\nu} = k_{ij} d_{ij}^\mu d_{ij}^\nu - \delta_{ij} \sum_l k_{il} d_{il}^\mu d_{il}^\nu, \quad (5.2)$$

where  $k_{ij}$  is the spring constant between particles  $i$  and  $j$  and  $d_{ij}^\mu$  is the  $\mu$  component of the unit vector between particles  $i$  and  $j$

$$d_{ij}^\mu = \hat{d}_{ij} \cdot \hat{e}^\mu. \quad (5.3)$$

### 5.1.2 Creating the Coarse-Grained Hessian

When we say that we are going to create a coarse-grained Hessian, we mean that from the original Hessian, we will create a Hessian with fewer degrees of freedom, such that the partition function  $Z$  for the Hessian network of both the original and CG Hessian will agree up to a constant.

Ignoring the kinetic part of the free energy (which will only change  $Z$  by a constant), the partition function is

$$Z \propto \int d\vec{r} \exp\left(\frac{-\beta}{2} \delta\vec{r}^\top \mathbf{H} \delta\vec{r}\right), \quad (5.4)$$

where  $\delta\vec{r}$  is the vector of the changes in position of the system with respect to the equilibrium position (1.4).

We partially calculate the partition function by integrating out the degrees of freedom associated with the particles that we want to coarse grain away. Let the particles that we want to remain be in set  $A$ , while the particles we remove are in set  $B$ . This leaves the partition function in the form

$$Z \propto \int d\vec{r}_A \exp\left(\frac{-\beta}{2} \delta\vec{r}_A^\top \mathbf{H}_{\text{CG}} \delta\vec{r}_A\right), \quad (5.5)$$

where  $\vec{r}_A$  is the vector of the positions for all particles in set  $A$ . We now have a coarse grained model with the remaining particles whose interactions are defined by this new Hessian  $\mathbf{H}_{\text{CG}}$

In order to calculate  $\mathbf{H}_{\text{CG}}$ , we first partition the Hessian into four parts: the submatrix representing the particles in group  $A$ , called  $\mathbf{H}_A$ , the submatrix representing the particles in group  $B$ , called  $\mathbf{H}_B$ , the submatrix of interactions between particles in group  $A$  and group  $B$ , called  $\mathbf{G}$  and the transpose of  $\mathbf{G}$ :

$$\mathbf{H} = \begin{pmatrix} \mathbf{H}_A & \mathbf{G} \\ \mathbf{G}^\dagger & \mathbf{H}_B \end{pmatrix} \quad (5.6)$$

We can then calculate the CG Hessian using the formula [66, 69, 72]

$$\mathbf{H}_{\text{CG}} = \mathbf{H}_A - \mathbf{G}\mathbf{H}_B^{-1}\mathbf{G}^\dagger. \quad (5.7)$$

This equation is exact, and thus nothing about the partition function has been lost in the process<sup>4</sup>. The bottleneck in terms of computational efficiency is in calculating the inverse of  $\mathbf{H}_B$ , which will be large if we want to coarse grain away most of the particles in the system.

### 5.1.3 Creating the Coarse-Grained Elastic Network

Now that we have a CG Hessian, we want to create an anisotropic elastic network from the Hessian. If the Hessian was calculated from an elastic network, the easiest way we could obtain the spring constants is by taking the trace of the submatrix that corresponds to the correct particles. This is because each submatrix would have only one non-zero eigenvalue, and that eigenvalue is equal to the spring constant.

Unfortunately, the CG Hessian is no longer representable by an elastic network. By this, we mean that no elastic network can produce this Hessian. There is a subgroup of all possible Hessians that correspond to elastic networks. The CG process (5.7) leads the CG Hessian out of this subgroup, even if the original Hessian network came from an elastic network. If we want a CG elastic network, we have to choose a network that approximates the CG Hessian. For example, we could still choose to create an EN whose spring constants correspond to the trace of the corresponding submatrix

---

<sup>4</sup>This is quite rare for coarse-graining methods.

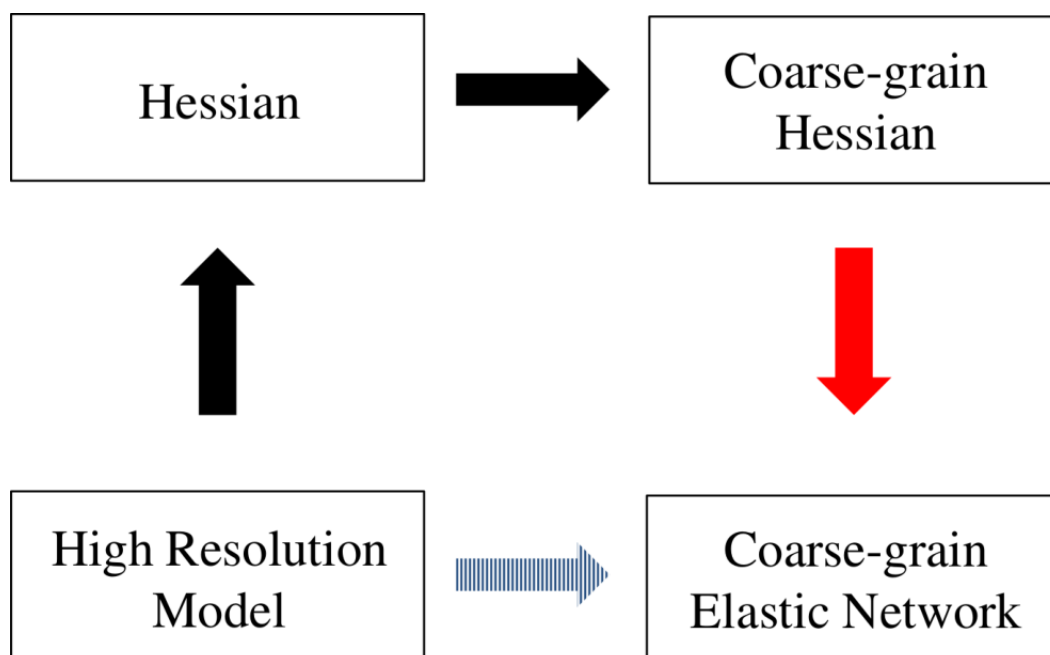


**Figure 5.2:** Figure shows another interpretation of the flow of the method. The red arrow represents that the process to go from the coarse grain Hessian to the elastic network adds the most error to the process.

of the CG Hessian. There are multiple ways to define the EN, and we will discuss two of the most obvious ones later in the chapter. Two questions naturally follow: (1) what is the best way to choose the EN from the CG Hessian and (2) does the quality of the final CG EN depend on the CG Hessian from which it was made? These are the two questions that we address in the rest of the chapter.

At this point, it is fair to ask why we even bother converting the CG Hessian to an elastic network. The answer is that we want a CG model that is not dependent on the reference state  $\vec{r}_0$ . Elastic networks only depend on the distance between particles and thus can be expressed as a forcefield. This gives us more flexibility in how we can use the network. First, we can easily run an MD simulation with an elastic network. We can also easily combine the network with a higher resolution model as part of a multi-resolution molecular dynamics simulation [150]. Such simulations separate a system into high and low resolution regions, where a high-resolution model (such as an all-atom forcefield) is used for the part of a protein that we want to pay special attention to and a low-resolution model (such as a CG elastic network) is used for the remaining and mostly rigid parts of the protein. This way the majority of computational effort is spent on the important region of the simulation.

## 5.2 Metrics to determine quality of CG Elastic Networks

In order to investigate how the elastic networks we obtain from different reductions<sup>5</sup> differ in terms of quality. To this end, we need to develop a metric that describes how well the network for one reduction will perform compared to another reduction. We start by creating a metric for the individual interactions between particles. To do this, we look at the ratio  $r_\lambda$  of the second largest eigenvalue to the largest eigenvalue of the interaction submatrix.<sup>6</sup> When  $r_\lambda = 0$ , there is only one non-zero eigenvalue and the interaction can be exactly represented as a spring. As the ratio increases from zero, the interaction is no longer just radial and therefore cannot be exactly represented as an interaction in an elastic network, but if the second eigenvalue is very small compared to the largest, the majority of the interaction is still radial. The worst possible interactions to be treated as a spring occur when  $r_\lambda = 1$ , in which case the interaction strength perpendicular to the radial direction is as strong as in the radial direction. For sub-matrices which have imaginary eigenvalues, we use the magnitude of the eigenvalue, which are in fact the only cases where we find  $r_\lambda = 1$ . The fact that there can be imaginary eigenvalues shows the danger of interpreting the CG Hessian as describing physical interactions.

Now that we have a way to describe individual interactions, we can use it to rate the entire reduction. There are many potential metrics that we could use, of which we will now discuss two. First, we could decide that the effective EN bond we get from a submatrix of the Hessian is acceptable as long as the ratio is below a certain cutoff  $r_{\lambda,c}$ . We then judge each CG reduction by the fraction of acceptable bonds

$$f_g = \frac{\sum_i \Theta(r_{\lambda,c} - r_{\lambda,i})}{N}, \quad (5.8)$$

where  $N$  is the total number of bonds and  $\Theta$  is the unit step function. We will refer to this as the “good bond fraction”. A larger number corresponds to a better CG network with a value of one being the best possible. This metric assumes that all bonds that fall in one of the categories (“good” or “bad”) have the same effect on the final network. The second metric is to look at the average ratio for all the interactions

$$f_a = \frac{\sum_i r_{\lambda,i}}{N} \quad (5.9)$$

where  $N$  is the total number of bonds. Smaller values of  $f_a$  correspond to better CG networks. This metric has the benefit that we do not have to choose a cutoff value. In an upcoming section, we will compare the two metrics for different reductions.

---

<sup>5</sup>As a reminder, we are using “reduction” to mean a specific set of particles that we are removing from the high resolution model.

<sup>6</sup>Care:  $r_\lambda$  stands for the ratio of eigenvalues and not for a distance.

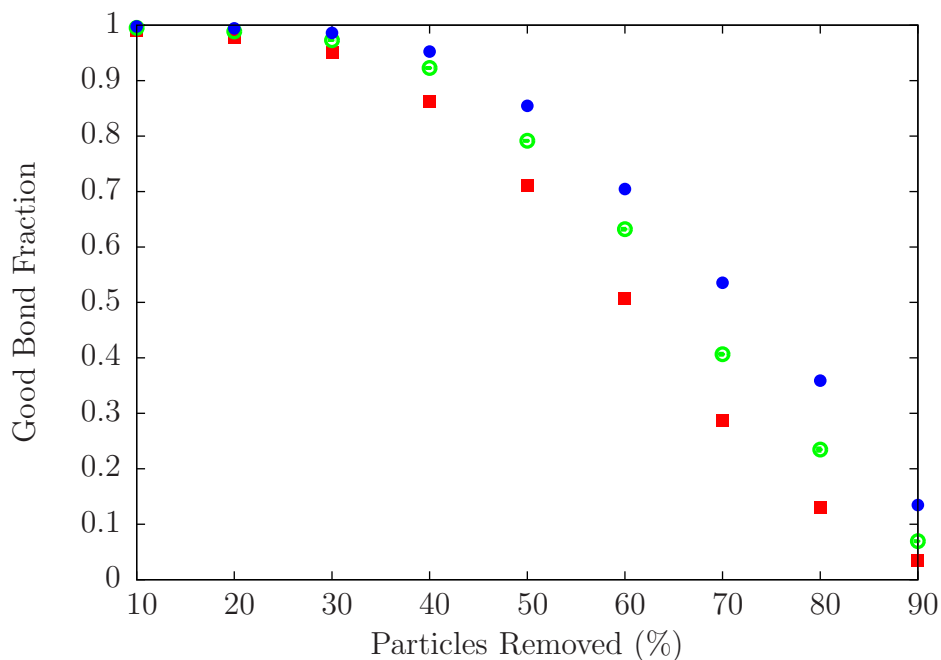


**Figure 5.3:** Average value of the good bond fraction for different starting configurations of a toy polymer model. Each point is the average value from 1000 different random reductions. The red squares are for models with 500 initial particles. The green open circles have 1000 initial particles. The blue filled circles have 2000 initial particles. The CG networks for larger systems perform better than smaller systems when the same percentage of particles are removed. As we remove more particles, the good bond fraction gets worse.

### 5.3 Effects of System Size and Number of Removed Particles on Metrics

We start by looking at a toy model of a polymer, where particles are randomly placed one  $\sigma$  away from the previous particle as long as they do not overlap with any other particles. Once all the particles have been placed, springs are attached between particles that are within  $4\sigma$  of each other. We created 3000 different random networks; 1000 with 500 initial particles, 1000 with 1000 starting particles, and 1000 with 2000 starting particles. We then removed different percentages of particles and calculated the good bond fraction with  $r_{\lambda,c} = 0.01$ . Fig. 5.3 shows the results for the good bond fraction. The first trend to notice is that the average good bond fraction decreases as we remove more particles, so the more particles we remove the worse the average network will be. Second, the larger the initial system, the better the average good bond fraction for the same percentage of particles removed. We find the same trends when we instead use the average ratio as our metric.

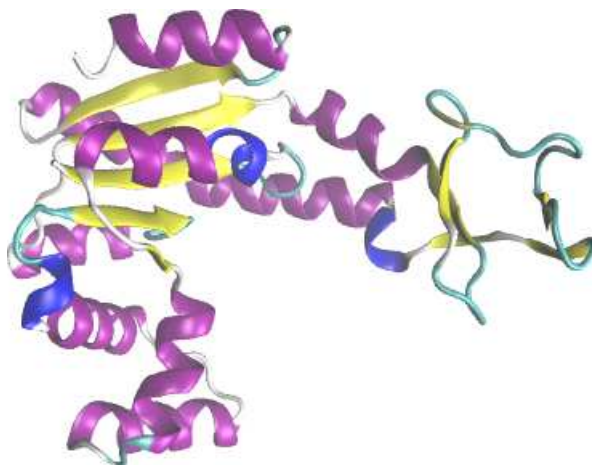


**Figure 5.4:** Image of the crystal structure of a conformation of Adenylate Kinase.

## 5.4 Elastic Networks for Protein Molecule

We will now test the method using a high-resolution Gaussian Network as the initial protein model. We will use a crystal structure of Adenylate Kinase (PDB: 4AKE [10]) as the model protein. The structure is shown in Fig. 5.4. This protein has a nice distribution of rigid and flexible domains, and it is also of an intermediate size with 214 residues and 1656 heavy atoms that makes it computationally inexpensive to work with. We only look at the heavy atoms in the protein.

### 5.4.1 Random Configuration Distributions

We start by randomly choosing 5000 different CG reductions, in which 90 percent of the particles are removed, and look at the distribution of the good bond fraction and the average ratio. Fig. 5.5 shows the results for the good bond fraction. The distribution is approximately Gaussian with a mean of 0.19 and a standard deviation of 0.01. Fig. 5.6 shows the results for the average ratio, where the mean is 0.35 and the standard deviation is 0.01. Fig. 5.7 compares the two metrics and shows that they are strongly anti-correlated with a correlation coefficient of  $-0.76$ .

Of course the metrics are not helpful if they cannot predict how well the CG networks perform at reproducing observables of the high resolution model. We will use the root mean square fluctuations (RMSF) for each particle as the observable that we compare. The RMSF for a particle is defined as

$$\text{RMSF}_i = \sqrt{\langle |\vec{r}_i - \vec{r}_{i,0}|^2 \rangle}, \quad (5.10)$$

where  $\vec{r}_i$  is the position of the  $i$ th particle, and  $\vec{r}_{i,0}$  is the initial position of the particle. Before calculating the deviation in position of particles from their initial positions,

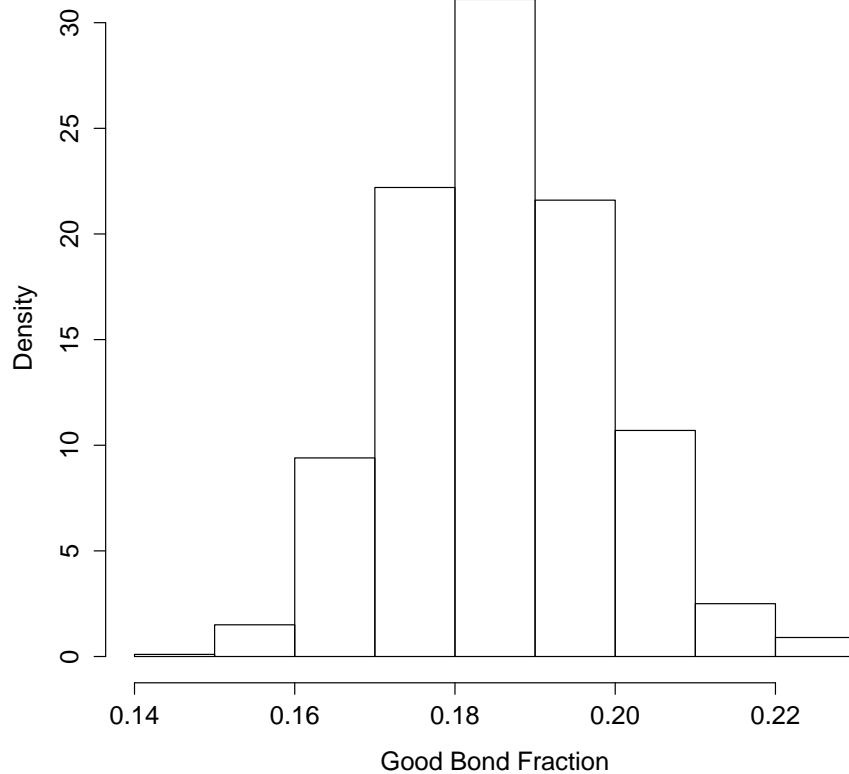


**Figure 5.5:** Distribution of the good bond fraction for CG networks of the Adenylate Kinase structure in which 90 percent of bonds have been removed. The mean value is 0.19 and the standard deviation is 0.01.

we first translate and rotate the system so that the total deviation of all the particles from the initial frame is minimized.

### 5.4.2 Defining the Spring Constant

To calculate the RMSF, we run a simulation using the EN network, and thus we now return to the question as to how we define the spring constant. Remember that in the ideal case, the spring constant is the only non-zero eigenvalue of the submatrix of the Hessian representing the interaction between two particles. We already mentioned taking the trace of the submatrix. In this case, we are adding the strength of the non-radial part to the radial interaction, even though these are supposed to be perpendicular. Another plausible option is to take the largest eigenvalue and ignore all the non-radial interactions between the two particles.

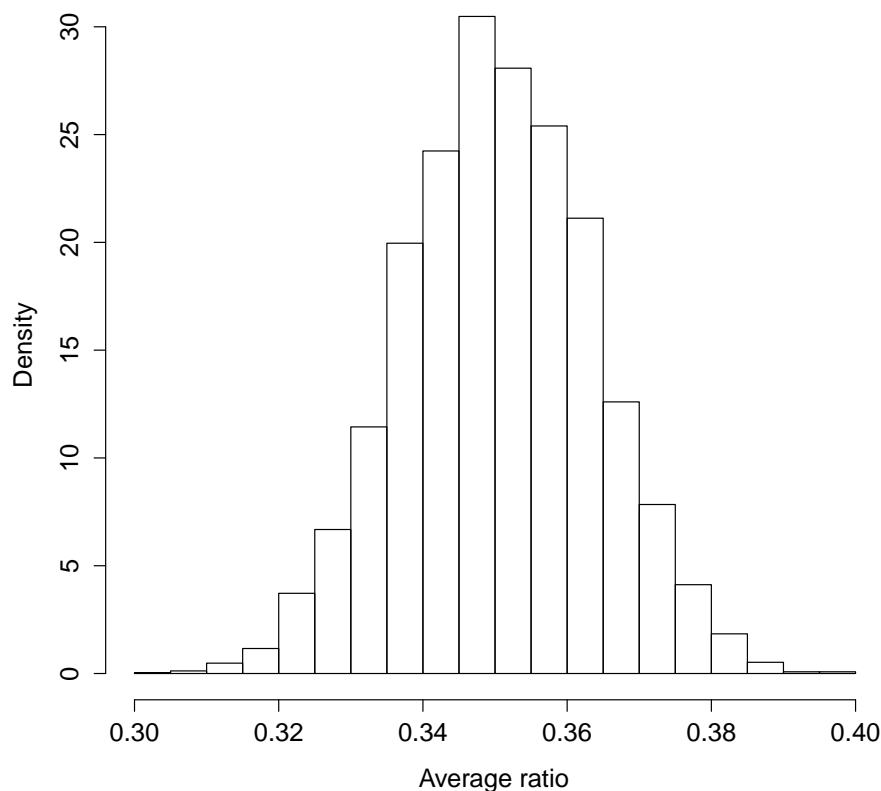


**Figure 5.6:** Distribution of the average ratio for CG networks of the Adenylate Kinase structure where 90 percent of bonds have been removed. The mean value is 0.35 and the standard deviation is 0.01.

Fig. 5.8 shows the RMSF for the same reduction with the spring constants defined as the largest eigenvalue and as the trace. The network that uses the trace for the interactions is able to reproduce the fluctuations of the all atom network better than the network using the largest eigenvalues. This is convenient, since it is easier to calculate the trace of each submatrix than to find the eigenvalues. Choosing the largest eigenvalue leads to overestimating the fluctuations which is caused by underestimating the strength of the interactions, which is not surprising considering that we ignored interactions. The best explanation for why the trace works better is that we are not ignoring any interactions, and though we are changing the direction of the non-radial interactions, this is balanced by changes in other interaction pairs. For the rest of the results shown, the simulations were performed with spring constants defined by the trace.

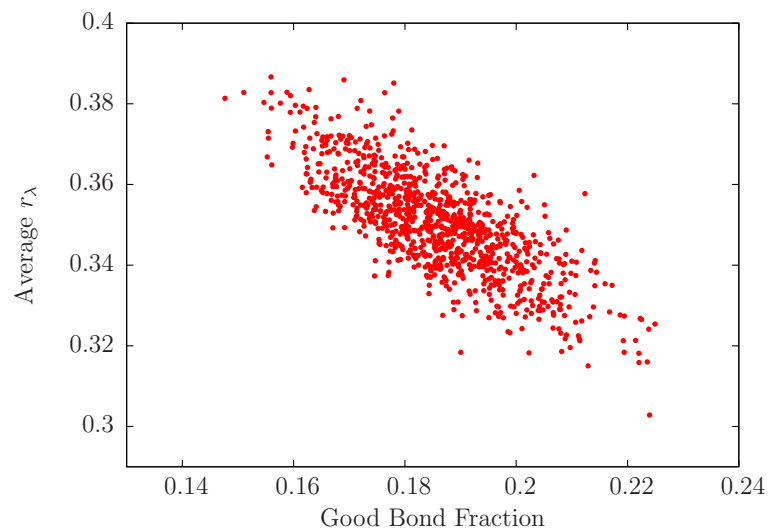


**Figure 5.7:** Scatter plot of the good bond fraction versus the average ratio for random reductions with 90 percent of particles removed. The correlation coefficient is  $-0.76$ .

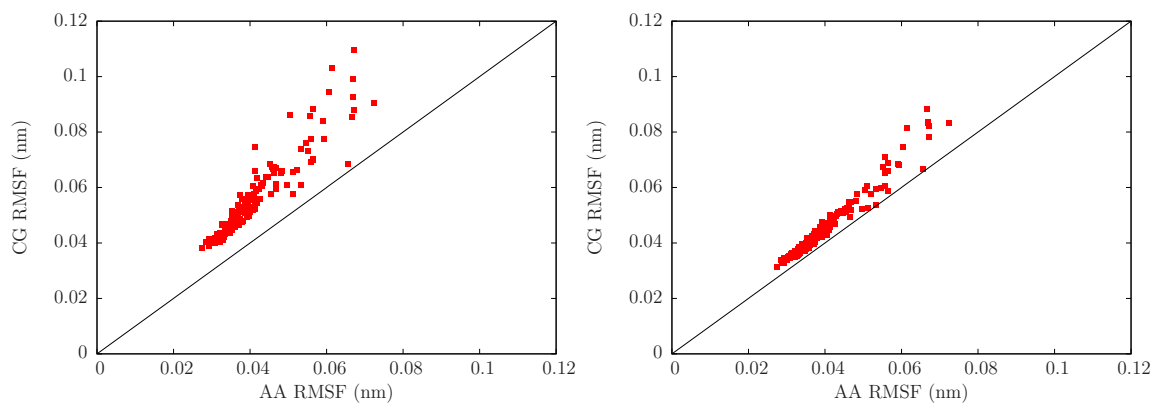


**Figure 5.8:** Comparison of RMSF for the particles of the CG network and the equivalent high resolution particles. The CG reduction had an average ratio of 0.3 and a good bond fraction of 0.21. Left: The largest eigenvalue of the interaction submatrix was used as the spring constant. Right: The trace of the interaction submatrix was used as the spring constant.

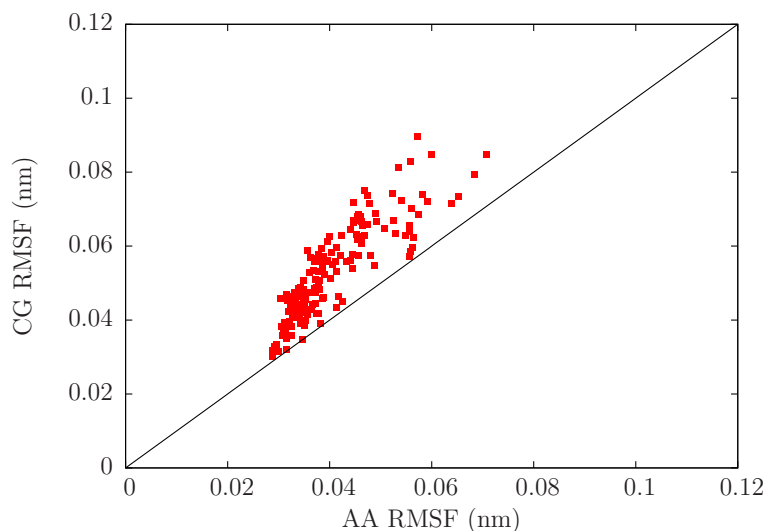


**Figure 5.9:** Comparison of RMSF for the particles of a CG network and the equivalent high resolution particles. This network has an average ratio of 0.4 and a good bond fraction of 0.09, which makes it one of the worse networks according to both metrics.

### 5.4.3 RMSF of Random Reductions

The network in Fig. 5.8 has an average ratio of 0.30 which makes it the reduction with the best average ratio from all the randomly sampled reductions. It also has a good bond fraction of 0.22 when a cutoff of 0.1 is used. We now compare this network to a network on the other end of the spectrum with an average ratio of 0.4 and a good bond fraction of 0.09. Fig. 5.9 shows this network performs worse at reproducing the fluctuations of the all atom network, especially for particles that had large fluctuations in the all atom model.

In general, we see that for reductions with a large average ratio or small good bond fraction, the CG fluctuations are too large compared to the high resolution simulation, and they perform worse for the particles that have large fluctuations in the high resolution simulation. As the metrics improve, the CG networks perform better at reproducing the fluctuations. The best networks at reproducing the fluctuations of the high-resolution model are the networks that score high with both metrics.

### 5.4.4 Single Particle per Amino Acid

We know that there is a distribution of quality of the CG reductions, and we would obviously like to use the best we can find. Of course, searching for the optimal reduction will take time, so it would be nice to find a simple rule that we can follow.

Traditionally, CG elastic networks have used the  $C_\alpha$  atoms of each amino acid as

Reduction	Good Bond Fraction	Average Ratio
Random Reductions	(0.21, 0.01)	(0.32, 0.01)
$C_\alpha$	0.21	0.32
$C_\beta$	0.21	0.32

**Table 5.1:** Good bond fraction and average ratio value for reductions with the same particle from each amino acid. The values for the random reductions is the mean value and standard deviation of the distribution (mean, sd).

the remaining degrees of freedom for a coarse-grained description [63, 64, 66, 72, 73, 151]. Fig. 5.10 shows the RMSF comparison for the CG network with only the  $C_\alpha$  from each amino acid remaining. This network has an average ratio of 0.32 and a good bond fraction of 0.21. Since this network has removed 88 percent instead of 90 percent of particles, the distributions for the average ratio and good bond fraction are slightly shifted compared to the reductions we have investigated so far: the mean value and standard deviation of the average ratio distribution are 0.32 and 0.01, respectively, and the mean value and standard deviation for the good bond fraction are 0.21 and 0.01, respectively. Thus the  $C_\alpha$  network is average for the number of particles removed according to these metrics. We also looked at using the other atoms that make up the backbone of an amino acid, but they all perform worse than the  $C_\alpha$  network.

The one atom selection that performs better than the  $C_\alpha$  comes from the side chain of the protein. Fig. 5.11 shows the RMSF results for a network with only the  $C_\beta$  particles from each amino acid. Even though this reduction also has an average ratio of 0.32 and a good bond fraction of 0.21, it reproduces the fluctuations of the high resolution model slightly better than the  $C_\alpha$  network. Our best explanation is that the  $C_\beta$  atoms are closer to the center of mass of the amino acid.

### 5.4.5 Optimized Reductions

We now focus on trying to efficiently find the best reductions. To this end, we have investigated two Monte Carlo based sampling routines to minimize the average ratio. We have found that minimizing the average ratio is numerically easier and more successful than maximizing the good bond fraction. Working with the good bond fraction increases the chance of getting stuck during the search. During each MC step, one particle in the CG network is swapped with a particle that had previously been removed. We used both simulated annealing [152, 153] and Wang-Landau sampling [154] with multiple different starting reductions. The simulations were run for 5000 steps so that we could compare their effectiveness to random sampling. Both simulated annealing and Wang-Landau perform only slightly better than random sampling. Fig. 5.12 shows the results for one of these optimized reductions. Even though there is only a slight improvement in terms of the average ratio, the reduc-

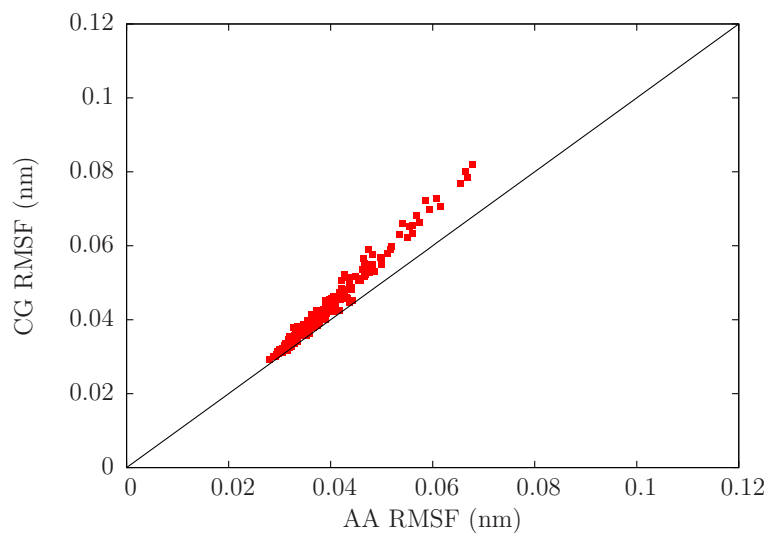


**Figure 5.10:** Comparison of RMSF for the particles of the CG network with all the  $C_{\alpha}$  and the equivalent high resolution particles.

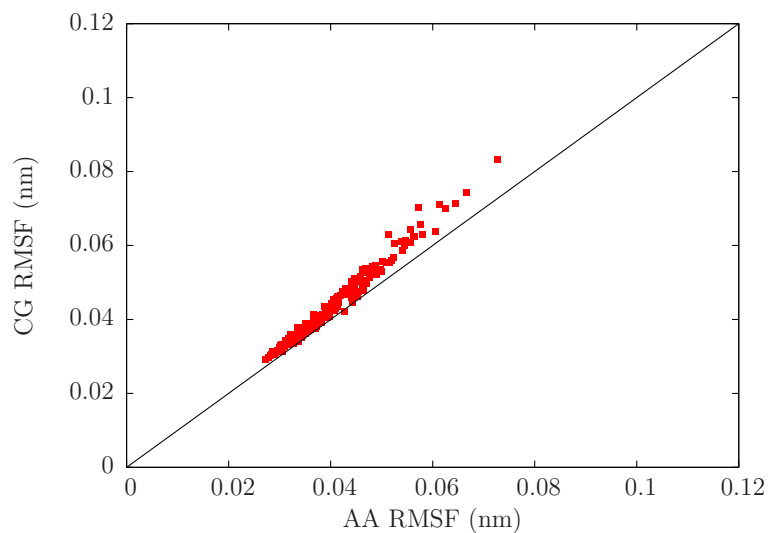


**Figure 5.11:** Comparison of RMSF for the particles of the CG network with all the  $C_{\beta}$  and the equivalent high resolution particles.

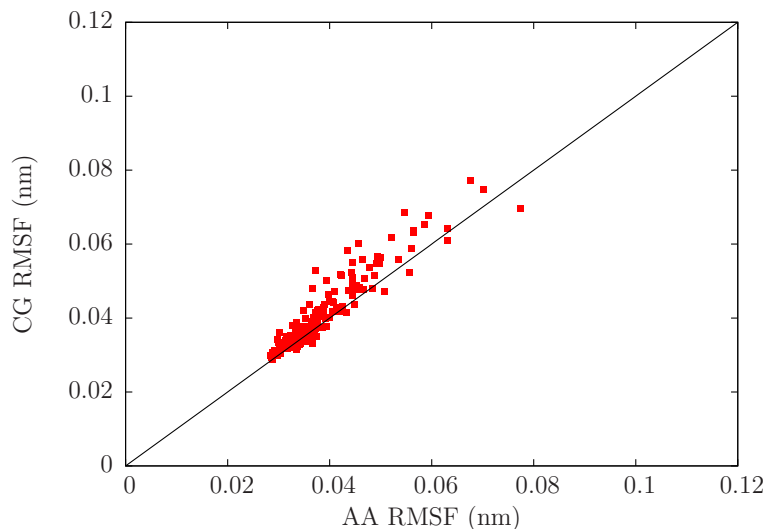


**Figure 5.12:** Comparison of RMSF for the particles of a CG network obtained from SA sampling.

tion reproduces the fluctuations of the high resolution simulation better than any other reduction we have looked at, including the  $C_\beta$  only reduction. It especially performs well for the atoms that undergo large fluctuations, which is where most of the reductions begin to fail.

### 5.4.6 Efficient MC Steps

Finding good reductions requires many MC steps, which hurts our goal of efficiency when these steps are costly. Normally, when we perform the coarse graining routine, the computational bottleneck is inverting the Hessian matrix of the particles that we want to remove. Luckily, we do not need to invert the entire matrix when we make an MC step because we can use information from the previous step. Since we are only replacing one particle, we are only changing three rows and three columns of the removed Hessian matrix  $\mathbf{H}_B$ , and so we are able to use information from the calculation of the inverse for the previous  $\mathbf{H}_B$  to quickly calculate the new inverse.

Our first step is to calculate the inverse matrix of the particles that are the same for both reductions. Let us call the group of particles that are being removed in both reductions  $S$  the previously removed particle that is now not removed  $O$  and the new particle to be removed  $N$ <sup>7</sup>. We will write the original sub-Hessian of removed particles  $\mathbf{H}_{B,0}$  as:

$$\mathbf{H}_{B,0} = \begin{pmatrix} \mathbf{H}_O & \mathbf{H}_{O,S} \\ \mathbf{H}_{O,S}^\dagger & \mathbf{H}_S \end{pmatrix}, \quad (5.11)$$

---

<sup>7</sup> $S$  for same,  $O$  for old, and  $N$  for new

where  $\mathbf{H}_{O,S}$  is the interaction matrix between particle  $O$  and the other particles. Our first goal is to find the inverse of  $\mathbf{H}_S$  because it will be useful later.

We partition the inverse of  $\mathbf{H}_B$  the same way:

$$\mathbf{H}_{B,0}^{-1} = \begin{pmatrix} \mathbf{M}_1 & \mathbf{M}_{1,2} \\ \mathbf{M}_{1,2}^\dagger & \mathbf{M}_2 \end{pmatrix}, \quad (5.12)$$

where  $\mathbf{M}_1$  has the same size and is in the same position in the inverse matrix as  $\mathbf{H}_O$  is in the original matrix.

The inverse of  $\mathbf{H}_S$  is

$$\mathbf{H}_S^{-1} = \mathbf{M}_2 - \mathbf{M}_{1,2}^\dagger \mathbf{M}_1^{-1} \mathbf{M}_{1,2}. \quad (5.13)$$

We call the new sub-Hessian of removed particles  $\mathbf{H}_{B,1}$ ,

$$\mathbf{H}_{B,1} = \begin{pmatrix} \mathbf{H}_N & \mathbf{H}_{N,S} \\ \mathbf{H}_{N,S}^\dagger & \mathbf{H}_S \end{pmatrix}, \quad (5.14)$$

where  $\mathbf{H}_N$  is the Hessian submatrix for the new particle to be removed.

To make the final result easier to read, we define  $\mathbf{N} = \mathbf{H}_N - \mathbf{H}_{N,S} \mathbf{H}_S^{-1} \mathbf{H}_{N,S}^\dagger$ . We then find that the inverse is:

$$\mathbf{H}_{B,1}^{-1} = \begin{pmatrix} \mathbf{N}^{-1} & -\mathbf{N}^{-1} \mathbf{H}_{N,S} \mathbf{H}_S^{-1} \\ -\mathbf{H}_S^{-1} \mathbf{H}_{N,S}^\dagger \mathbf{N}^{-1} & \mathbf{H}_S^{-1} + \mathbf{H}_S^{-1} \mathbf{H}_{N,S}^\dagger \mathbf{N}^{-1} \mathbf{H}_{N,S} \mathbf{H}_S^{-1} \end{pmatrix} \quad (5.15)$$

Thus, instead of having to take the inverse of a very large matrix, we need need to find the inverse of two  $3 \times 3$  matrices, and perform some additional matrix multiplication and addition. This reduces the time needed to create a new reduction by orders of magnitude.

The difference between the elements of the inverse matrix calculated using this method and from scratch is on the order of  $10^{-25}$  for the first 1000 steps. Over time, the numerical errors accumulate and eventually the total error begins to rapidly increase. This normally occurs after 2000 steps and necessitates that we calculate the inverse matrix directly after a set number of steps (normally 1000 steps to remain on the safe side).

Even though the Monte Carlo sampling methods have only shown a small improvement in finding good networks compared to random sampling (The reduction in Fig. 5.12 was found using the efficient MC step technique), the fact that we can perform the MC steps quickly allows us to sample hundreds of times more reductions in the same amount of time.

We now discuss why the attempts at finding an optimal reduction appears to be only slightly better than random sampling. Simulated annealing would often become stuck in a minimum whose average ratio were only three to four standard deviations from the mean of the distribution. If we raised the “temperature” again, the sample

would just fall into another well where the reductions were also only three standard deviations better than the mean. This would continue no matter how long we ran a simulated annealing simulation. The only difference between running the simulation for 5000 steps or 25000 steps was the number of different reductions of this type that would be found. Wang-Landau sampling has the same problem. The density of reductions that are more than three standard deviations away from the mean must be extremely small, difficult to find by our MC moves, or maybe it is simply zero.

## 5.5 Elastic Networks for RNA

We now apply the coarse graining method to an RNA example. Starting with the crystal structure of the Adenine riboswitch (PDB: 1Y26 [155]), we again produce an all atom elastic network that we then coarse grain. This riboswitch was chosen because it is of similar size as the Adenylate Kinase we used as the example for proteins, with 83 bases and 1499 heavy atoms. The structure is shown in Fig. 5.13.

We use an all atom elastic network with distance cutoff of 0.9 nm for the initial interactions. In this section, we follow the same order as for proteins where we start by looking at CG reductions chosen at random before moving to reductions consisting of the same particle for each nucleic acid.

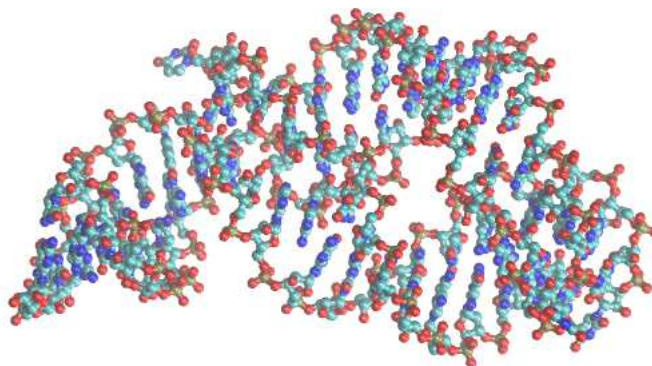


**Figure 5.13:** Image of crystal structure of the Adenine riboswitch.

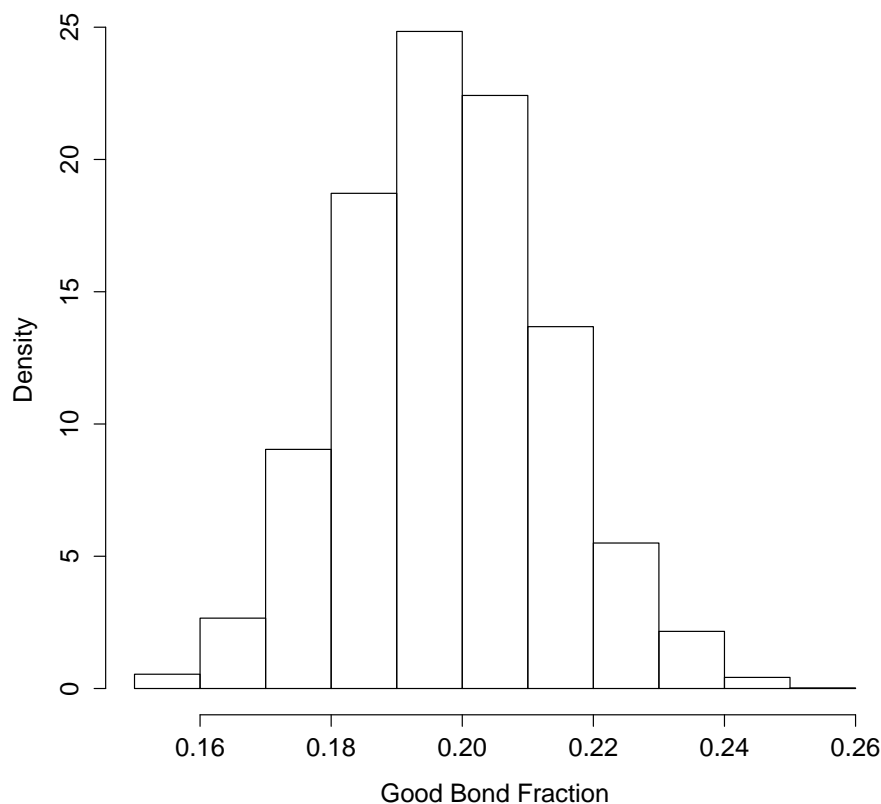


**Figure 5.14:** Distribution of the good bond fraction, where a good bond is defined as an interaction with an eigenvalue ratio below a cutoff of 0.1.

### 5.5.1 Random Configuration Distribution

As with the protein, we start our investigation by randomly choosing reductions where 90 percent of the particles are removed at random. Fig. 5.14 shows the results for the good bond fraction which again has a normal distribution. The cutoff value is 0.1. Fig. 5.15 shows the results for the average ratio. The two metrics have a correlation of -0.68, which is slightly weaker than for the protein model.

We now look at some reductions that fall at different ends of these distributions. Fig. 5.16 compares the RMSF for a configuration with an average ratio of 0.34 and a good bond fraction of 0.23. This makes it one of the best reductions according to its average ratio and an above average configuration according to its good bond fraction. Fig. 5.17 shows the RMSF comparison for a CG configuration with an average ratio of 0.36 and a good bond fraction of 0.25, making it above average according to its average ratio and one of the best reductions according to its good bond fraction. Both

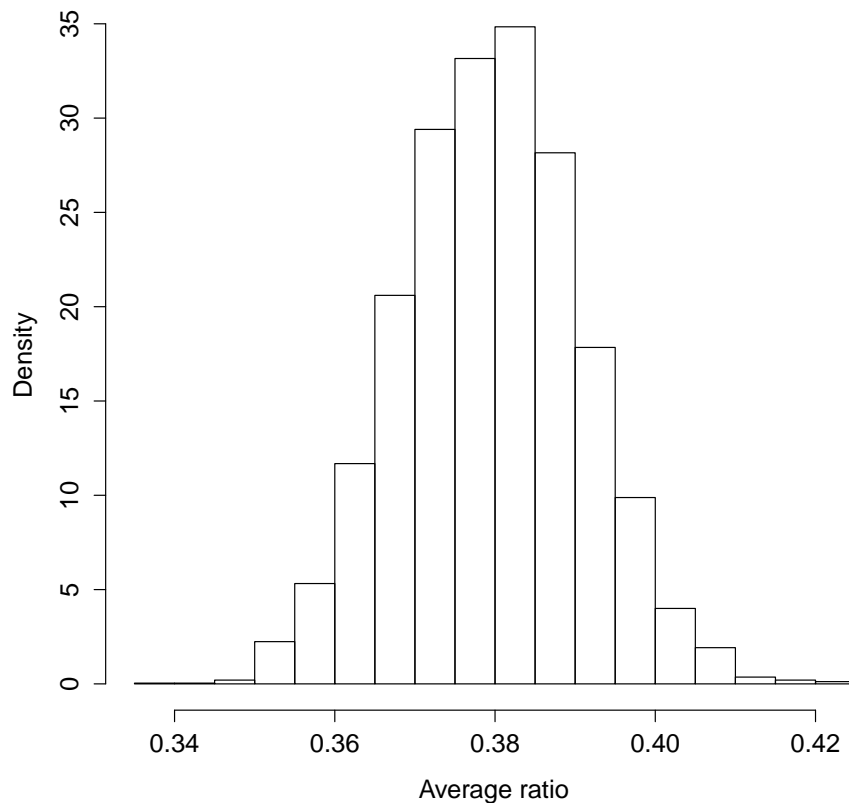


**Figure 5.15:** Distribution of the average ratio.

Reduction	Good Bond Fraction	Average Ratio
Random Reductions	(0.19, 0.02)	(0.37, 0.01)
5.16	0.23	0.34
5.17	0.25	0.36
5.18	0.18	0.40

**Table 5.2:** Good bond fraction and average ratio value for two good reductions and one bad reduction. The figure that shows the RMSF for the reduction is given in the table. The values for the random reductions are the mean value and standard deviation of the distribution (mean, standard deviation).

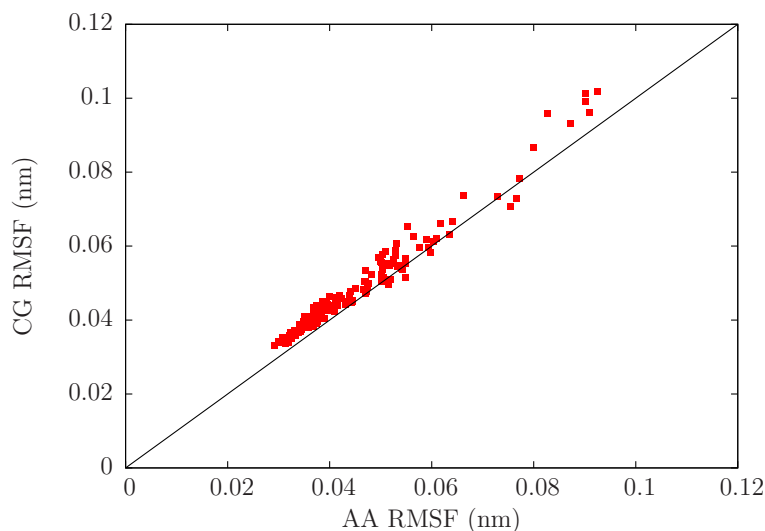


**Figure 5.16:** Comparison of the RMSF for a CG network and the equivalent particles of the all atom network. The CG network has an average ratio of 0.34 and a good bond fraction of 0.23. This makes it one of the best reductions according to its average ratio and an above average configuration according to its good bond fraction.

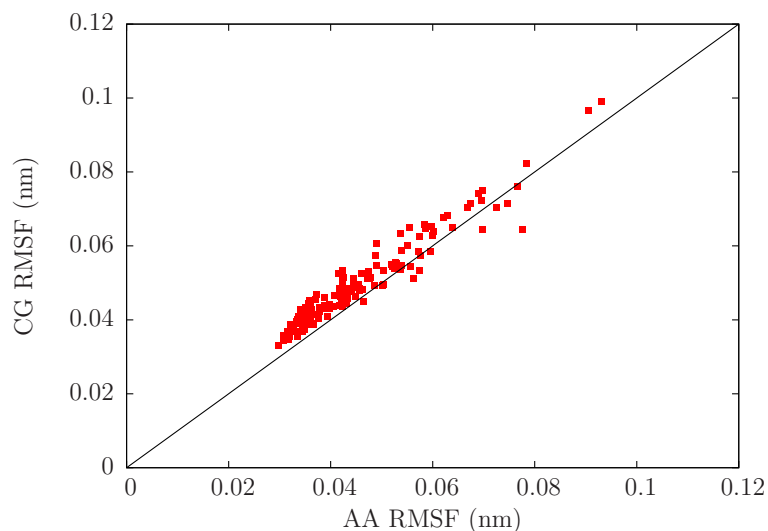
CG networks are able to reproduce the fluctuations of the high resolution model over all ranges of fluctuation magnitude. These results are better than the equivalent random reductions for the protein model.

Fig. 5.18 shows the RMSF for a configuration with an average ratio of 0.4 and a good bond fraction of 0.18, making it a poor configuration according to both metrics. The fluctuations of the network are consistently larger than for the high resolution model.

We tried to use the same advanced searching techniques to find a better CG network than what we could obtain randomly, but the best reductions that we found did not perform any better than the best random networks. This suggests that it is even more difficult to find the best reductions from the RNA distribution.

### 5.5.2 Single Particle per Nucleic Acid

We now turn our attention to networks that only have the same particle from each base. We will specifically look at networks with only the phosphorous atom, the C1' carbon atom, and the C2 carbon atom from the phosphate, sugar, and base parts of the nucleic acid respectively. Previous work by Pinamonti *et al.* [140] has looked at these three reductions using a Hessian network model, as opposed to the elastic network that we implement. They found that the C1' model performed the best at reproducing the fluctuations of all atom simulations. This was followed by the C2



**Figure 5.17:** Comparison of the RMSF for a CG network and the equivalent particles of the all atom network. The CG network has an average ratio of 0.36 and a good bond fraction of 0.25, making it above average according to its average ratio and one of the best reductions according to its good bond fraction.

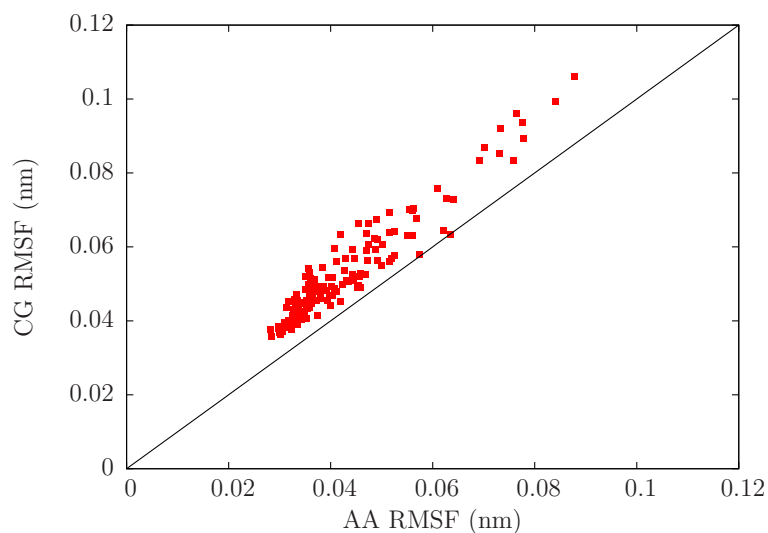


**Figure 5.18:** Comparison of the RMSF for a CG network and the equivalent particles of the all atom network. The CG network has an average ratio of 0.4 and a good bond fraction of 0.18 making it a poor configuration according to both metrics.

Reduction	Good Bond Fraction	Average Ratio
Random Reductions	(0.16, 0.02)	(0.42, 0.01)
P	0.24	0.39
C1'	0.18	0.42
C2	0.09	0.49

**Table 5.3:** Good bond fraction and average ratio value for reductions with the same particle from each nucleic acid. The values for the random reductions are the mean value and standard deviation of the distribution (mean, sd).

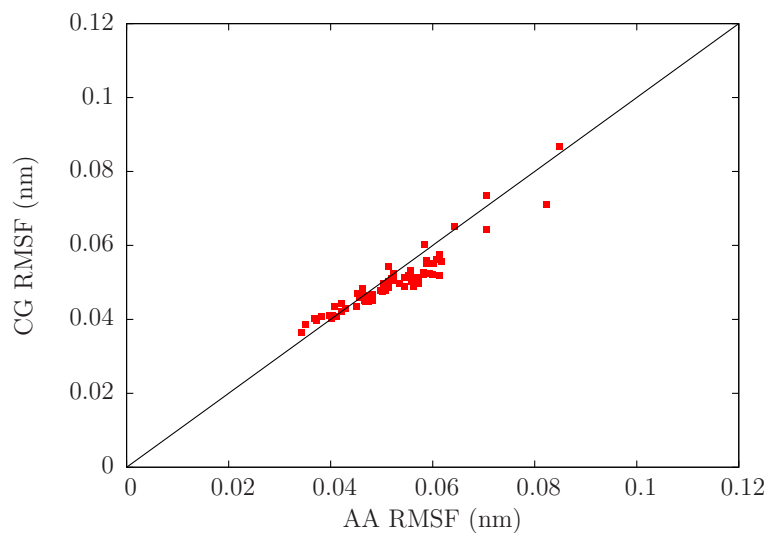
carbon and finally the phosphorus network.

Fig. 5.19, Fig. 5.20, and Fig. 5.21 show the RMSF for the phosphorous, C1' carbon and C2 carbon respectively. Our results do agree with Pinamonti *et al.* [140] in that the C1' network performs better than the C2 network, but the phosphorus network performs better than both with our method. The only difference between the two methods is that we convert the CG Hessian to an anisotropic elastic network, while Pinamonti *et al.* stay with a Hessian network. From this we can gather that the elements of the interactions that we lose when we create the C1' network are substantial, where as we don't lose as much for the phosphorus network.

Since these networks only have six percent of the particles remaining, we cannot compare average ratio or good bond fraction to the ten percent networks that we have looked at so far. The mean average ratio distribution for random networks with only 83 particles remaining is 0.42 with a standard deviation is 0.01 and the mean good bond fraction is 0.16 with a standard deviation of 0.02. The phosphorous network has an average ratio of 0.39 and a good bond fraction of 0.24 making it well above average for both of these metrics. The C1' network has an average ratio of 0.42 and a good bond fraction of 0.18 making it slightly above average. The C2 network has an average ratio of 0.49 and a good bond fraction of 0.09 making it one of the worst networks. This is consistent with the RMSF results.

These results are fundamentally different from the protein networks, where the better network was not on the backbone. For the protein model, we suggest that this was because the  $C_{\beta}$  particle is closer to the center of mass. For the RNA molecule, the phosphorous is on the backbone. In addition, all the protein single particle networks had average values for the average ratio and good bond fraction metric. Instead, the phosphorous RNA network is at the good tail end of the distribution.

Overall, the general principles of this CG elastic network technique are the same for the protein and RNA molecules, but we are unable to make universal claims about what makes a better network.



**Figure 5.19:** Comparison of the RMSF for the CG network with only the phosphorous atoms and the equivalent particles of the all atom network. The CG network has an average ratio of 0.39 and a good bond fraction of 0.24.

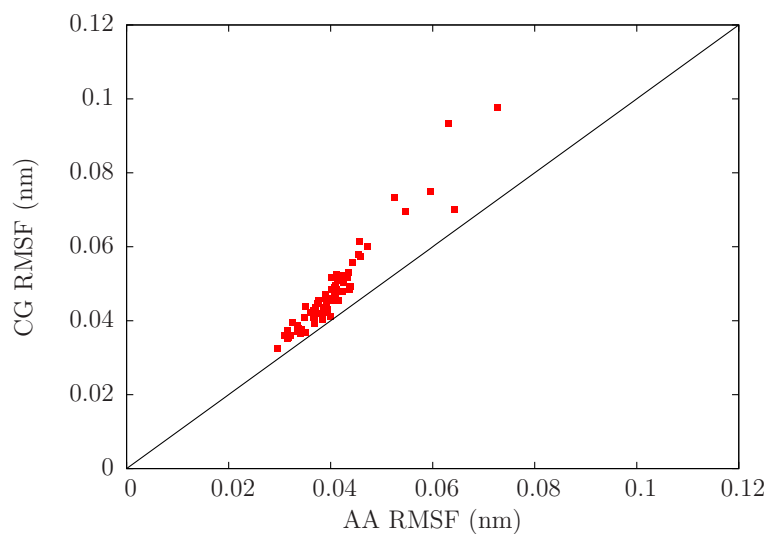


**Figure 5.20:** Comparison of the RMSF for the CG network with only the C1' carbon atoms and the equivalent particles of the all atom network. The CG network has an average ratio of 0.42 and a good bond fraction of 0.18.

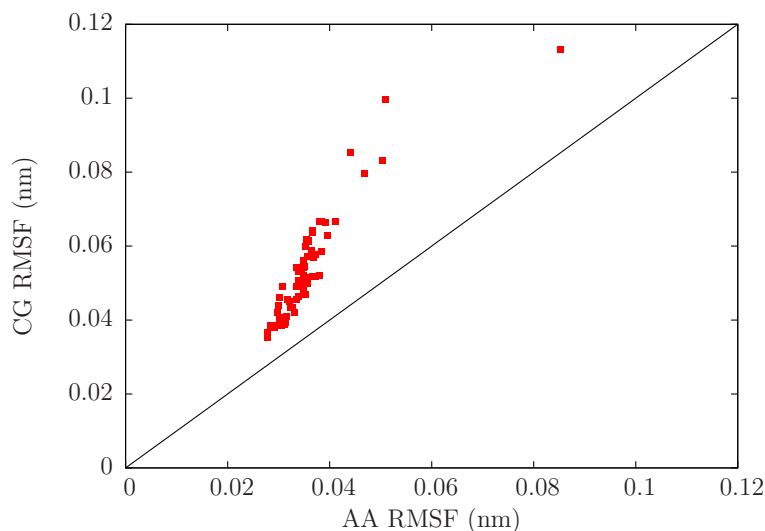


**Figure 5.21:** Comparison of the RMSF for the CG network with only the C2 carbon atoms and the equivalent particles of the all atom network. The CG network has an average ratio of 0.49 and a good bond fraction of 0.09 .

## 5.6 Discussion

We can efficiently create CG Gaussian networks by partially integrating the partition function of the quadratic Taylor expansion of a high resolution model. Unfortunately, we cannot exactly transfer the coarse grained Hessian to an anisotropic elastic network that can be used in Molecular Dynamic simulations, and we are forced to make an approximation of the CG Hessian. The choice of which particles to remove has a large effect on the ability of the CG anisotropic network to reproduce the fluctuations of the high resolution model. For the protein example we discuss, the standard choice of keeping every  $C_\alpha$  works reasonably well, but it is only an average reduction, and therefore there are reductions that perform better. For instance, picking the  $C_\beta$  atoms for a protein configuration over the  $C_\alpha$ , or performing a search over all reductions and finding an even better set of heavy atoms to represent the molecule. For the RNA molecule, the best CG networks perform exceptionally well at reproducing the fluctuations, and we were unable to find better reductions using advanced sampling techniques.

There are two main areas of improvement for this method. Though the advanced sampling techniques that we tried did not find reductions at the tail of the distributions, there may be better methods, or there may be a different metric that is easier to search. The second area of improvement is in determining what makes a good reduction. At the moment, the potential lessons from one bio-molecular structure seem to be contradicted by the lessons from another structure. Are there universal guidelines for selecting a good reduction? Regardless, this method already can produce

elastic networks that can to a good job of reproducing the fluctuations of atomistic models without the need for an atomistic reference model, and there is still room for improvement.

# Mathematical Symbols

This section provides a table of the important symbols used in this thesis. The symbols are ordered by when they appear in the thesis. Not all symbols in the thesis are listed. Many symbols that are only used briefly have been omitted.

<b>Symbol</b>	<b>Description</b>
$\mathcal{E}$	Energy of a membrane
$S$	The surface of a membrane
$c_i$	Principle curvature of a surface
$K$	The total curvature ( $K = c_1 + c_2$ )
$K_0$	The spontaneous curvature
$K_G$	The Gaussian curvature ( $K_G = c_1 c_2$ )
$\kappa$	The bending modulus
$\bar{\kappa}$	The Gaussian curvature
$\vec{r}$	The positional degrees of freedom for a system
$\vec{r}_0$	The equilibrium position of the particles in a system
$r_i^\mu$	The $\mu$ component of the position of particle $i$
$\delta r_i^\mu$	The difference in the $\mu$ component of the position of particle $i$ from its equilibrium position
$d_{i,j}$	The distance between two particles
$d_{i,j}^0$	The equilibrium distance between two particles
$d_{i,j}^\mu$	The difference in the $\mu$ component of the position between two particles
$h_q$	The undulation mode of wave vector $q$
$\tau_r$	The relaxation time
$L$	The length of a membrane
$F_z$	The force on a membrane tether
$R_t$	The radius of a membrane tether
$L_x, L_y, L_z$	The dimensions of the simulation box
$\gamma$	The buckling strain ( $\gamma = (L - L_x)/L$ )
$\phi$	The angle that the membrane makes against the horizontal axis
$f_x$	The lateral compressive stress along the $x$ -direction
$\Sigma$	The isotropic surface tension
$\lambda$	The ratio of the bending modulus to the lateral compressive stress
$m$	The elliptic parameter
$\psi_i$	The angle at the inflection point
$\sigma$	Unit of length for Cooke simulations
$\epsilon$	Unit of energy for Cooke simulations

$E_{\text{pot}}$	The potential energy of a simulation
$\mathcal{R}$	The ratio of the potential energy and free energy of a membrane
$\ell$	Length material parameter that determines the extent that the membrane deviates from Helfrich theory
$\tilde{f}_x$	The squared ratio of $\ell$ and $\lambda$ ( $\ell^2/\lambda^2$ )
$\delta$	Dimensionless parameter relating $\ell$ to the length of the membrane $L$
$w$	The thickness of a bilayer
$L_t$	The length of a tethered membrane
$\mathbb{H}$	The Hessian matrix for a system
$Z$	The canonical partition function
$r_\lambda$	The ratio of the second largest to the largest eigenvalue
$f_g$	The fraction of acceptable bonds for a reduction
$f_a$	The average ratio for a reduction

# Bibliography

- [1] W. Helfrich, “Elastic properties of lipid bilayers: theory and possible experiments,” *Naturforsch. C*, vol. 28, pp. 693–703, 1973.
- [2] R. Phillips, J. Kondev, and J. Theriot, *Physical Biology of the Cell*. Garland Science, 2009.
- [3] J. F. Nagle, “Introductory Lecture: Basic quantities in model biomembranes,” *Farad. Discuss.*, vol. 161, pp. 11–29, 2013.
- [4] H. Lodish, A. Berk, C. A. Kaiser, M. Krieger, M. P. Scott, A. Bretscher, H. Ploegh, and P. Matsudaira, *Molecular Cell Biology*. W. H. Freeman and Company, sixth ed., 2008.
- [5] B. Alberts, A. Johnson, and J. Lewis, *Molecular Biology of the Cell*. Garland Science, fifth ed., 2008.
- [6] A. Roux, K. Uyhazi, A. Frost, and P. De Camilli, “Gtp-dependent twisting of dynamin implicates constriction and tension in membrane fission,” *Nature*, vol. 441, pp. 528–531, 2006.
- [7] M. J. Bowick and R. Sknepnek, “Pathways to faceting of vesicles,” *Soft Matter*, vol. 9, pp. 8088–8095, 2013.
- [8] S. Nagarajan, E. E. Schuler, K. Ma, J. T. Kindt, and R. B. Dyer, “Dynamics of the Gel to Fluid Phase Transformation in Unilamellar DPPC Vesicles,” *J. Phys. Chem. B*, vol. 116, pp. 13749–13756, 2012.
- [9] C. Coulais, J. T. B. Overvelde, L. A. Lubbers, K. Bertoldi, and M. van Hecke, “Discontinuous Buckling of Wide Beams and Metabeams,” *Phys. Rev. Lett.*, vol. 115, p. 044301, Jul 2015.
- [10] C. W. Müller, G. J. Schlauderer, J. Reinstein, and G. E. Schulz, “Adenylate kinase motions during catalysis: an energetic counterweight balancing substrate binding,” *Structure*, vol. 4, pp. 147–56, 1996.

- [11] R. Potestio, F. Pontiggia, and C. Micheletti, “Coarse-grained description of protein internal dynamics: An optimal strategy for decomposing proteins in rigid subunits,” *Biophys. J.*, vol. 96, pp. 4993–5002, 2009.
- [12] R. Lipowsky and E. Sackmann, eds., *Structure and Dynamics of Membranes*, vol. 1A of *Handbook of Biological Physics*. Elsevier, North Holland, 1995.
- [13] Avanti Polar Lipids, “14:0 PC (DMPC)—850345,” 2015. [Online: accessed March 15, 2015].
- [14] J. N. Israelachvili, D. J. Mitchell, and B. W. Ninham, “Theory of self-assembly of hydrocarbon amphiphiles into micelles and bilayers,” *J. Chem. Soc., Faraday Trans.*, vol. 72, pp. 1525–1568, 1976.
- [15] I. R. Cooke and M. Deserno, “Coupling between Lipid Shape and Membrane Curvature,” *Biophys. J.*, vol. 91, pp. 487–495, 2006.
- [16] E. Kreyszig, *Differential Geometry*. New York: Dover, 1991.
- [17] M. do Carmo, *Differential Geometry of Curves and Surfaces*. Englewood Cliffs, NJ: Prentice Hall, 1976.
- [18] M. Hamm and M. M. Kozlov, “Elastic energy of tilt and bending of fluid membranes,” *Eur. Phys. J. E*, vol. 3, no. 4, pp. 323–335, 2000.
- [19] M. C. Watson, E. G. Brandt, P. M. Welch, and F. L. H. Brown, “Determining Biomembrane Bending Rigidities from Simulations of Modest Size,” *Phys. Rev. Lett.*, vol. 109, p. 028102, Jul 2012.
- [20] J. F. Nagle, M. S. Jablin, S. Tristram-Nagle, and K. Akabori, “What are the true values of the bending modulus of simple lipid bilayers?,” *Chem. Phys. Lipids*, vol. 185, pp. 3–10, 2015.
- [21] D. Chapman, R. M. Williams, and B. D. Ladbroke, “Physical studies of phospholipids. VI. Thermotropic and lyotropic mesomorphism of some 1,2-diacylphosphatidylcholines (lecithins),” *Chem. Phys. Lipids*, vol. 1, pp. 445–475, 1967.
- [22] E. Evans and R. Kwok, “Mechanical calorimetry of large dimyristoylphosphatidylcholine vesicles in the phase transition region,” *Biochemistry*, vol. 21, no. 20, pp. 4874–4879, 1982.
- [23] T. Heimburg, U. Würz, and D. Marsh, “Binary phase diagram of hydrated dimyristoylglycerol-dimyristoylphosphatidylcholine mixtures,” *Biophys. J.*, vol. 63, no. 5, pp. 1369–1378, 1992.
- [24] J. F. Nagle and S. Tristram-Nagle, “Structure of lipid bilayers,” *BBA-Biomembranes*, vol. 1469, pp. 159–195, 2000.

- [25] R. H. Garrett and C. M. Grisham, *Biochemistry*. Brooks Cole, fourth ed., 2008.
- [26] T. E. Creighton, *Proteins: Structures and molecular properties*. W. H. Freeman, second ed., 1992.
- [27] A. Fersht, *Structure and mechanism in protein science: A guide to enzyme catalysis and protein folding*. W. H. Freeman, first ed., 1998.
- [28] W. M. Haynes, ed., *CRC handbook of chemistry and physics*. CRC Press, 96 ed., 2015.
- [29] C. N. Pace, “Conformational stability of globular proteins,” *Trends Biochem. Sci.*, vol. 15, pp. 14–17, 1990.
- [30] C. N. Pace, B. A. Shirley, M. McNutt, and K. Gajiwala, “Forces contributing to the conformational stability of proteins,” *FASEB J.*, vol. 10, pp. 75–83, 1996.
- [31] Wikipedia, the free encyclopedia, “RNA chemical structure,” 2015. [Online; accessed March 15, 2015].
- [32] I. Tinono Jr. and C. Bustamante, “How RNA folds,” *J. Mol. Biol.*, vol. 293, pp. 271–281, 1999.
- [33] W. F. van Gunsteren and H. J. C. Berendsen, “Computer Simulation of Molecular Dynamics: Methodology, Applications, and Perspectives in Chemistry,” *Angewandte Chemie International Edition in English*, vol. 29, pp. 992–1023, 1990.
- [34] M. Karplus and J. A. McCammon, “Molecular dynamics simulations of biomolecules,” *Nat. Struct. Mol. Biol.*, vol. 9, pp. 646–652, 2002.
- [35] M. P. Allen and D. J. Tildesley, *Computer simulation of liquids*. Clarendon Pr., 1993.
- [36] D. Frenkel and B. Smit, *Understanding molecular simulation: From algorithms to applications*. Academic Press, 2nd ed., 2001.
- [37] K. Petersen, *Ergodic theory*. Cambridge University Press, 1983.
- [38] O. Berger, O. Edholm, and F. Jähnig, “Molecular dynamics simulations of a fluid bilayer of dipalmitoylphosphatidylcholine at full hydration, constant pressure, and constant temperature,” *Biophys. J.*, vol. 72, no. 5, pp. 2002–2013, 1997.
- [39] S. J. Marrink, X. Periole, D. P. Tieleman, and A. H. d. Vries, “Comment on “On using a too large integration time step in molecular dynamics simulations of coarse-grained molecular models” by M. Winger, D. Trzesniak, R. Baron and W. F. van Gunsteren, *Phys. Chem. Chem. Phys.*, 2009, 11, 1934,” *Phys. Chem. Chem. Phys.*, vol. 12, pp. 2254–2256, 2010.

- [40] V. Tozzini, “Coarse-grained models for proteins,” *Curr. Opin. Struct. Biol.*, vol. 15, pp. 144–150, 2005.
- [41] D. Fritz, C. R. Herbers, K. Kremer, and N. F. A. van der Vegt, “Hierarchical modeling of polymer permeation,” *Soft Matter*, vol. 5, p. 4556, 2009.
- [42] M. Deserno, “Mesoscopic Membrane Physics: Concepts, Simulations, and Selected Applications,” *Macromol. Rapid Comm.*, vol. 30, pp. 752–771, 2009.
- [43] W. G. Noid, “Perspective: Coarse-grained models for biomolecular systems,” *J. Chem. Phys.*, vol. 139, p. 090901, 2013.
- [44] S. Riniker, J. R. Allison, and W. F. van Gunsteren, “On developing coarse-grained models for biomolecular simulation: a review,” *Phys. Chem. Chem. Phys.*, vol. 14, pp. 12423–12430, 2012.
- [45] W. Tschöp, K. Kremer, J. Batoulis, T. Bürger, and O. Hahn, “Simulation of polymer melts. I. Coarse-graining procedure for polycarbonates,” *Acta Polym.*, vol. 49, pp. 61–74, 1998.
- [46] A. K. Soper, “Empirical potential Monte Carlo simulation of fluid structure,” *Chem. Phys.*, vol. 202, pp. 295–306, 1996.
- [47] A. P. Lyubartsev and A. Laaksonen, “Calculation of effective interaction potentials from radial distribution functions: A reverse Monte Carlo approach,” *Phys. Rev. E*, vol. 52, p. 3730, 1995.
- [48] S. Izvekov and G. A. Voth, “A Multiscale Coarse-Graining Method for Biomolecular Systems,” *J. Phys. Chem. B*, vol. 109, pp. 2469–2473, 2005.
- [49] S. Izvekov and G. A. Voth, “Multiscale coarse graining of liquid-state systems,” *J. Chem. Phys.*, vol. 123, p. 134105, 2005.
- [50] A. A. Louis, “Beware of density dependent pair potentials,” *J. Phys. Condens. Matter*, vol. 14, p. 9187, 2002.
- [51] M. E. Johnson, T. Head-Gordon, and A. A. Louis, “Representability problems for coarse-grained water potentials,” *J. Chem. Phys.*, vol. 126, p. 144509, 2007.
- [52] H. Wang, C. Junghans, and K. Kremer, “Comparative atomistic and coarse-grained study of water: What do we lose by coarse-graining?,” *Eur. Phys. J. E*, vol. 28, pp. 221–229, 2009.
- [53] J. W. Mullinax and W. G. Noid, “Extended ensemble approach for deriving transferable coarse-grained potentials,” *J. Chem. Phys.*, vol. 131, p. 104110, 2009.

- [54] I. R. Cooke, K. Kremer, and M. Deserno, “Tunable generic model for fluid bilayer membranes,” *Phys. Rev. E*, vol. 72, no. 1, p. 011506, 2005.
- [55] I. R. Cooke and M. Deserno, “Solvent-free model for self-assembling fluid bilayer membranes: Stabilization of the fluid phase based on broad attractive tail potentials,” *J. Chem. Phys.*, vol. 123, no. 22, p. 224710, 2005.
- [56] J. D. Weeks, D. Chandler, and H. C. Andersen, “Role of Repulsive Forces in Determining the Equilibrium Structure of Simple Liquids,” *J. Chem. Phys.*, vol. 15, p. 5237, 1971.
- [57] S. J. Marrink, H. J. Risselada, S. Yefimov, D. P. Tieleman, and A. H. de Vries, “The MARTINI Force Field: Coarse Grained Model for Biomolecular Simulations,” *J. Phys. Chem. B*, vol. 111, pp. 7812–7824, 2007.
- [58] S. J. Marrink and D. P. Tieleman, “Perspective on the MARTINI model,” *Chem. Soc. Rev.*, vol. 42, pp. 6801–6822, 2013.
- [59] J. M. Rodgers, J. Sørensen, J. M. de Meyer, Frédérick, B. Schiøtt, and B. Smit, “Understanding the Phase Behavior of Coarse-Grained Model Lipid Bilayers through Computational Calorimetry,” *J. Phys. Chem. B*, vol. 116, pp. 1551–1569, 2012.
- [60] Z.-J. Wang and M. Deserno, “A Systematically Coarse-Grained Solvent-Free Model for Quantitative Phospholipid Bilayer Simulation,” *J. Phys. Chem. B*, vol. 114, no. 34, pp. 11207–11220, 2010.
- [61] Z.-J. Wang and M. Deserno, “Systematic implicit solvent coarse-graining of bilayer membranes: lipid and phase transferability of the force field,” *New J. Phys.*, vol. 12, p. 095004, 2010.
- [62] M. M. Tirion, “Large Amplitude Elastic Motions in Proteins from a Single-Parameter Atomic Analysis,” *Phys. Rev. Lett.*, vol. 77, pp. 1905–1908, 1996.
- [63] I. Bahar, A. R. Atilgan, and B. Erman, “Direct evaluation of thermal fluctuations in proteins using a single-parameter harmonic potential,” *Fold. Des.*, vol. 2, pp. 173–181, 1997.
- [64] T. Haliloglu, I. Bahar, and B. Erman, “Gaussian Dynamics of Folded Proteins,” *Phys. Rev. Lett.*, vol. 79, pp. 3090–3093, 1997.
- [65] T. Haliloglu and I. Bahar, “Structure-based analysis of protein dynamics: Comparison of theoretical results for hen lysozyme with X-ray diffraction and NMR relaxation data,” *Proteins*, vol. 37, pp. 654–667, 1999.
- [66] K. Hinsen, A. Petrescu, S. Dellerue, M. Bellissent-Funel, and G. Kneller, “Harmonicity in slow protein dynamics,” *Chem. Phys.*, vol. 261, pp. 25–37, 2000.

- [67] A. R. Atilgan, S. R. Durell, R. L. Jernigan, M. C. Demirel, O. Keskin, and I. Bahar, “Anisotropy of Fluctuation Dynamics of Proteins with an Elastic Network Model,” *Biophys. J.*, vol. 80, pp. 505–515, 2001.
- [68] I. Bahar and A. J. Rader, “Coarse-grained normal mode analysis in structural biology,” *Curr. Opin. Struct. Biol.*, vol. 15, pp. 586–592, 2005.
- [69] V. Carnevale, S. Raugei, C. Micheletti, and P. Carloni, “Convergent Dynamics in the Protease Enzymatic Superfamily,” *J. Am. Chem. Soc.*, vol. 2, pp. 173–181, 2006.
- [70] A. Zen, V. Carnevale, A. M. Lesk, and C. Micheletti, “Correspondences between low-energy modes in enzymes: Dynamics-based alignment of enzymatic functional families,” *Protein Sci.*, vol. 17, pp. 918–929, 2008.
- [71] E. Lyman, J. Pfaendtner, and G. A. Voth, “Systematic Multiscale Parameterization of Heterogeneous Elastic Network Models of Proteins,” *Biophys. J.*, vol. 95, pp. 4183–4192, 2008.
- [72] L. Zhou and S. A. Siegelbaum, “Effects of Surface Water on Protein Dynamics Studied by a Novel Coarse-Grained Normal Mode Approach,” *Biophys. J.*, vol. 94, pp. 3461–3474, 2008.
- [73] L. Yang, G. Song, and R. L. Jernigan, “Protein elastic network models and the ranges of cooperativity,” *Proc. Natl. Acad. Sci. USA*, vol. 106, pp. 12347–12352, 2009.
- [74] E. Fuglebakk, N. Reuter, and K. Hinsen, “Evaluation of Protein Elastic Network Models Based on an Analysis of Collective Motions,” *J. Chem. Theory Comput.*, vol. 9, pp. 5618–5628, 2013.
- [75] S. Kundu, J. S. Melton, D. C. Sorensen, and G. N. Phillips Jr, “Dynamics of Proteins in Crystals: Comparison of Experiment with Simple Models,” *Biophys. J.*, vol. 83, pp. 723–732, 2002.
- [76] M. Deserno, “Fluid lipid membranes: from differential geometry to curvature stresses,” *Chem. Phys. Lipids*, vol. 185, pp. 11–45, 2015.
- [77] U. Seifert, “Configurations of fluid membranes and vesicles,” *Adv. Phys.*, vol. 46, pp. 13–137, 1997.
- [78] H. Wang, D. Hu, and P. Zhang, “Measuring the spontaneous curvature of bilayer membranes by molecular dynamics simulations,” *Comm. Comp. Phys.*, vol. 13, pp. 1093–1106, 2012.

- [79] M. Hu, J. J. Briguglio, and M. Deserno, “Determining the Gaussian Curvature Modulus of Lipid Membranes in Simulations,” *Biophys. J.*, vol. 102, no. 6, pp. 1403–1410, 2012.
- [80] M. Hu, D. H. de Jong, S.-J. Marrink, and M. Deserno, “Gaussian curvature elasticity determined from global shape transformations and local stress distributions: A comparative study using the MARTINI model,” *Farad. Discuss.*, vol. 161, pp. 365–382, 2013.
- [81] R. Goetz, G. Gompper, and R. Lipowsky, “Mobility and elasticity of self-assembled membranes,” *Phys. Rev. Lett.*, vol. 82, pp. 221–224, 1999.
- [82] E. Lindahl and O. Edholm, “Mesoscopic undulations and thickness fluctuations in lipid bilayers from molecular dynamics simulations,” *Biophys. J.*, vol. 79, no. 1, pp. 426–433, 2000.
- [83] S. J. Marrink and A. E. Mark, “Effect of Undulations on Surface Tension in Simulated Bilayers,” *J. Phys. Chem. B*, vol. 105, no. 26, pp. 6122–6127, 2001.
- [84] G. Ayton and G. A. Voth, “Bridging microscopic and mesoscopic simulations of lipid bilayers,” *Biophys. J.*, vol. 83, no. 6, pp. 3357–3370, 2002.
- [85] O. Farago, ““water-free” computer model for fluid bilayer membranes,” *J. Chem. Phys.*, vol. 119, no. 1, pp. 596–605, 2003.
- [86] S. J. Marrink, A. H. de Vries, and A. E. Mark, “Coarse grained model for semiquantitative lipid simulations,” *J. Phys. Chem. B*, vol. 108, no. 2, pp. 750–760, 2004.
- [87] Z.-J. Wang and D. Frenkel, “Modeling flexible amphiphilic bilayers: A solvent-free off-lattice Monte Carlo study,” *J. Chem. Phys.*, vol. 122, no. 23, p. 154701, 2005.
- [88] G. Brannigan, P. F. Philips, and F. L. H. Brown, “Flexible lipid bilayers in implicit solvent,” *Phys. Rev. E*, vol. 72, no. 1, p. 011915, 2005.
- [89] E. R. May, A. Narang, and D. I. Kopelevich, “Role of molecular tilt in thermal fluctuations of lipid membranes,” *Phys. Rev. E*, vol. 76, p. 021913, Aug 2007.
- [90] E. R. May, A. Narang, and D. I. Kopelevich, “Molecular modeling of key elastic properties for inhomogeneous lipid bilayers,” *Mol. Sim.*, vol. 33, no. 9-10, pp. 787–797, 2007.
- [91] M. C. Watson, E. S. Penev, P. M. Welch, and F. L. H. Brown, “Thermal fluctuations in shape, thickness, and molecular orientation in lipid bilayers,” *J. Chem. Phys.*, vol. 135, no. 24, p. 244701, 2011.

- [92] E. G. Brandt, A. R. Braun, J. N. Sachs, J. F. Nagle, and O. Edholm, “Interpretation of Fluctuation Spectra in Lipid Bilayer Simulations,” *Biophys. J.*, vol. 100, no. 9, pp. 2104–2111, 2011.
- [93] H. Shiba and H. Noguchi, “Estimation of the bending rigidity and spontaneous curvature of fluid membranes in simulations,” *Phys. Rev. E*, vol. 84, p. 031926, 2011.
- [94] F. Brochard and J. F. Lennon, “Frequency Spectrum of Flicker Phenomenon in Erythrocytes,” *J. de Physique*, vol. 36, no. 11, pp. 1035–1047, 1975.
- [95] F. Brochard, P.-G. de Gennes, and P. Pfeuty, “Surface-tension and deformations of membrane structures—relation to 2-dimensional phase-transitions,” *J. de Physique*, vol. 37, no. 10, pp. 1099–1104, 1976.
- [96] M. B. Schneider, J. T. Jenkins, and W. W. Webb, “Thermal Fluctuations of Large Cylindrical Phospholipid-Vesicles,” *Biophys. J.*, vol. 45, no. 5, pp. 891–899, 1984.
- [97] M. B. Schneider, J. T. Jenkins, and W. W. Webb, “Thermal Fluctuations of Large Quasi-Spherical Bimolecular Phospholipid-Vesicles,” *Biophys. J.*, vol. 45, no. 9, pp. 1457–1472, 1984.
- [98] J. F. Faucon, M. D. Mitov, P. Méléard, I. Bivas, and P. Bothorel, “Bending Elasticity and Thermal Fluctuations of Lipid-Membranes—Theoretical and Experimental Requirements,” *J. de Physique*, vol. 50, no. 17, pp. 2389–2414, 1989.
- [99] J. Henriksen, A. C. Rowat, and J. H. Ipsen, “Vesicle fluctuation analysis of the effects of sterols on membrane bending rigidity,” *Eur. Biophys. J.*, vol. 33, no. 8, pp. 732–741, 2004.
- [100] L. Kramer, “Theory of Light Scattering from Fluctuations of Membranes and Monolayers,” *J. Chem. Phys.*, vol. 55, pp. 2097–2105, 1971.
- [101] U. Seifert and S. A. Langer, “Viscous Modes of Fluid Bilayer Membranes,” *Europhys. Lett.*, vol. 23, no. 1, pp. 71–76, 1993.
- [102] A. G. Zilman and R. Granek, “Undulations and Dynamic Structure Factor of Membranes,” *Phys. Rev. Lett.*, vol. 77, pp. 4788–4791, 1996.
- [103] V. A. Harmandaris and M. Deserno, “A novel method for measuring the bending rigidity of model lipid membranes by simulating tethers,” *J. Chem. Phys.*, vol. 125, no. 20, p. 204905, 2006.

- [104] J. C. Mathai, S. Tristram-Nagle, J. F. Nagle, and M. L. Zeidel, “Structural Determinants of Water Permeability through the Lipid Membrane,” *J. Gen. Physiol.*, vol. 131, no. 1, pp. 69–76, 2008.
- [105] M. Nakano, M. Fukuda, T. Kudo, N. Matsuzaki, T. Azuma, K. Sekine, H. Endo, and T. Handa, “Flip-Flop of Phospholipids in Vesicles: Kinetic Analysis with Time-Resolved Small-Angle Neutron Scattering,” *J. Phys. Chem. B*, vol. 113, no. 19, pp. 6745–6748, 2009.
- [106] W. K. den Otter and W. J. Briels, “The bending rigidity of an amphiphilic bilayer from equilibrium and nonequilibrium molecular dynamics,” *J. Chem. Phys.*, vol. 118, p. 4712, 2003.
- [107] H. Noguchi, “Anisotropic surface tension of buckled fluid membranes,” *Phys. Rev. E*, vol. 83, p. 061919, 2011.
- [108] M. Hu, P. Diggins, and M. Deserno, “Determining the bending modulus of a lipid membrane by simulating buckling,” *J. Chem. Phys.*, vol. 138, p. 214110, 2013.
- [109] M. Abramowitz and I. A. Stegun, *Handbook of Mathematical Functions*. New York: Dover, 1970.
- [110] A. J. Rzepiela, L. V. Schäfer, N. Goga, H. J. Risselada, A. H. De Vries, and S. J. Marrink, “Reconstruction of atomistic details from coarse-grained structures,” *J. Comput. Chem.*, vol. 31, no. 6, pp. 1333–1343, 2010.
- [111] X. Wang and D. M., “Determining the pivotal plane of fluid lipid membranes in simulations,” *J. Chem. Phys.*, vol. 143, p. 164109, 2015.
- [112] H.-J. Limbach, A. Arnold, B. A. Mann, and C. Holm, “ESPResSo – an extensible simulation package for research on soft matter systems,” *Comput. Phys. Commun.*, vol. 174, no. 9, pp. 704–727, 2006.
- [113] G. S. Grest and K. Kremer, “Molecular dynamics simulation for polymers in the presence of a heat bath,” *Phys. Rev. A*, vol. 33, no. 5, pp. 3628–3631, 1986.
- [114] B. Hess, C. Kutzner, D. van der Spoel, and E. Lindahl, “GROMACS 4: Algorithms for highly efficient, Load-Balanced, and scalable molecular simulation,” *J. Chem. Theory Comput.*, vol. 4, pp. 435–447, 2008.
- [115] H. J. C. Berendsen, J. P. M. Postma, W. F. van Gunsteren, A. DiNola, and J. R. Haak, “Molecular dynamics with coupling to an external bath,” *J. Chem. Phys.*, vol. 81, no. 8, pp. 3684–3690, 1984.

- [116] T. Soddemann, B. Dünweg, and K. Kremer, “Dissipative particle dynamics: A useful thermostat for equilibrium and nonequilibrium molecular dynamics simulations,” *Phys. Rev. E*, vol. 68, p. 046702, 2003.
- [117] S. A. Shkulipa, *Computer simulations of lipid bilayer dynamics*. PhD thesis, University of Twente, Enschede, The Netherlands, 2006.
- [118] C. de Boor, *A Practical Guide to Splines*. New York: Springer, 2001.
- [119] L. Fernandez-Puente, I. Bivas, M. D. Mitov, and P. Méléard, “Temperature and Chain Length Effects on Bending Elasticity of Phosphatidylcholine Bilayers,” *Europhys. Lett.*, vol. 28, no. 3, p. 181, 1994.
- [120] P. Méléard, C. Gerbeaud, T. Pott, L. Fernandez-Puente, I. Bivas, M. Mitov, J. Dufourcq, and P. Bothorel, “Bending elasticities of model membranes: influences of temperature and sterol content,” *Biophys. J.*, vol. 72, no. 6, pp. 2616–2629, 1997.
- [121] N. Chu, N. Kučerka, Y. Liu, S. Tristram-Nagle, and J. F. Nagle, “Anomalous swelling of lipid bilayer stacks is caused by softening of the bending modulus,” *Phys. Rev. E*, vol. 71, p. 041904, 2005.
- [122] J. Pan, S. Tristram-Nagle, N. Kučerka, and J. Nagle, “Temperature Dependence of Structure, Bending Rigidity, and Bilayer Interactions of Dioleoylphosphatidylcholine Bilayers,” *Biophys. J.*, vol. 94, no. 1, pp. 117–124, 2008.
- [123] J. A. Bouwstra, G. S. Gooris, M. A. Salomons-de Vries, J. A. van der Spek, and W. Bras, “Structure of human stratum corneum as a function of temperature and hydration: A wide-angle X-ray diffraction study,” *Int. J. Pharm.*, vol. 84, no. 3, pp. 205–216, 1992.
- [124] G. S. K. Pilgram, A. M. Engelsma-van Pelt, J. A. Bouwstra, and H. K. Koerten, “Electron Diffraction Provides New Information on Human Stratum Corneum Lipid Organization Studied in Relation to Depth and Temperature,” *J. Invest. Dermatol.*, vol. 113, pp. 403–409, 1999.
- [125] M. Caffrey and J. Hogan, “LIPIDAT: A database of lipid phase transition temperatures and enthalpy changes. DMPC data subset analysis,” *Chem. Phys. Lipids*, vol. 61, no. 1, pp. 1 – 109, 1992.
- [126] J. K. Mills and D. Needham, “Lysolipid incorporation in dipalmitoylphosphatidylcholine bilayer membranes enhances the ion permeability and drug release rates at the membrane phase transition,” *Biochim. Biophys. Acta*, vol. 1716, pp. 77–96, 2005.

- [127] D. Needham and M. W. Dewhurst, “The development and testing of a new temperature-sensitive drug delivery system for the treatment of solid tumors,” *Adv. Drug Deliv. Rev.*, vol. 53, pp. 285–305, 2001.
- [128] L. Pocivavsek, R. Dellsy, A. Kern, S. Johnson, B. Lin, K. Y. C. Lee, and E. Cerda, “Stress and fold localization in thin elastic membranes,” *Science*, vol. 320, no. 5878, pp. 912–916, 2008.
- [129] H. Diamant and T. A. Witten, “Compression induced folding of a sheet: An integrable system,” *Phys. Rev. Lett.*, vol. 107, no. 16, p. 164302, 2011.
- [130] H. Diamant and T. A. Witten, “Shape and symmetry of a fluid-supported elastic sheet,” *Phys. Rev. E*, vol. 88, no. 1, p. 012401, 2013.
- [131] O. Oshri, F. Brau, and H. Diamant, “Wrinkles and folds in a fluid-supported sheet of finite size,” *Phys. Rev. E*, vol. 91, no. 5, p. 052408, 2015.
- [132] C.-H. Lee, W.-C. Lin, and J. Wang, “All-optical measurements of the bending rigidity of lipid-vesicle membranes across structural phase transitions,” *Phys. Rev. E*, vol. 64, p. 020901, Jul 2001.
- [133] Z. A. Levine, R. M. Venable, M. C. Watson, M. G. Lerner, J. Shea, R. W. Pastor, and F. L. H. Brown, “Determination of biomembrane bending moduli in fully atomistic simulations,” *J. Am. Chem. Soc.*, vol. 136, no. 39, pp. 13582–13585, 2014.
- [134] J. M. Seddon, K. Harlos, and D. Marsh, “Metastability and Polymorphism in the Gel and Fluid Bilayer Phases of Dilauroylphosphatidylethanolamine,” *J. Biol. Chem.*, vol. 258, pp. 3850–3854, 1983.
- [135] P. Diggins IV, Z. A. McDargh, and M. Deserno, “Curvature Softening and Negative Compressibility of Gel-Phase Lipid Membranes,” *J. Am. Chem. Soc.*, vol. 137, pp. 12752–12755, 2015.
- [136] R. Dimova, “Recent developments in the field of bending rigidity measurements on membranes,” *Adv. Colloid Interface Sci.*, vol. 208, no. 0, pp. 225–234, 2014.
- [137] S. Steltenkamp, M. M. Müller, M. Deserno, C. Hennessal, C. Steinem, and A. Janshoff, “Mechanical properties of pore-spanning lipid bilayers probed by atomic force microscopy,” *Biophys. J.*, vol. 91, no. 1, pp. 217–226, 2006.
- [138] L. D. Landau and E. M. Lifshitz, *Theory of Elasticity*. Oxford: Butterworth-Heinemann, 1999.
- [139] B. West and F. Schmid, “Fluctuations and elastic properties of lipid membranes in the gel  $l_{\beta}$  state: a coarse-grained monte carlo study,” *Soft Matter*, vol. 6, pp. 1275–1280, 2010.

- [140] G. Pinamonti, S. Bottaro, C. Micheletti, and G. Bussi, “Elastic network models for RNA: a comparative assessment with molecular dynamics and SHAPE experiments,” *Nucl. Acids Res.*, vol. 43, pp. 7260–7269, 2015.
- [141] I. Bahar and R. L. Jernigan, “Vibrational Dynamics of Transfer RNAs: Comparison of the Free and Synthetase-bound Forms,” *J. Mol. Biol.*, vol. 281, pp. 871–884, 1998.
- [142] F. Tama, M. Valle, J. Frank, and C. L. Brooks III, “Dynamic reorganization of the functionally active ribosome explored by normal mode analysis and cryo-electron microscopy,” *Proc. Natl. Acad. Sci. USA*, vol. 100, pp. 9319–9323, 2003.
- [143] Y. Wang, A. J. Rader, I. Bahar, and R. L. Jernigan, “Global ribosome motions revealed with elastic network model,” *J. Struct. Biol.*, vol. 147, pp. 302–314, 2004.
- [144] A. W. Van Wynsberghe and Q. Cui, “Comparison of Mode Analyses at Different Resolutions Applied to Nucleic Acid Systems,” *Biophys. J.*, vol. 89, pp. 2939–2949, 2005.
- [145] Y. Wang and R. L. Jernigan, “Comparison of tRNA Motions in the Free Ribosomal Bound Structures,” *Biophys. J.*, vol. 89, pp. 3399–3409, 2005.
- [146] M. T. Zimmermann and R. L. Jernigan, “Elastic network models capture the motions apparent within ensembles of RNA structures,” *RNA*, vol. 20, pp. 792–804, 2014.
- [147] P. Setny and M. Zacharias, “Elastic Network Models of Nucleic Acids Flexibility,” *J. Chem. Theory Comput.*, vol. 9, pp. 5460–5470, 2013.
- [148] T. T. Foley, M. S. Shell, and W. G. Noid, “The impact of resolution upon entropy and information in coarse-grained models,” *J. Chem. Phys.*, p. 243104, 2015.
- [149] R. Potestio, *Coarse-grained modeling of protein structure and internal dynamics: comparative methods and applications*. PhD thesis, International School for Advanced Studies-SISSA, 2010.
- [150] M. Praprotnik, L. Delle Site, and K. Kremer, “Multiscale Simulation of Soft Matter: From Scale Bridging to Adaptive Resolution,” *Annu. Rev. Phys. Chem.*, vol. 59, pp. 545–571, 2008.
- [151] C. Globisch, V. Krishnamani, M. Deserno, and C. Peter, “Optimization of an Elastic Network Augmented Coarse Grained Model to Study CCMV Capsid Deformation,” *PLOS ONE*, vol. 8, p. e60582, 2013.

- [152] S. Kirkpatrick, C. D. Gelatt Jr, and M. P. Vecchi, “Optimization by Simulated Annealing,” *Science*, vol. 220, pp. 674–680, 1983.
- [153] V. Černý, “Thermodynamical approach to the traveling salesman problem: An efficient simulation algorithm,” *J. Optim. Theory Appl.*, vol. 45, pp. 41–51, 1985.
- [154] F. Wang and D. P. Landau, “Efficient, Multiple-Range Random Walk Algorithm to Calculate the Density of States,” *Phys. Rev. Lett.*, vol. 86, pp. 2050–2053, 2001.
- [155] A. Serganov, Y. R. Yuan, O. Pikovskaya, A. Polonskaia, L. Malinina, A. T. Phan, C. Hobartner, R. Micura, R. R. Breaker, and D. J. Patel, “Structural Basis for Discriminative Regulation of Gene Expression by Adenine- and Guanine-Sensing mRNAs,” *Chem. Biol.*, vol. 11, pp. 1729–1741, 2004.